

# **Anisotropic flow measurements at FAIR and SPS energies**

Dissertation

zur Erlangung des Doktorgrades  
der Naturwissenschaften

vorgelegt beim Fachbereich Physik  
der Johann Wolfgang Goethe - Universität  
in Frankfurt am Main

von

Viktor Klochkov  
aus Kherson, Ukraine

Frankfurt am Main 2019

(D 30)



vom Fachbereich Physik der  
Johann Wolfgang Goethe-Universität als Dissertation angenommen.

Dekan:	Prof. Dr. Michael Lang
Betreuer:	Dr. Ilya Selyuzhenkov
Gutachter:	Prof. Dr. Peter Senger
	Prof. Dr. Herbert Ströbele
	Prof. Dr. Christoph Blume
Datum der Disputation:	November 20, 2019



# Abstract

The Compressed Baryonic Matter experiment (CBM) at FAIR and the NA61/SHINE experiment at CERN SPS aim to study the area of the QCD phase diagram at high net baryon densities and moderate temperatures using heavy ion collisions. The FAIR and SPS accelerators cover energy ranges 2-11 and 13-150 GeV per nucleon respectively in laboratory frame for heavy ions up to Au and Pb. One of the key observables to study the properties of a matter created in such collisions is anisotropic transverse flow of particles.

In this work the performance of the CBM experiment for anisotropic flow measurements is studied with Monte-Carlo simulations using gold ions at SIS-100 energies employing different heavy-ion event generators. Also procedures for centrality estimation and charged hadron identification are described and corresponding frameworks are developed.

The measurement of the reaction plane angle is performed with Projectile Spectator Detector (PSD), which is a hadron calorimeter located at very forward angle. To prevent radiation damage by the high intensity ion beam, the PSD has a hole in the center to let the beam pass through. Various combinations of CBM detector subsystems are used to investigate the possible systematic biases in flow and centrality measurements. Effects of detector azimuthal non-uniformity and the PSD beam hole size on physics performance are studied. The resulting performance of CBM for flow measurements is demonstrated for identified charged hadron anisotropic flow as a function of rapidity and transverse momentum in

different centrality classes.

The measurement techniques developed for CBM were also validated with the experimental data recently collected by the NA61/SHINE experiment at CERN SPS for Pb+Pb collisions at the beam momenta  $30A$  GeV/ $c$ . Compared to the existing data from the NA49 experiment at the CERN SPS, the new data allows for more precise measurement of anisotropic flow harmonics. The fixed target setup of NA61/SHINE also allows to extend flow measurements available from the STAR at RHIC beam energy scan (BES) program to a wide rapidity range up to the forward region where projectile nucleon spectators appear. In this thesis an analysis of the anisotropic flow harmonics in Pb+Pb collisions at beam momenta  $30A$  GeV/ $c$  collected by the NA61/SHINE experiment in the year 2016 is presented. Flow coefficients are measured relative to the spectator plane estimated with the Projectile Spectators Detector (PSD). The flow coefficients are obtained as a function of rapidity and transverse momentum in different classes of collision centrality. The results are compared with the corresponding NA49 data and the measurements from the RHIC BES program.

# Kurzfassung

Das "Compressed Baryonic Matter" Experiment (CBM) bei FAIR und das NA61/SHINE Experiment bei CERN SPS zielen darauf ab, den Bereich des QCD-Phasendiagramms zu untersuchen bei hohen Nettobaryondichten und moderaten Temperaturen unter Verwendung von Schwerionenkollisionen.

Die FAIR- und SPS-Beschleuniger decken den Energiebereich von wenigen bis 150 GeV pro Nukleon im Laborrahmen für Schwerionen bis hin zu Au bzw. Pb ab.

Der anisotrope Teilchenfluss gehört zu den wichtigsten Beobachtungsgrößen, die Aufschluss über die Eigenschaften der in Schwerionen hohen energie Materie geben. In Rahmen dieser Arbeit werden Monte-Carlo Simulationene durchgeführt und analysiert, um zukünftige Messungen den anisotropen Teilchenflusse mit dem CBM Detectorsystem zu optimieren. Es wurden verschiedene Ereignisgeneratoren verwendet, um die SIS-100 Strahlionen zu bescheiben. Auch Verfahren zur Zentralitätsabschätzung und zur Identifizierung von geladenen Hadronen werden beschrieben, fü die entsprechende Komputerverprogramme wurde entwickelt.

Verschiedene Kombinationen von CBM-Detektor-Subsystemen werden verwendet, um die möglichen systematischen Fehlers in der Fluss- und Zentralitätsmessungen. Es werden die Auswirkungen der azimuthalen Inhomogenität des Detektors und der Strahllochgröße auf die Qualität des Messungen untersucht. Die resultierende Performanz der CBM-Detektorsystems für Flussmessungen wird für identifizierte geladene anisotrope Hadronenströmungen als Funk-

tion von Rapidität und Transversalimpulse in verschiedenen Zentralitätsklassen demonstriert.

Die für CBM entwickelten Analysetechniken wurden auch auf die experimentellen Daten angewendet, die kürzlich mit dem NA61/SHINE-Experiment am CERN SPS in Blei-Blei-Kollisionen am Strahlimpuls  $30A \text{ GeV}/c$  gemessen wurden. Im Vergleich zu den bestehenden Daten des NA49-Experiments am CERN SPS ermöglichen die neuen Daten eine genauere Messung von Höheren Ordnungen des anisotropen Fluss. Der "fixed target" Aufbau des NA61/SHINE Experiment ermöglicht es auch, durchgeführten Messungen des Flusses. die Flussmessungen, die vom STAR-Experiment am RHIC zur Verfügung stehen, auf einen weiten Rapiditätbereich bis in den vorderen Bereich auszudehnen, in dem Projektil-Fragmente auftreten. In dieser Arbeit wird eine Analyse des anisotropen Flusses in Blei-Blei-Kollisionen bei Strahlimpuls von  $30A \text{ GeV}/c$  vorgestellt, der vom NA61/SHINE-Experiment im Jahr 2016 gemessen wurde. Die Flusskoeffizienten werden mithilfe der PSD gemessen Spektatoren bestimmt. Die Flusskoeffizienten werden als Funktion von Rapidität und Transversalimpuls in verschiedenen Klassen der Kollisionszentralität analysiert. Die Ergebnisse werden mit den entsprechenden NA49-Daten und den Messungen aus dem RHIC BES-Programm verglichen.



# Contents

<b>1</b>	<b>Introduction</b>	<b>5</b>
1.1	Fundamental forces . . . . .	5
1.2	Standard model . . . . .	6
1.3	Quantum-chromo dynamics . . . . .	7
1.4	Exploration of the QCD phase diagram . . . . .	8
1.4.1	Neutron stars . . . . .	10
1.4.2	Neutron star mergers and gravitational waves . . . . .	12
1.4.3	Relativistic heavy-ion collisions . . . . .	13
<b>2</b>	<b>Anisotropic flow</b>	<b>17</b>
2.1	Geometry of heavy-ion collision . . . . .	18
2.2	Existing data . . . . .	20
2.3	Flow measurement methods . . . . .	22
2.3.1	The flow-vector . . . . .	23
2.3.2	Event plane method . . . . .	24
2.3.3	Scalar product method . . . . .	25
2.3.4	Cumulant method . . . . .	26
2.4	Corrections for detector azimuthal anisotropies . . . . .	26
2.4.1	Recentering . . . . .	27
2.4.2	Twist . . . . .	28
2.4.3	Rescaling . . . . .	28

2.4.4	Q-vector correction framework . . . . .	28
<b>3</b>	<b>Fixed target experiments at FAIR and CERN SPS</b>	<b>31</b>
3.1	Facility for Antiproton and Ion Research . . . . .	31
3.1.1	The Compressed Baryonic Matter experiment . . . . .	32
3.2	Super Proton Synchrotron @ CERN . . . . .	43
3.2.1	NA61/SHINE experiment . . . . .	43
<b>4</b>	<b>Calibration tools and analysis frameworks</b>	<b>47</b>
4.1	CBM simulation setup . . . . .	48
4.1.1	Event generators . . . . .	48
4.1.2	Datasets . . . . .	48
4.1.3	Event selection . . . . .	49
4.1.4	Track selection . . . . .	50
4.2	NA61/SHINE data . . . . .	52
4.2.1	Event selection . . . . .	52
4.2.2	Tracks selection . . . . .	55
4.3	NA61/SHINE TPC calibration . . . . .	59
4.3.1	Global $T_0$ calibration (Stage 1) . . . . .	59
4.3.2	Drift velocity calibration (Stage 2) . . . . .	61
4.3.3	Chamber $T_0$ calibration (Stage 3) . . . . .	62
4.3.4	Chamber positions calibration (Stage 4) . . . . .	64
4.3.5	Summary . . . . .	64
4.4	Charged hadron identification . . . . .	66
4.4.1	Identification with Time-of-Flight and specific energy loss . . . . .	66
4.4.2	Framework description . . . . .	67
4.4.3	Results . . . . .	72
4.4.4	Summary . . . . .	77
4.5	Centrality . . . . .	78

---

4.5.1	Mapping collision geometry to experimental observables . . .	78
4.5.2	Glauber model . . . . .	80
4.5.3	MC-Glauber fit . . . . .	80
4.5.4	Framework description . . . . .	81
4.5.5	Results . . . . .	84
4.5.6	Summary . . . . .	90
<b>5</b>	<b>Results</b>	<b>93</b>
5.1	NA61/SHINE measurement . . . . .	93
5.1.1	Correction for detector effects . . . . .	93
5.1.2	Systematics . . . . .	94
5.1.3	Results for directed flow . . . . .	96
5.1.4	Results for elliptic flow . . . . .	101
5.2	CBM performance . . . . .	105
5.2.1	Correction for detector effects . . . . .	105
5.2.2	Results for directed flow . . . . .	108
<b>6</b>	<b>Conclusions and outlook</b>	<b>113</b>
	<b>Bibliography</b>	<b>127</b>
	<b>Zusammenfassung</b>	<b>137</b>
	<b>Acknowledgments</b>	<b>143</b>
	<b>Curriculum Vitae</b>	<b>145</b>



# Chapter 1

## Introduction

### 1.1 Fundamental forces

All existing types of interaction can be deduced from four fundamental forces: gravitation, electromagnetic, weak and strong force. Gravitation is the weakest force at microscopic scale, but becoming dominating at astronomical scales. Every object with a non-zero mass is a subject to the gravitational interaction. It is responsible for the formation of the stars and planets, galaxies and black holes. The electromagnetic interaction appears between any two electrically charged particles. Like gravitation it is long-range, but much stronger. Electromagnetic force keeps electrons inside the atoms and defines the properties of any chemical element. It is hard to imagine our every-day live without human-made electrical devices. The weak interaction is a short-range correlation which is responsible for the  $\beta$ -decay. The strong force is the strongest force in this list. It keeps nucleons inside the atomic nucleus and quarks and gluons inside the nucleons. The summary of all fundamental forces is presented in the table 1.1. The most complicated and less understood interaction is the strong interaction.

Table 1.1: Fundamental forces.

Interaction	Gravitation	Weak	Electromagnetic	Strong
Carrier	not observed yet	$W^\pm, Z^0$	$\gamma$	$g$
Strength	$10^{-2}$	$10^{-34}$	$10^{-6}$	10
Range (m)	$\infty$	$10^{-18}$	$\infty$	$10^{-15}$

## 1.2 Standard model

The Standard model of particle physics is a theory classifying all known elementary particles and describing three out of four (except of gravitation) fundamental forces. All elementary particles can be divided into two large groups (figure 1.1):

- bosons (integer spin)
- fermions (half-integer spin)

In the boson sector there are four gauge bosons (force carriers) with spin  $S = 1$  and the Higgs boson with spin  $S = 0$ . In the fermion sector there are six quarks (up, down, charm, strange, top, bottom) and six leptons (electron, electron neutrino, muon, muon neutrino, tau, tau neutrino). They are paired to form three generations, which have similar properties. Almost all matter which we see consist of up and down quarks which form protons and neutrons, and electrons. With the discovery of the Higgs boson, which explains the mechanism how elementary particles acquire mass, the Standard model is complete and self-consistent. Although there are several phenomena unexplained, such as:

- baryon matter asymmetry
- neutrino oscillations and non-zero mass
- dark matter and dark energy

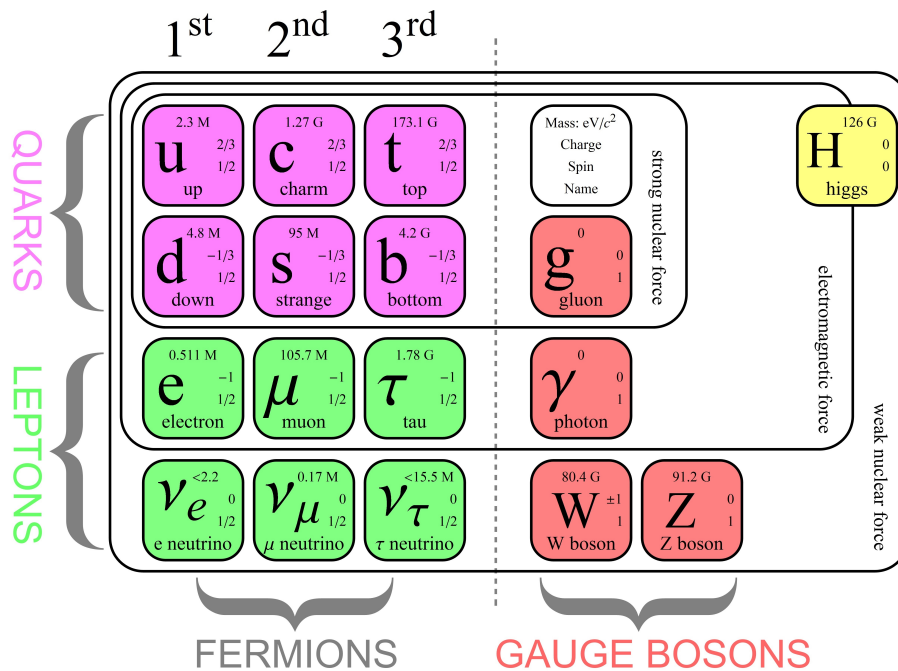


Figure 1.1: The Standard Model of elementary particles [1]

- gravity

There are many theoretical attempts to solve those problems introducing new particles, symmetries or dimensions. (Un)fortunately non of them were confirmed experimentally.

### 1.3 Quantum-chromo dynamics

Quantum-chromo dynamics (QCD) is a theory of strong interaction between quarks and gluons. It is a quantum field theory based on Special Unitary group in 3 dimensions (SU(3) symmetry). The two main features of the QCD theory are:

- quark confinement (there no free quarks)
- asymptotic freedom (interaction between quarks is weak at short distances or large energies)

The QCD Lagrangian is:

$$\mathcal{L}_{\text{QCD}} = \bar{\psi}_i (i(\gamma^\mu D_\mu)_{ij} - m \delta_{ij}) \psi_j - \frac{1}{4} G_{\mu\nu}^a G_a^{\mu\nu} \quad (1.1)$$

where  $\psi_i$  is a quark field wavefunction with a flavor  $i$ ,  $D_\mu := \partial_\mu - ig A_\mu^\alpha \lambda_\alpha/2$  is the gauge covariant derivative,  $\gamma^\mu$  are Dirac matrices,  $G_{\mu\nu}$  is gauge invariant gluon field strength tensor:

$$G_{\mu\nu}^a = \partial_\mu \mathcal{A}_\nu^a - \partial_\nu \mathcal{A}_\mu^a + gf^{abc} \mathcal{A}_\mu^b \mathcal{A}_\nu^c \quad (1.2)$$

where  $\mathcal{A}_\nu^a$  are the gluon fields.

The theory is quite complicated and cannot be solved analytically. There several theoretical approaches to this problem including lattice QCD, perturbative QCD and effective field theories. This work is dedicated to experimental approach to study QCD.

## 1.4 Exploration of the QCD phase diagram

A schematic representation of the QCD phase diagram is shown in the figure 1.2. At low baryon chemical potential  $\mu_B$  and low temperature  $T$  matter exists in the form of hadrons (mostly protons and neutrons). At a temperature around 150 MeV and zero chemical potential a smooth cross-over transition to quark and gluon degrees of freedom occurs as we know from lattice QCD calculations. This transition is illustrated in the figure 1.3. Unfortunately it is very challenging to extend those calculations to non-zero  $\mu_B$  due to so-called "sign"-problem. At large baryon chemical potential and moderate temperatures QCD inspired models expect structures in the phase diagram, like first order phase transition and critical endpoint, and exotic phases of QCD matter [3, 2].

There are different ways to study the QCD phase diagram in the region of



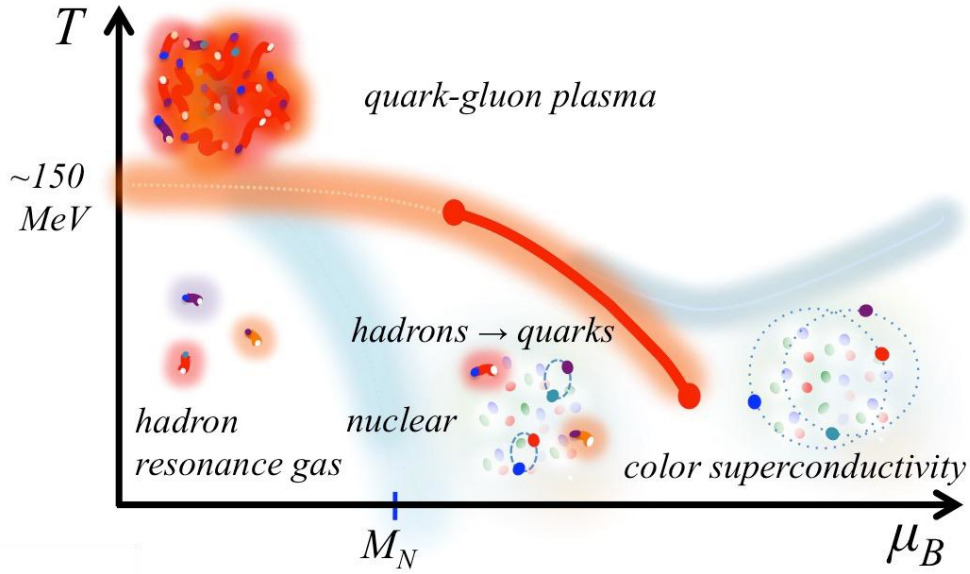


Figure 1.2: Schematic phase diagram of dense nuclear matter, in the baryon chemical potential  $\mu_B$  - temperature  $T$  plane [2].

high net-baryon densities, mainly:

- Neutron stars observation
- Neutron stars mergers and gravitational waves
- Relativistic heavy-ion collisions

Combinations of all three methods will allow us to study wide area of the diagram including high temperatures and get a common picture. The properties of the dense baryonic matter at different conditions are summarized in the table 1.2. Nuclear matter can be characterized by its equation of state (EoS), which is related to pressure ( $p$ ), temperature ( $T$ ), volume ( $V$ ), energy ( $E$ ), density ( $\rho$ ) and isospin ( $p$ ):

$$p = \left. \frac{\delta E}{\delta V} \right|_{T=const} \quad (1.3)$$

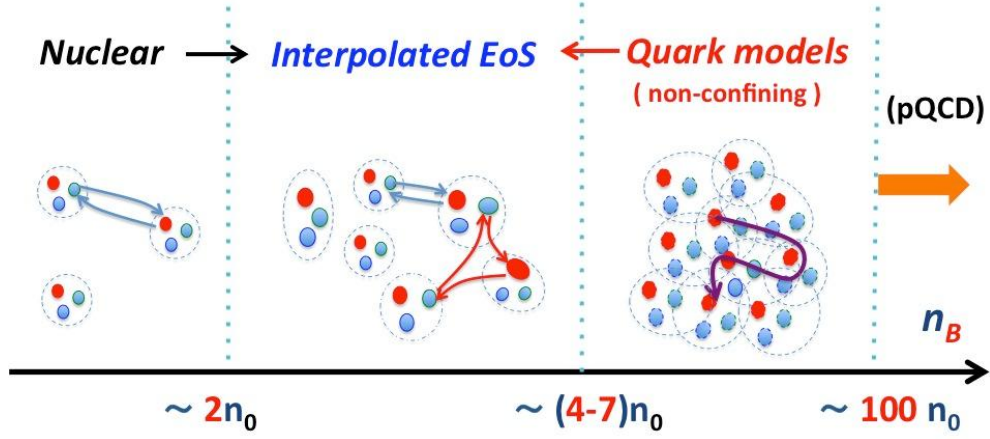


Figure 1.3: A schematic picture of the the transition from nuclear to deconfined quark matter with increasing density [2].

Table 1.2: Dense baryonic matter properties at different conditions.

	Neutron stars	Gravitational waves	Heavy-ion collisions
Temperature (MeV)	<10	10-100	100-150
Density ( $\rho_0$ )	<10	2-6	5-15
Time	$\infty$	10 ms	$10^{-23}$ s
Size	10 km	10 km	10 fm

with  $V = A/\rho$  and  $\delta V/\delta\rho = -A^2\rho$ :

$$p = \rho^2 \frac{\delta(E/A)}{\delta\rho} \Big|_{T=const} \quad (1.4)$$

Illustration of different theoretical predictions of EoS are shown in the figure 1.4.

### 1.4.1 Neutron stars

Given the EoS, mass and radius of a neutron star can be calculated by the the Tolman-Oppenheimer-Volkoff (TOV) equation [5], which is a solution of Ein-

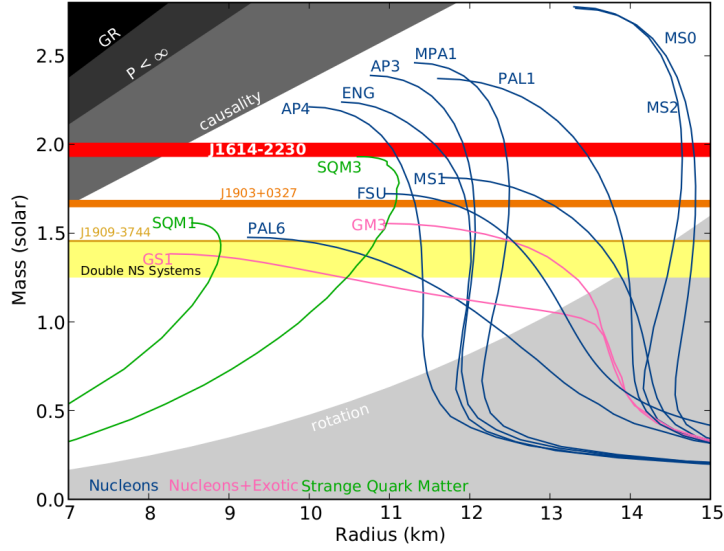


Figure 1.4: The neutron star mass-radius relation as predicted by different Equations of State [4].

stein's equation [6] in spherical coordinates:

$$\frac{dP}{dr} = -\frac{Gm}{r^2} \rho \left(1 + \frac{P}{\rho c^2}\right) \left(1 + \frac{4\pi r^3 P}{mc^2}\right) \left(1 - \frac{2Gm}{rc^2}\right)^{-1} \quad (1.5)$$

There are a lot of theoretical hypotheses about neutron star composition and corresponding equations of state [7, 8], as illustrated in the figure 1.5. The most interesting part is the inner core, where extreme densities of 3-9  $\rho_0$  are reached.

According to TOV equation, the measurement of mass and radius of a neutron star would determine the EoS. Already the mass information allows to discriminate different EoS. With observation of a neutron star with a mass of 2 Solar masses by Shapiro delay [4] many EoS were ruled out. Several model prediction are shown in the figure 1.4 together with the experimental constrains.

The Neutron Star Interior Composition Explorer (NICER) at the International Space Station (ISS) will provide simultaneous measurements of mass and radius of neutron star in the near future [10]. The measurement principle is based on gravitation lensing which is stronger with increasing mass to radius relation.

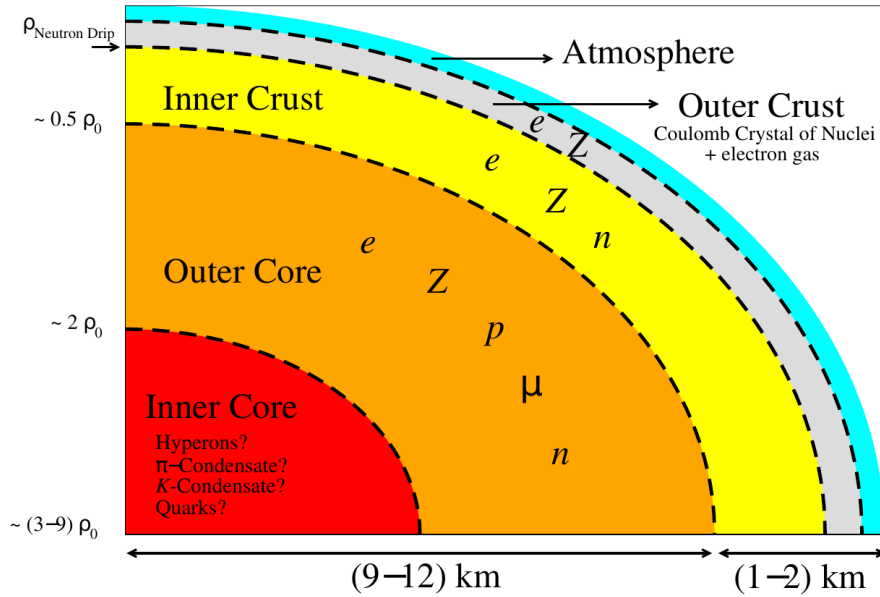


Figure 1.5: Possible structure of the neutron star [9].

By detecting radiation from two sides of neutron star at the same time radius estimation can be obtained.

### 1.4.2 Neutron star mergers and gravitational waves

After the first observation of gravitation waves by LIGO and Virgo Collaborations [11] we have one more way to study the QCD phase diagram. During a collision of two neutron stars a hot (10-100 MeV) and dense ( $2-6 \rho_0$ ) medium is created. A simulation of the density and temperature in a neutron star merger is shown in the figure 1.6.

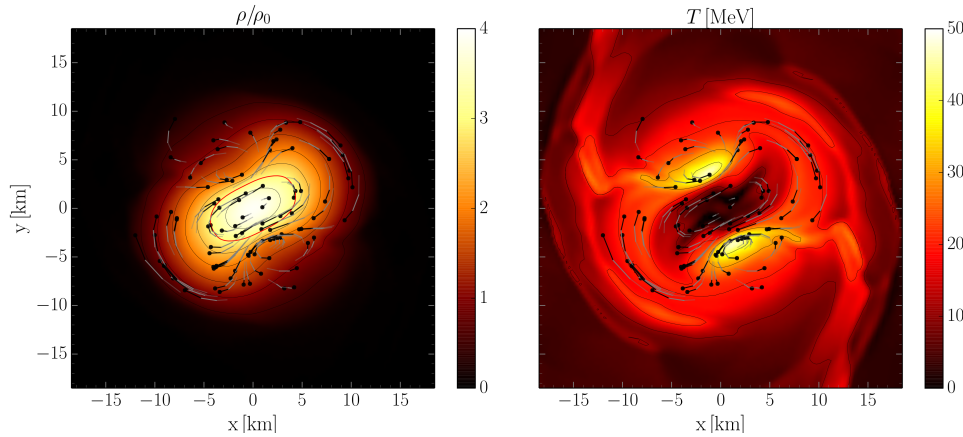


Figure 1.6: Distributions of the rest-mass density  $\rho$  in units of  $\rho_0$  (left panel) and the temperature (right panel) on the equatorial plane at a post-merger time of  $t=6.34$  ms for the LS220-M132 binary [12].

The observation of the system evolution (prompt or delayed collapse to black hole or no collapse) with gravitation waves together with electromagnetic signals [13, 14] allows to constrain the equation of state.

### 1.4.3 Relativistic heavy-ion collisions

Another method to explore the QCD phase diagram is especially relevant to this thesis and the only one which can be performed in the laboratory is the analysis of relativistic heavy-ion collisions. Different stages of a heavy-ion collision at ultra-relativistic energies are shown in the figure 1.7.

During a collision of two heavy nuclei at high energies, a hot and dense medium is created in the overlap region. The lifetime and size of it is very small, but unlike to previous methods number of collision one can study limited only by accelerator and detector capabilities.

Experimentally we have an access only to the final stage of the collision. There are many detector techniques which allow to reconstruct the final stage and analysis techniques (together with model calculations) to make assumptions about

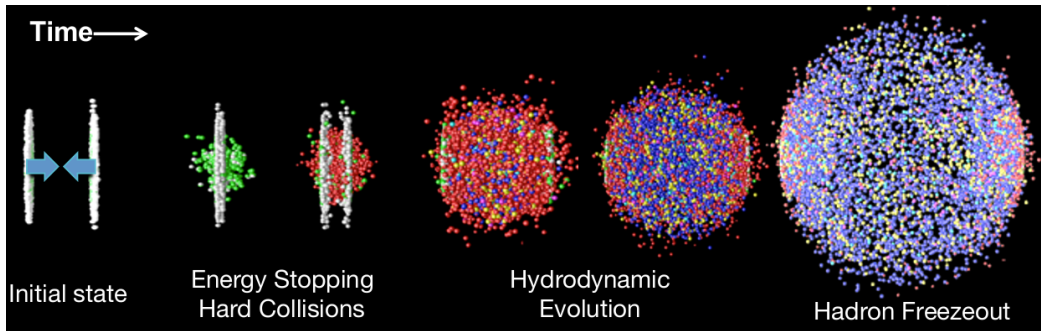


Figure 1.7: Stages of a heavy-ion collision [15].

the initial stage.

The investigation of properties of strongly interacting matter with heavy-ion collisions started around 40 years ago. During this time the experimental technologies vastly evolved. With different types of accelerators and detectors we were able to increase energies and interaction rates by many orders of magnitude, but the initial idea of colliding two nucleus and measuring produced particles still allows us to learn something new.

There two different approaches in colliding heavy ions (in general, any particles): colliding two beams, and one beam (projectile) with a fixed target. Respectively, all heavy ion experiments can be divided into colliders and fixed target. There are advantages and disadvantages of each type of experiment geometry. Advantages of the fixed target geometry comparing to colliders:

- higher luminosity can be achieved
- full acceptance in forward hemisphere including projectile spectators (no beam pipe)
- coverage for low  $p_T$  due to relativistic boost

Advantages of the collider geometry comparing to fixed target:

- higher energy can be achieved

- uniform backward-forward acceptance
- acceptance doesn't change depending on energy

### Brief historical overview

The investigation of the properties of strongly interacting matter at high temperatures was proposed by Rolf Hagedorn more than 50 years ago. To achieve such condition of hot and dense matter the high energy heavy-ion collisions could be used. It was suggested that with increasing the energy, new degrees of freedom may become available. At that time no quarks and gluons were discovered yet, and the QCD theory was not developed.

Exploration of the QCD phase diagram with heavy-ion collisions started around 40 years ago with AGS experiments [16] at Brookhaven National Laboratory (BNL) [17], at Nuclotron in JINR [18], Dubna and at CERN. Also contributed a lot experiments FOPI [19, 20] and KaoS [21].

After years of experimental and theoretical efforts one of the biggest discovery in this field was made in the year 2000 – the quark-gluon plasma. The exiting properties of this state of matter are still being revealed. For example, it was shown at RHIC collider at BNL that quark-gluon matter has properties of an ideal liquid [22].

At the moment there are several experiments exploring QCD phase diagram in a different energy ranges:

- HADES [23] at SIS18
- Baryonic Matter at Nuclotron (BM@N) [24, 25], Dubna, Russia
- NA61/SHINE [26, 27] at Super Proton Synchrotron (SPS)
- STAR [28] at Relativistic Heavy Ion Collider (RHIC), Brookhaven, US

- A Large Ion Collider Experiment (ALICE) [29, 30] at Large Hadron Collider (LHC) [31]

Recently, STAR Collaboration extended Beam Energy Scan (BES) Programme to energies below  $\sqrt{s_{NN}}=7.7$  GeV with fixed target regime of detector operation – STAR Fixed Target (FXT) Programme [32]. There are several heavy-ion experiments preparing to start operation in the near future.

- Multi-Purpose Detector (MPD) at Nuclotron-based Ion Collider Facility (NICA) [33, 34] in Dubna, Russia.
- Compressed Barionic Matter (CBM) at Facility for Antiproton and Ion Research (FAIR) in Darmstadt.
- Heavy-ion program at J-PARC [35] in Japan (in a planning stage stage).

MPD will operate at energies  $\sqrt{s_{NN}}=4-11$  GeV in the collider mode. More details about the Compressed Baryonic Matter experiment are in the section Sec. 3.1.

One of the most important observables, which is sensitive both to the EoS and the degrees of freedom in the early fireball, is the anisotropic collective flow of particles, which will be discussed in the following chapter.

There are many observables constructed to put constrains on the theories, in the next section described one of them – the anisotropic flow.



# Chapter 2

## Anisotropic flow

The first attempts to study properties of nuclear matter using heavy-ion collisions (A+A) started in the 1970s. It was suggested that there is a difference between A+A and multiple nucleon-nucleon collisions due to large collective pressure, shock waves and collective flow. After several years of developing measuring techniques and improving detector technologies, the collective flow of protons was observed in 1980s at the BEVALAC and SIS-18 at GSI [36, 37]. The next big step was done at Brookhaven Alternate Gradient Synchrotron (AGS) and later at the CERN Super Proton Synchrotron (SPS) by observing the in-plane elliptic flow, which appears above beam kinetic energy of 4A GeV . It was first suggested by Ollitrault [38] in 1992. Later at the Brookhaven Relativistic Heavy Ion Collider (RHIC) large elliptic flow and its scaling with number of constituent quarks was observed [39]. That is considered as an indication of the strongly interacting Quark Gluon Plasma (sQGP). The experiments at CERN Large Hadron Collider (LHC) confirmed the large elliptic flow [40], but not the scaling at high transverse momentum. During last years an elliptic flow pattern was observed in p+Pb and even high multiplicity p+p collisions at LHC.

## 2.1 Geometry of heavy-ion collision

In heavy-ion collisions, the initial geometry and relative position of the nuclei play an important role. A picture of two colliding nuclei is shown on the figure 2.1, left. The vector, which is connecting centers of the nuclei is called impact parameter

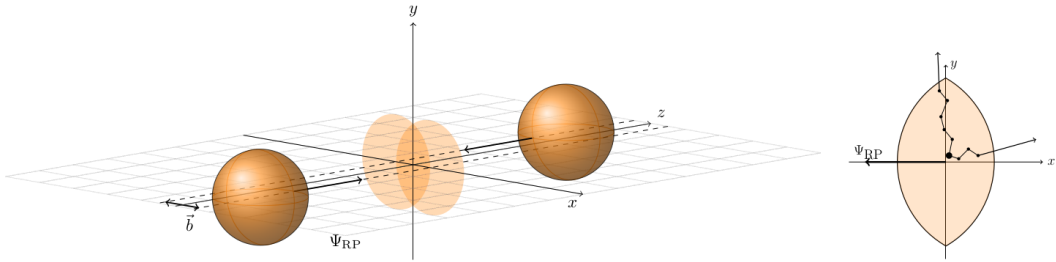


Figure 2.1: Left: the two nuclei approach each other along the direction of the  $z$ -axis with impact parameter  $b$ . The plane spanned by  $b$  and  $e_z$  is the reaction plane. Right: the spatial asymmetry develops through multiple scattering into a momentum asymmetry. Taken from [41].

$b$ . The reaction plane ( $RP$ ) is spanned by the vector of the impact parameter and the beam direction. The azimuth of the reaction plane is called the reaction plane angle ( $\Psi_{RP}$ ), and it is a symmetry plane of the collision. For non-central collisions, the asymmetry of the initial energy density in the transverse plane is expected to be aligned with the direction of the reaction plane.

There are different ways to estimate this angle with measurable quantities. To estimate the reaction plane orientation it is common to use the azimuthal asymmetry of particle production in the plane transverse to the beam direction. Due to the momentum transfer between participants and spectators, the spectators (fragments of projectile and target nuclei) are deflected in the course of the collision. The spectator deflection direction is likely to be correlated with the impact parameter (or reaction plane) direction. As an approximation for the reaction plane angle one can use following symmetry planes:

- participants plane (defined by the symmetry plane of participating nucleons)
- projectile spectators plane
- target spectators plane

They are illustrated in the figure 2.2.

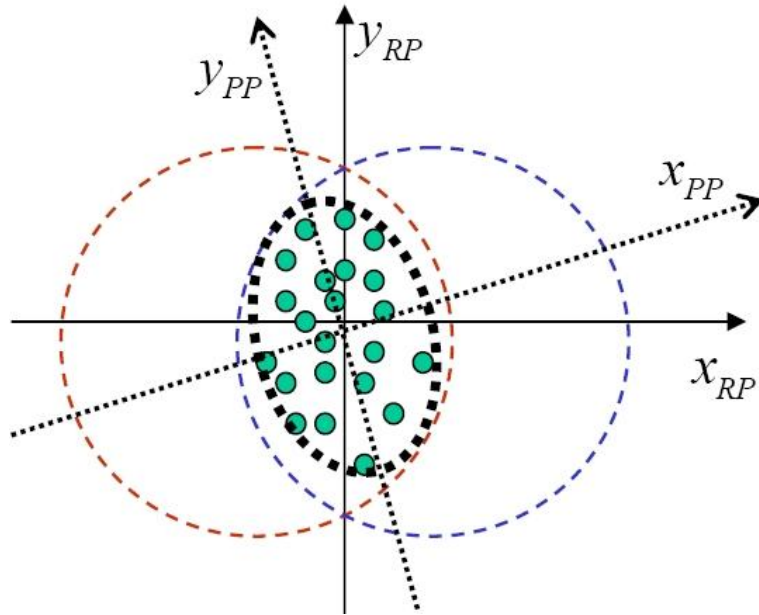


Figure 2.2: The illustration of the definitions of the reaction plane and participant plane ( $PP$ ) coordinate systems [42]. The distribution of the produced particles does not coincide with the reaction plane due to the fluctuations.

In this work, projectile spectators will be used to define the reaction plane. This method provides an estimate of the reaction plane independent of the produced particles. The rapidity gap between spectators and produced particles allows to suppress non-flow contributions (will be discussed later) and momentum conservation effects [43].

During the evolution of the created medium, spatial anisotropy of the energy density converts to momentum anisotropy of the produced particles due to interaction between them [44]. In an asymmetrical medium, the pressure gradient

will be also asymmetrical. Figure 2.1 (right) illustrates, that a particle will experience a larger pressure in the direction of the reaction plane. The anisotropy of the produced particles in the final stage can be measured experimentally. Based on the symmetries of the overlap region one can quantify this asymmetry using Fourier decomposition:

$$\frac{d^3N}{d^3p} = \frac{1}{2\pi} \frac{d^2N}{p_T dp_T dy} \left( 1 + 2 \sum_{n=1}^{\infty} v_n \cos(n(\varphi - \Psi_{m,SP})) \right) \quad (2.1)$$

where  $n$  is harmonic number,  $\Psi_{m,SP}$  is a symmetry plane angle for a harmonic  $m$  (in general case,  $m \neq n$  and flow coefficients can be defined relative to any symmetry plane),  $v_n$  are called flow harmonics and can be calculated as follows:

$$v_n\{\Psi_m\} = \langle \cos(n(\varphi_i - \Psi_{m,SP})) \rangle \quad (2.2)$$

where the angle brackets mean an average over all particles in all events. The sine term vanishes due to symmetry with respect to the reaction plane.

The flow harmonics correspond to the asymmetry for a given harmonics in the Fourier expansion of the distribution.  $v_1$  corresponds to the deflection of the particles transverse to the beam (directed flow),  $v_2$  and higher  $v_n$  correspond to the distribution ellipticity (elliptic flow), triangularity (triangular flow), etc. Magnitude of  $v_n$  depends of the system size, energy, centrality and other event and particle properties. The main feature of anisotropic flow is its sensitivity to early stages of collision. It is originated from particles spatial anisotropy in initial stage, which vanishes already in first few  $fm/c$  of the collision.

## 2.2 Existing data

During past 40 years flow measurements from low energies at SIS-18 and AGS to very high energies at LHC were performed. In this section selected results

relevant to this work are discussed.

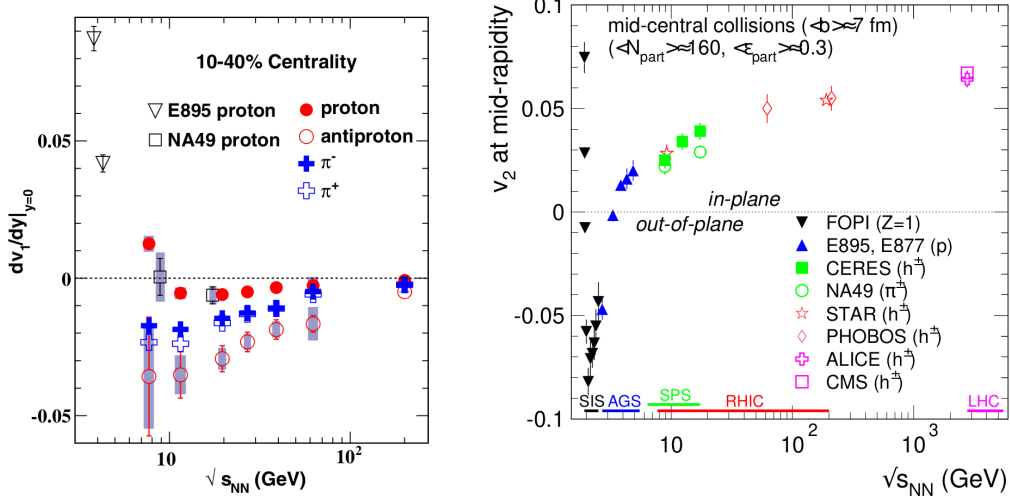


Figure 2.3: Directed flow slope for protons and pions at midrapidity vs. Au+Au collision energy (left). Statistical (bars) and systematical (shaded area) uncertainties are shown separately. Elliptic flow slope at midrapidity vs. collision energy [45] (right).

Directed flow slope for protons and pions at midrapidity figure 2.3 (left) Directed flow slope for protons and lambda changes sign.

Example of existing elliptic flow measurement in a wide energy range is shown in the figure 2.3 (right). Elliptic flow changes sign two times.

Measurements [46] by the NA49 experiment, which is predecessor of the NA61/SHINE, of the directed flow are presented in the figure 2.4. Proton and pion directed and elliptic flow were measured at the energies of 40 and 158 A GeV.

First preliminary STAR Fixed target results on anisotropic flow measurements in Au+Au collisions at 4.5 A GeV [47] are presented in the figure 2.5. The STAR fixed target energy range is close to CBM energies and the lowest SPS energy. At lower energies high precision differential measurements are performed by the HADES Collaboration [48, 49].

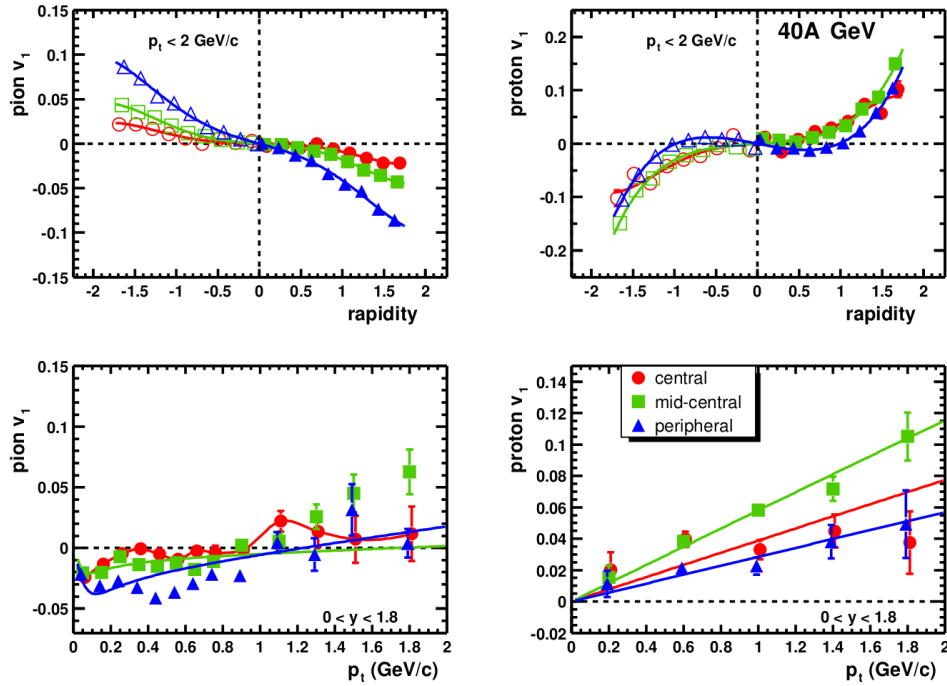


Figure 2.4: Directed flow  $v_1$  for pions (left) and protons (right) vs. rapidity (top) and transverse momentum (bottom) for Pb+Pb collision @ 40A GeV beam energy. Three different centralities are shown in different colors.

## 2.3 Flow measurement methods

To calculate flow coefficients one needs to use Eq. 2.2. It contains experimentally unmeasurable quantify  $\Psi_{n,SP}$ . There are several ways to rewrite this equation to have only experimentally measurable quantities on the right-hand side. The methods are following:

- event plane method
- scalar product method
- cumulant method

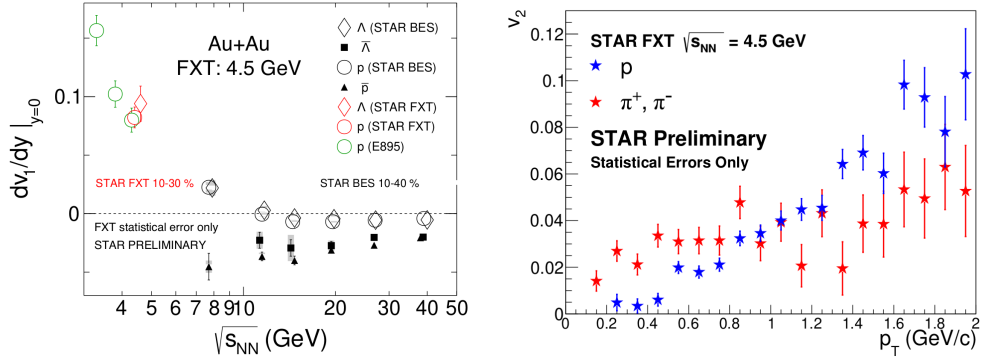


Figure 2.5: Mid-rapidity directed flow slope versus beam energy for for baryons (left). Elliptic flow  $v_2$  for pions and protons (right) [47].

### 2.3.1 The flow-vector

The azimuthal asymmetry of the measured distributions can be described in the terms of two dimensional flow vector  $\mathbf{q}_n$  which is defined by a sum of unit vectors  $\mathbf{u}_{n,i}$ :

$$\mathbf{u}_{n,i} = \{\cos n\varphi_i, \sin n\varphi_i\} \quad (2.3)$$

$$\mathbf{Q}_n = \frac{1}{M} \sum_i^M \mathbf{u}_{n,i} \quad (2.4)$$

where  $\varphi$  is azimuthal angle of a particle,  $M$  is number of particles.  $\mathbf{Q}_n$ -vectors are determined event-by-event, while  $\mathbf{u}_{n,i}$ -vector for a single particle with index  $i$ . One could also use a different normalization of the flow vector, for example, normalize to its absolute value:

$$\mathbf{Q}_n = \frac{1}{Q} \sum_i^M \mathbf{u}_{n,i} \quad (2.5)$$

Experimentally we don't measure individual particles, but tracks or signals in calorimeters or any other type of channelized detector. In this case the definition of the flow vector should be adjusted. For example, in case of a calorimeter one

can rewrite the  $Q_n$  vector definition:

$$\mathbf{Q}_n^{ch} = \frac{1}{E_s} \sum_j^{N_s} E_j \mathbf{n}_j \quad (2.6)$$

The unit vector  $\mathbf{n}_j$  points to the center of the  $j$ -th module,  $E_j$  is the energy deposition in the  $j$ -th module,  $N_s$  is the number of modules and  $E_s = \sum_j^{N_s} E_j$  is the total energy. The  $Q_n$ -vector gives the average direction of particles for a given harmonic.

### 2.3.2 Event plane method

Using equation Eq. 2.4 one can estimate the reaction plane angle with the so-called event plane angle:

$$\Psi_{EP}^n = \frac{1}{n} \text{atan2}(Q_y^n, Q_x^n) \quad (2.7)$$

In case of infinitely large  $M$ , the event plane angle coincides with the reaction plane angle. Otherwise, one needs to use the resolution correction factor  $R$ , which shows how good both angles are correlated. With a known reaction plane angle, resolution can be calculated as:

$$\mathbf{R}_n = \langle \cos n(\Psi_{RP}^n - \Psi_{EP}^n) \rangle \quad (2.8)$$

There are different ways to estimate the  $\mathbf{Q}$ -vector resolution correction factors  $R_{1,\alpha}^A \{B, C\}$ . For example, the 3-subevent method:

$$R_{1,\alpha}^A \{B, C\} = \sqrt{2 \frac{\langle Q_{1,\alpha}^A Q_{1,\alpha}^B \rangle \langle Q_{1,\alpha}^A Q_{1,\alpha}^C \rangle}{\langle Q_{1,\alpha}^B Q_{1,\alpha}^C \rangle}} \quad (2.9)$$



or mixed harmonic method:

$$R_{1,\alpha}^A \{B, C, D\} = \sqrt{2 \frac{\langle Q_{1,\alpha}^A Q_{1,\beta}^B \rangle \langle Q_{1,\alpha}^A Q_{1,\gamma}^C Q_{2,\delta}^D \rangle}{\langle Q_{1,\beta}^B Q_{1,\gamma}^C Q_{2,\delta}^D \rangle}} \quad (2.10)$$

where  $A, B, C, D$  are different subevents (measured in different kinematic regions or for different particle species) and  $(\alpha, \beta, \gamma, \delta) = \{(x, x, x, x), (x, x, y, y), (y, y, y, x), (y, y, x, y)\}$ .

Independent estimates of the flow harmonics  $v_n$  can be obtained using the following method:

$$v_1^\alpha \{A\} = \frac{2 \langle u_{1,\alpha} Q_{1,\alpha}^A \rangle}{R_{1,\alpha}^A} \quad (2.11)$$

$$v_2^{\alpha\beta\gamma} \{A, B\} = \kappa_{\alpha\beta\gamma} \frac{4 \langle u_{2,\alpha} Q_{1,\beta}^A Q_{1,\gamma}^B \rangle}{R_{1,\beta}^A R_{1,\gamma}^B}, \quad (2.12)$$

where for  $v_1$   $\alpha = x, y$ , for  $v_2$   $\kappa_{\alpha\beta\gamma} = 1$  for  $(\alpha, \beta, \gamma) = \{(x, x, x), (y, x, y), (y, y, x)\}$  and  $\kappa_{\alpha\beta\gamma} = -1$  for  $(\alpha, \beta, \gamma) = (x, y, y)$ . It is known, that  $v_n$  fluctuates significantly from event to event [50]. As was shown in [51], that the event plane method in case of ideal resolution  $R = 1$  gives observed  $\langle v_n \rangle$  equals "true"  $v_n$ . In reality, the resolution correction factor is always smaller and in a low resolution limit  $R \ll 1$  the measured  $v_n$  equals  $\sqrt{\langle v_n^2 \rangle}$ . This makes the measurement with the event plane method ambiguous.

### 2.3.3 Scalar product method

To remove the ambiguity of the event plane method, one can use a different normalization of the  $Q$ -vector. With a normalization  $Q/M$  instead of  $Q/|Q|$  one will measure  $v_n = \sqrt{\langle v_n^2 \rangle}$  independently of resolution. This method is called scalar product method.

### 2.3.4 Cumulant method

The anisotropic flow can be also estimated using the azimuthal correlation between particles. For a 2-particle correlation it can be done in a following way:

$$\langle\langle 2 \rangle\rangle \equiv \langle\langle e^{in(\varphi_1 - \varphi_2)} \rangle\rangle = \langle v_n^2 \{2\} \rangle + \delta_n \quad (2.13)$$

where the first averaging is done for particles in one event, and the second averaging is over all events,  $\delta_n$  is so-called non-flow contribution, which comes from all correlations not related to the system initial geometry (for example from resonance decays, jets, momentum conservation). To reduce the non-flow contribution, a rapidity gap can be introduced between particles. Another way to suppress non-flow is to use correlation of more than 2 particles:

$$\langle\langle 4 \rangle\rangle \equiv \langle\langle e^{in(\varphi_1 + \varphi_2 - \varphi_3 - \varphi_4)} \rangle\rangle \quad (2.14)$$

Flow coefficients using 4-particle correlation can be calculated as:

$$v_n \{4\} = \sqrt[4]{\langle\langle 4 \rangle\rangle - 2\langle\langle 2 \rangle\rangle^2} \quad (2.15)$$

More details on cumulants one can find in [52, 53].

## 2.4 Corrections for detector azimuthal anisotropies

In case of an ideal detector, the  $Q$ -vector relation to the symmetry plane is limited only by the multiplicity of the particles within the acceptance. In reality, the detector non-uniformity in  $\varphi$  and effects from magnetic field, additional material etc., can bias the measurement. Data driven corrections for those effects were

suggested in [54].

The effect of the detector bias on the measured components of the  $u$ -vector ( $x_n$  and  $y_n$ ) can be written as follows:

$$\langle x_n \rangle_{\Psi_{SP}} = x_n + v_n a_{2n}^+ (\cos n\Psi_{SP} + \lambda_{2n}^{s+} \sin n\Psi_{SP}) \quad (2.16)$$

$$\langle y_n \rangle_{\Psi_{SP}} = y_n + v_n a_{2n}^- (\sin n\Psi_{SP} + \lambda_{2n}^{s-} \cos n\Psi_{SP}) \quad (2.17)$$

where  $\langle y_n \rangle_{\Psi_{SP}}$  and  $\langle x_n \rangle_{\Psi_{SP}}$  are unknown "true" components,  $a_{2n}^\pm = 1 \pm x_{2n}$  is the acceptance coefficient and  $\lambda_{m\mp n}^{c\pm} = \frac{v_m}{v_n} \frac{x_{m\pm n}}{a_{2n}^\pm}$  is the smallness parameter. Unbiased correlation can be recovered by applying several corrections. Ones which are relevant for this work are briefly described below.

### 2.4.1 Recentering

The recentering correction shifts the  $u_n$  vector to the nonzero values of  $c_n$  and  $s_n$  in equations Eq. 2.16 and Eq. 2.17. This effect can be corrected for by subtracting from the  $u_n$  vector components their corresponding average values: The effect of

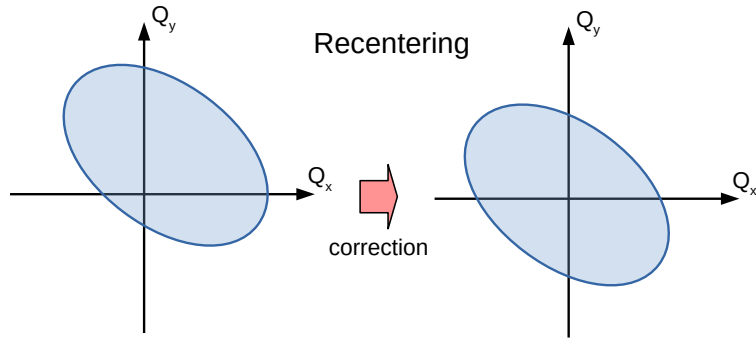


Figure 2.6: Schematic illustration of the recentering correction step.

detector bias is illustrated by the distorted shape of the distribution. In case of

an ideal detector, it should have circular shape and a center in the point  $(0,0)$ . This step corrects for shifts in both  $x$  and  $y$  directions.

### 2.4.2 Twist

In the next step correction for effective rotation of the reaction plane angle is done. It is corrected by rotation of the Q-vector distribution.

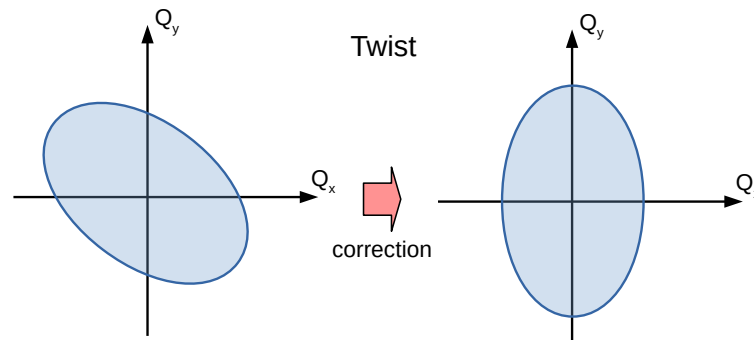


Figure 2.7: Schematic illustration of the twist correction step.

### 2.4.3 Rescaling

In the last step, which was used in this thesis, the correction for different detector sensitivities in  $x$  and  $y$  direction is done. For example, if the detector has a better acceptance in  $x$ -direction, the measured symmetry plane angle will be biased. To correct for it, the Q-vector distribution is symmetrized by rescaling.

### 2.4.4 Q-vector correction framework

All the described and more corrections were implemented in Qn-Vector Corrections Framework by J. Onderwaater, V. Gonzalez and I. Selyuzhenkov [55, 41].

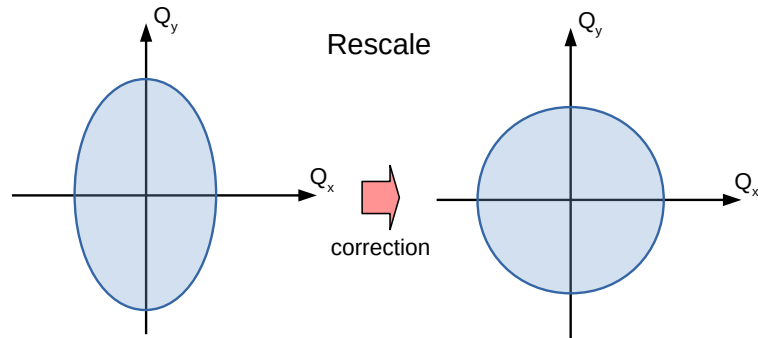


Figure 2.8: Schematic illustration of the rescale correction step.

The framework is a ROOT based C++ modular package with experiment-independent interface. Figure 2.9 illustrates the QnVector Corrections Framework performance with ALICE data [41]. After these corrections, the elliptic flow measurements with different event plane estimators are fully consistent with each other. At the moment it is a default tool for the flow analysis in ALICE. Within this work it was interfaced to CBM simulations and to NA61/SHINE data.

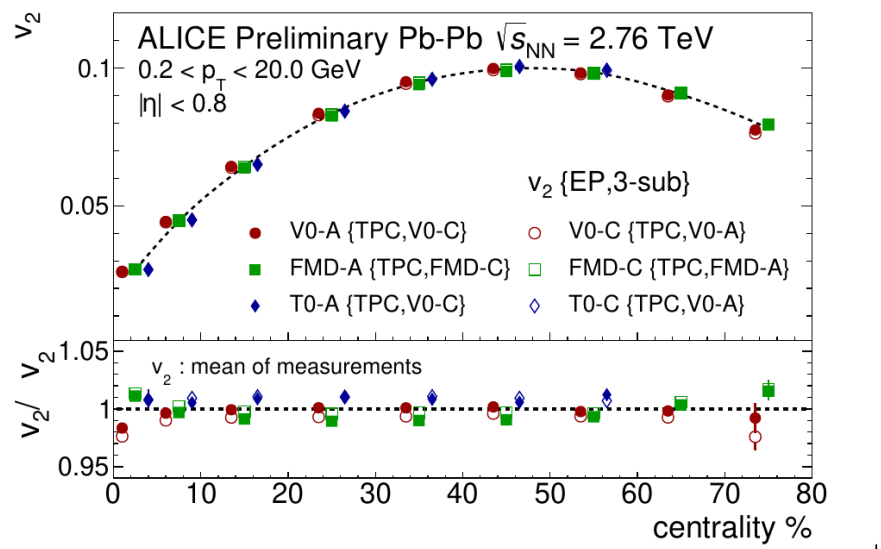


Figure 2.9: Elliptic flow  $v_2$  of charged particles estimated with event planes from different ALICE detectors.

# Chapter 3

## Fixed target experiments at FAIR and CERN SPS

### 3.1 Facility for Antiproton and Ion Research

The Facility for Antiproton and Ion Research (FAIR) is a future accelerator complex at GSI, Darmstadt, which is designed to provide high-intensity heavy-ion beams with the SIS-100 accelerator ring. It will have the ability to accelerate all ions of all chemical elements including antiprotons. The beam kinetic energy range is 2-11A GeV for gold ions and 5-11 and 14-29 GeV for protons.

Timeline for FAIR construction:

- July 2017: Groundbreaking, start of excavation and trench sheeting
- July 2018: Start of shell construction
- 2022: Buildings completed
- 2025: Completion of full facility and start of operations

The schematic view of the FAIR accelerator complex is shown in the figure [3.1](#).

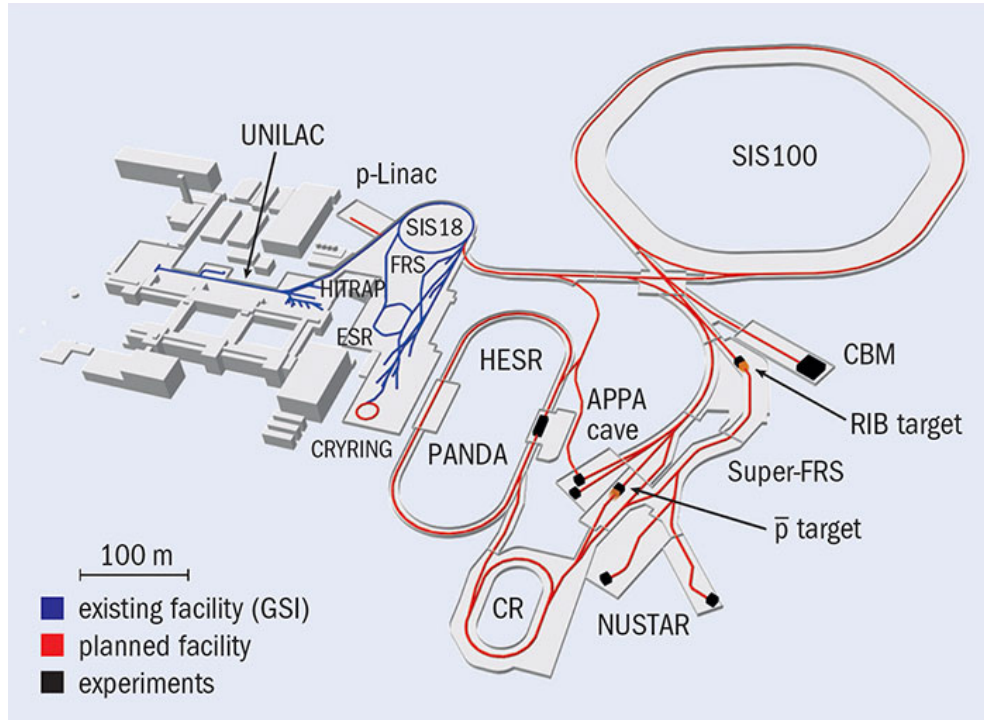


Figure 3.1: Schematic view of the Future Facility for Antiproton and Ion Research.

### 3.1.1 The Compressed Baryonic Matter experiment

It was mentioned in section Sec. 3 that there are many operating and future facilities aiming at the study of properties of QCD matter. The future Compressed Baryonic Matter experiment plays a unique role among them due to its unprecedented event rates of the order of up to  $10^7$  Au+Au collisions/sec. The rate capability of CBM is shown in the figure 3.2. Such high rates are needed to perform multi-differential measurements of rare probes which are required to contribute to the following open questions:

- Equation of state of the QCD matter
- QCD phase transition and critical point(s)
- Chiral symmetry restoration and hadron modification in a dense medium



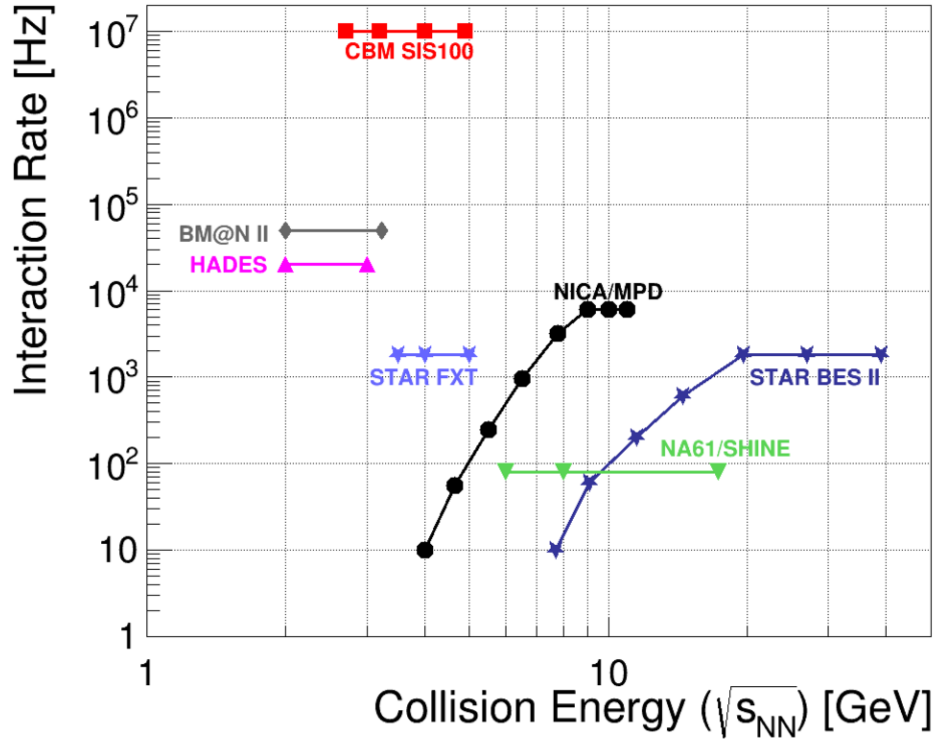


Figure 3.2: Interaction rates as function of collision energy for existing and planned heavy-ion experiments.

- Hypernuclei properties

Extreme collision rates also put challenging requirements on detector technologies and computing performance. To measure very high collision rates, fast and radiation hard detectors, and front-end electronics with free-streaming readout is needed as well as high speed data acquisition and a high performance computing farm for online event selection based on 4 dimensional (space+time) event reconstruction.

### Physics program

To address the physics questions mentioned above, CBM will perform comprehensive measurements of the following observables:

- Hadron yields, collective flow, correlations, fluctuations
- Production of (multi-)strange hyperons ( $K$ ,  $\Lambda$ ,  $\Sigma$ ,  $\Xi$ ,  $\Omega$ ) at (sub)threshold energies
- In-medium modifications of light vector mesons  $\rho$ ,  $\omega$ ,  $\phi$   $\hat{+}$   $e^+ + e^-$  ( $\mu^+ + \mu^-$ ) via dilepton measurements
- Hypernuclei lifetimes and yields
- Charm production and propagation at threshold energies
- Excitation function in p+A collisions ( $J/\psi$ ,  $D^0$ ,  $D^{+-}$ )
- Charmonium suppression in cold nuclear matter

This thesis is dedicated to CBM performance for anisotropic flow measurements.

### Experimental setup

The CBM experimental setup is shown in the figure 3.3. It comprises the following components:

- a superconducting dipole magnet (needed for momentum measurement of charged particles);
- a Micro Vertex Detector (MVD) consisting of four layers of silicon monolithic active pixel sensors (displaced vertices reconstruction);
- a Silicon Tracking System (STS) based on double-sided silicon micro-strip sensors arranged in eight stations inside a dipole magnet (main tracking detector);
- a Time-of-Flight wall (TOF) based on Multi-Gap Resistive Plate Chambers (MRPC) with low-resistivity glass (charged hadrons identification);

- a Ring Imaging Cherenkov (RICH) detector comprising a CO<sub>2</sub> radiator and a UV photon detector realized with multi-anode photomultipliers for electron identification (electron and pion identification);
- a Transition Radiation Detector (TRD) (pion suppression, particle tracking, and identification using specific energy loss);
- a Muon Chamber (MuCh) system for muon identification consisting of a set of gaseous micropattern chambers sandwiched between hadron absorber plates made of graphite and iron;
- an Electromagnetic Calorimeter (ECAL) (measurement of photons);
- a Projectile Spectator Detector (PSD) (event characterization, event plane);
- a First-Level-Event-Selection (FLES) system (online event reconstruction and selection).

**Dipole magnet** The magnet houses the Silicon Tracking System (STS) and provides a magnetic field integral of 1 Tm [56]. With this magnetic field the STS is able to reconstruct tracks with a momentum resolution of  $\Delta p/p = 1.5\%$ . The magnet gap has a height of 144 cm and a width of 300 cm to accommodate the STS. The maximum magnetic field is around 1 T. The energy stored in the magnet is about 5 MJ. The magnet will be self-protecting. However, in order to limit the temperature rise to 100 K in case of a quench, the energy will be dumped in an external resistor. The implementation of the magnet geometry in CBMROOT is shown in figure 3.4.

**Micro Vertex Detector** The micro-vertex detector is designed to provide high resolution secondary vertices reconstruction of short lived particles such as  $D^0$  ( $D^\pm$ )-mesons (decay length  $c\tau = 124$  (314)  $\mu\text{m}$ ). To reduce multiple scattering

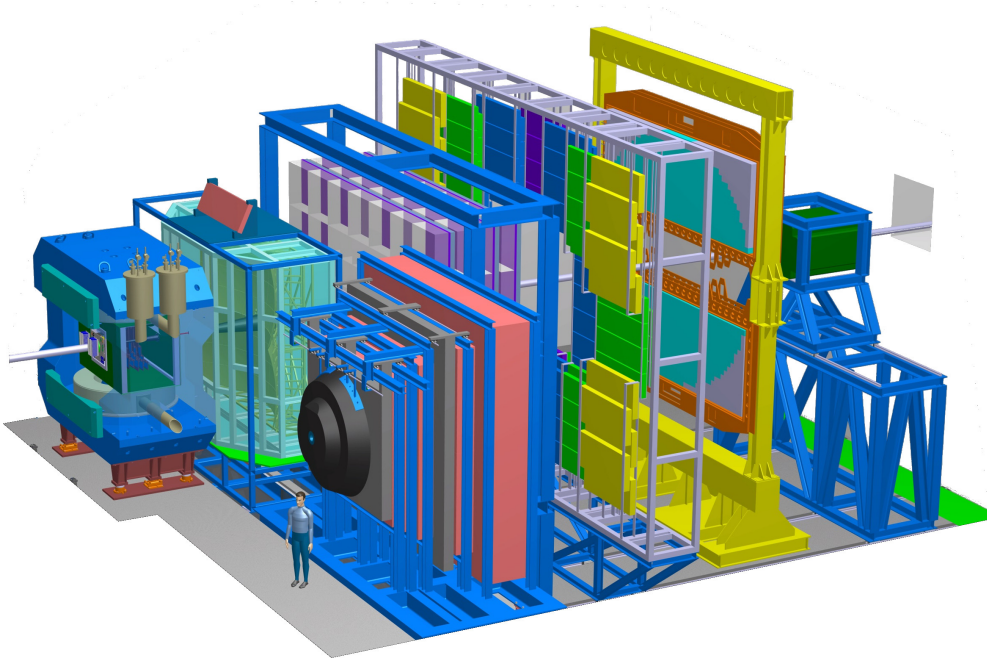


Figure 3.3: The CBM experimental setup. For muon measurements, the RICH detector will be replaced by the MuCH, which is shown to the right of the beam axis.

inside the detector, the MVD has a very low material budget of 300-500  $\mu\text{m}$  silicon equivalent for sensors and support structures. The detector consists of three stations of monolithic active pixel sensors (MAPS). They are located at distances 5, 10, 15 and 20 cm downstream from the target. The transverse pixel size of about 18-20  $\mu\text{m}$  will allow to reconstruct secondary vertices with resolution of 50-100  $\mu\text{m}$  along the beam axis. Schematic view of the MVD detector is shown in the figure 3.5. All four stations have different size and number of sensors to have similar acceptance.

**Silicon Tracking System** The Silicon Tracking System (STS) [57] is the core detector of the CBM setup. It is located inside the dipole magnet, which allows for measurement of the momentum of charged particles. With 8 layers of silicon double-sided strip sensors it has a momentum resolution up to 1.5%. The sensors

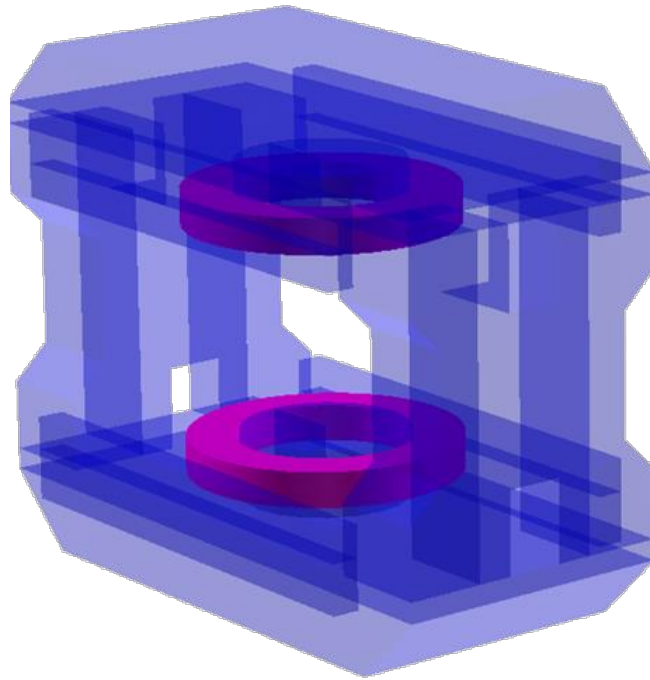


Figure 3.4: CBM Dipole magnet geometry implementation in CBMROOT (geometry version 18a).

are located at distances between 30 and 100 cm from the target. A low material budget is achieved with  $300 \mu\text{m}$  thick sensors, carbon ladders and microcables. A schematic view of the STS is shown in figure 3.6.

**Ring Imaging Cherenkov detector** The task of the Ring Imaging Cherenkov [58] detector is to identify electrons in a momentum range up to 8-10  $\text{GeV}/c$ . The identification technique is based on the measurement of Cherenkov radiation emitted by charged particles passing a radiator. Adjusting the refractive index of a radiator material one can achieve a signal from electrons, but keep the pions below light production threshold. In CBM the gaseous  $\text{CO}_2$  will be used as radiator. The light will be focused by spherical mirrors, and will be measured with photo-multipliers. In the CBM setup, the RICH detector will be placed after the dipole magnet and the STS in front of the Transition

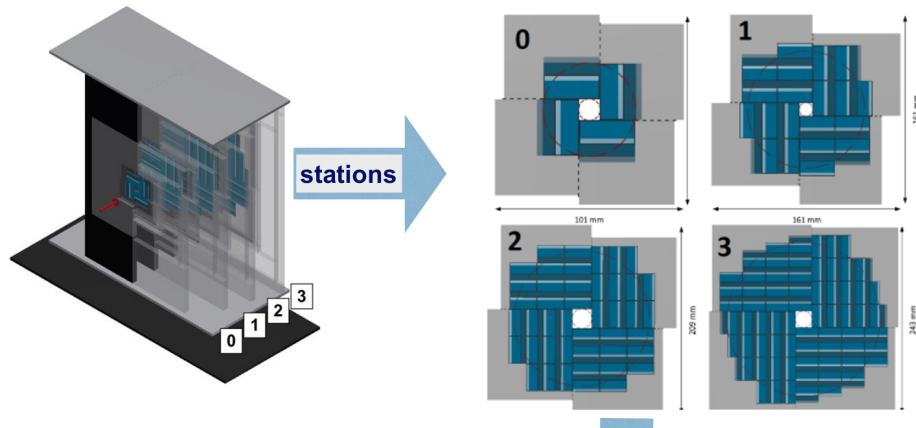


Figure 3.5: Schematic view of the Micro Vertex Detector.

Radiation Detector at the distance about 1.6 m downstream of the target.

**Transition Radiation Detector** Three Transition Radiation Detector stations, each consisting of 3 detector layers, will serve for particle tracking and for the identification of electrons and positrons with momentum  $p > 1.5 \text{ GeV}/c$  ( $\gamma > 1000$ ) [59]. They are located at distances approximately 5 m, 7.2 m and 9.5 m downstream the target. In order to keep the occupancy below 5% for central heavy-ion collisions, the minimum size of a single cell should be about  $1 \text{ cm}^2$ . The pion suppression factor obtained with 9 TRD layers is estimated to be well above 100 at an electron efficiency of 90%.

**Muon Chamber** Measuring and identifying low-momentum muons in heavy-ion collisions is experimentally challenging. In CBM that is planned to achieve using a hadron absorber system to suppress the contributions from all other particle species. Between the absorber walls, tracking stations (triplets) are placed. The hadron absorbers vary in material and thickness, and the tracking stations consist of detector triplets based on GEM and MRPC technologies [60]. The MuCh system is placed downstream from the STS stations. To reduce the number of background muons from pion and kaon weak decays, the detector system

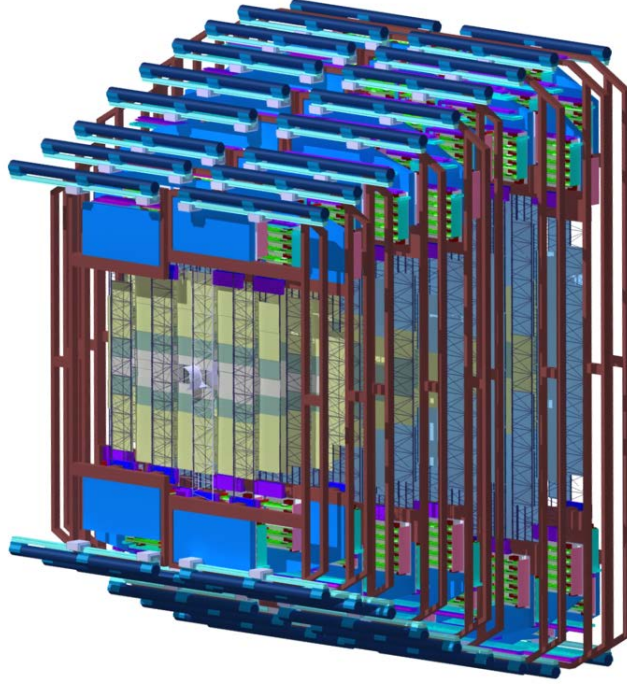


Figure 3.6: Schematic view of the Silicon Tracking System.

has to be as short as possible.

**Time-of-Flight detector** Measuring Time-of-Flight allows to identify charged particles after matching the hit in TOF with the corresponding track measured in the STS. A particle mass  $m$  can be calculated using time-of-flight  $t$ , track length  $l$  and momentum  $p$  in a following way:

$$m^2 = p^2 \left( \frac{1}{\beta^2} - 1 \right); \quad \beta = \frac{l}{t} \quad (3.1)$$

To obtain sufficient separation between different particle species (mostly protons, kaons and pions), a time resolution better than 80 ps is needed [61]. For an acceptance coverage close to the one of the STS total size of the TOF wall placed at a distance of 7 m downstream the target has to be  $12 \times 9 \text{ m}^2$ . To achieve those goals a TOF wall consisting of state-of-the-art Multigap Resistive Plate Chambers (MRPC) is under construction. A schematic view of the TOF wall is shown

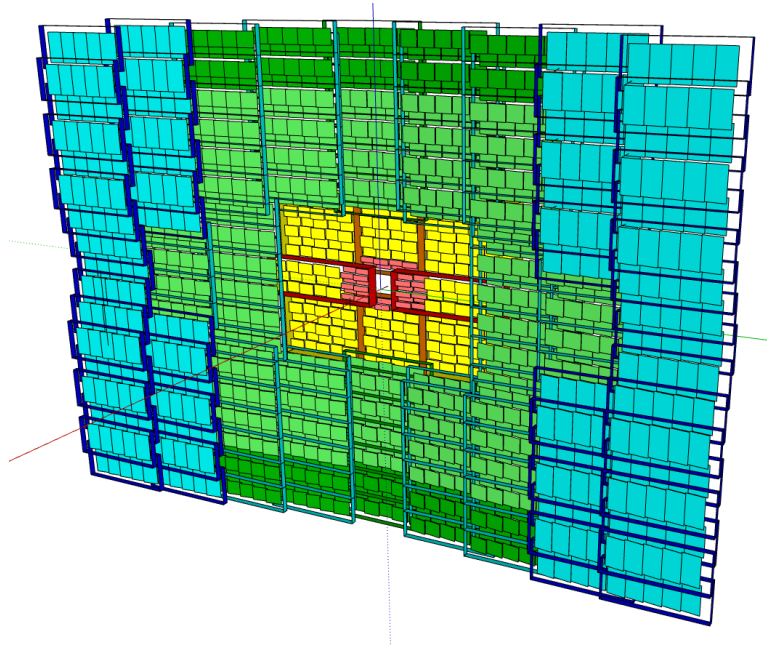


Figure 3.7: Schematic view of the Time-of-Flight wall.

in figure 3.7.

**Electromagnetic Calorimeter** A "shashlik" type calorimeter will be used to measure direct photons and photons from neutral meson decays. The ECal will be composed of modules which consist of 140 sandwiched lead and scintillator layers. The ECal is not a part of the day-one setup.

**Projectile Spectator Detector** The main purpose of the Projectile Spectator Detector [62] is to provide experimental information of the heavy-ion collision centrality, and the orientation of its symmetry plane. The detector is designed to measure the energy distribution of the projectile nucleus fragments (spectators), and the forward going particles produced close to beam rapidity. The transverse layout of the PSD is shown in the figure 3.8 with different colors indicating parts (PSD1, PSD2, PSD3) with different sensitivity to spectators. The PSD has 44 modules and covering polar angles of  $0.21^\circ < \Theta < 5.7^\circ$  ( $4.3^\circ$ ) at a distance of 8 m from the target. The angular acceptance is optimized for the FAIR energy



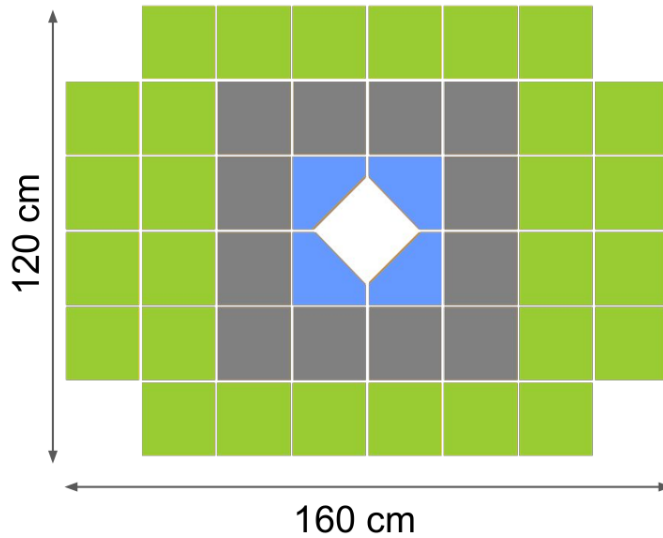


Figure 3.8: Transverse layout of the Projectile Spectator Detector. With different colors regions with sensitivity to spectator fragments are highlighted.

range  $\sqrt{s_{NN}}=2.7-4.8$  GeV. The PSD has a rectangular hole of size 20 x 20 cm in the center which is needed to avoid radiation damage at high beam intensities expected at CBM. The PSD is sensitive to spectator fragments (central modules) and produced particles (outer modules).

**First-Level-Event-Selection** The CBM physics program includes the measurement of particles with very small production cross-section which requires high reaction rates. The CBM experiment is designed for operation at interaction rates up to 10 MHz, which corresponds to a beam intensity of  $10^9$  ions/s, and a 1% interaction target. The bandwidth of 10 GByte/s can be achieved with modern optical fibers and transceivers. To perform measurements at 10 MHz, a trigger is needed. There are no simple observables to implement a hardware trigger, so an online software trigger will be used. Track reconstruction and selection of short-lived particles will be done online by the existing computer farm (GSI GreenIT Cube) using many-core processors. Only events of interest will be

stored.

## 3.2 Super Proton Synchrotron @ CERN

The Super Proton Synchrotron (SPS) is a particle accelerator at The European Organization for Nuclear Research (CERN). It was commissioned in 17 June 1976

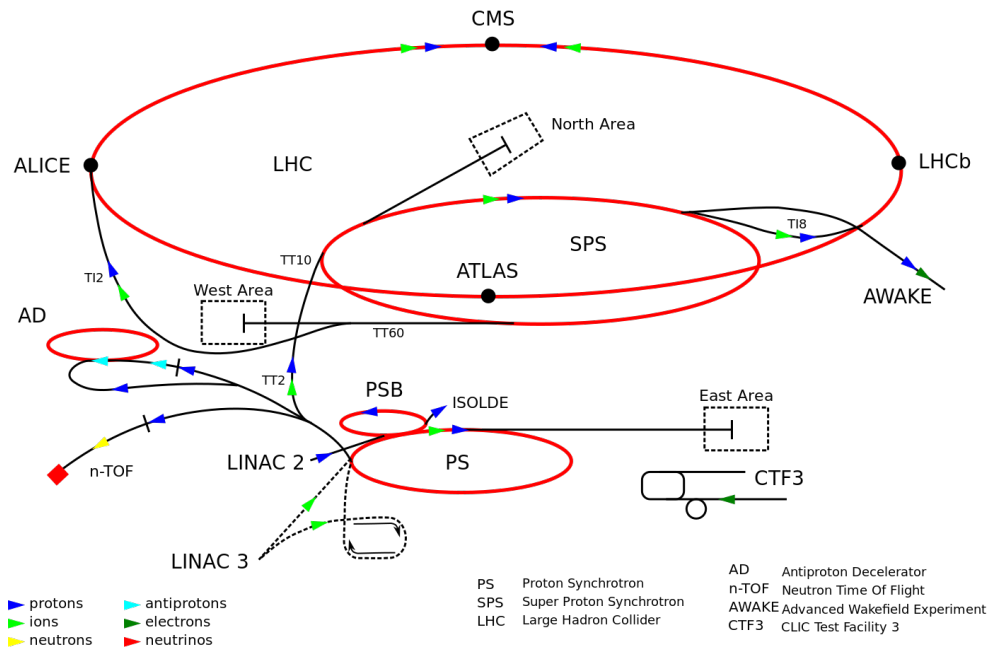


Figure 3.9: The Super Proton Synchrotron as part of current particle accelerator complex at CERN.

and is still operating. The maximum energy for proton acceleration is 450 GeV, for heavy-ions is around  $150A$  GeV . Nowadays it is mainly used as an injector for high-intensity proton and lead beams for the Large Hadron Collider (LHC). Besides that, SPS is used to provide beams to several fixed target experiments, such as NA61/SHINE, NA62 and COMPASS.

### 3.2.1 NA61/SHINE experiment

NA61/SHINE (standing for "SPS Heavy Ion and Neutrino Experiment") is a particle physics experiment is placed at Super Proton Synchrotron (SPS) in the H2 beamline of the North Area (NA).

The NA61/SHINE physics goals include:

- Search for the onset of deconfinement and for the critical point of strongly interacting matter which is pursued by investigating p+p, p+Pb and nucleus-nucleus collisions
- precise hadron production measurements for improving calculations of the initial neutrino beam flux in the long-baseline neutrino oscillation experiments as well as for more reliable simulations of cosmic-ray air showers.

The detector system is shown in the figure 3.10 and includes:

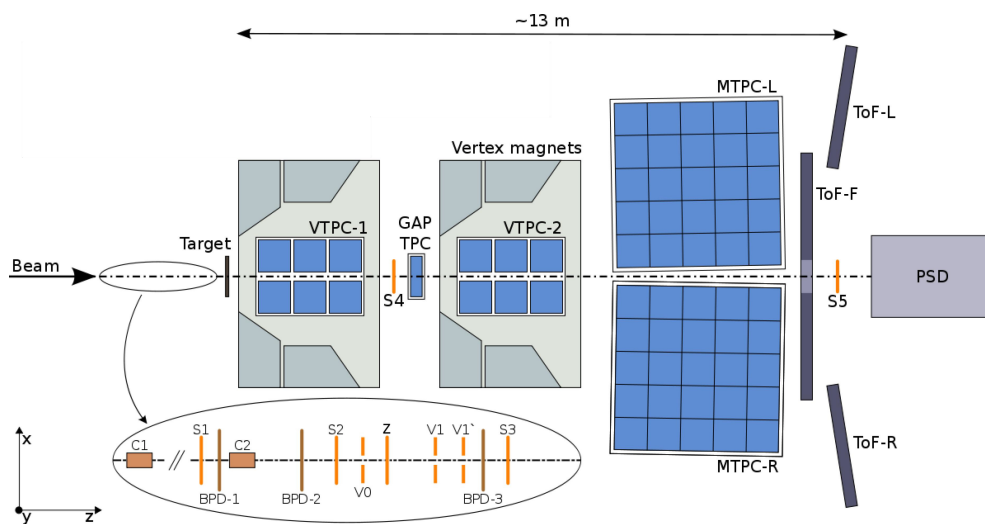


Figure 3.10: Layout of the NA61/SHINE experiment.

- several Time Projection Chambers
- Projectile Spectator Detector (PSD)
- two Time-of-Flight walls
- Trigger and Beam Position Detectors (BPD)

### Time Projection Chambers

In the NA61/SHINE experiment the measurement of particle trajectories and ionization energy loss ( $dE/dx$ ) is provided by four Time Projection Chambers (TPC). Two of them are located inside a dipole magnets, called Vertex-TPC(1,2) (VTPC1 and VTPC2) and contribute mainly to momentum measurements. They have a gas volume of 200 x 250 x 67 cm each, and are divided into two sensitive volumes located at each side from the beam. The other two TPCs are located outside the magnetic field, called Main-TPC(Left, Right) (MTPCL and MTPCR). They have a much larger volume of 390 x 390 x 112 cm and provide most of the  $dE/dx$  sensitivity. There are also additional small chamber Gap-TPC (GTPC) placed on the beamline between the VTPCs to provide momentum determination of high momentum particles, and two Forward-TPCs (FTPC) to supplement forward tracking.

### Projectile Spectator Detector

NA61/SHINE Projectile Spectator Detector is a hadron calorimeter designed to measure forward rapidity particles (projectile spectators). The transverse layout

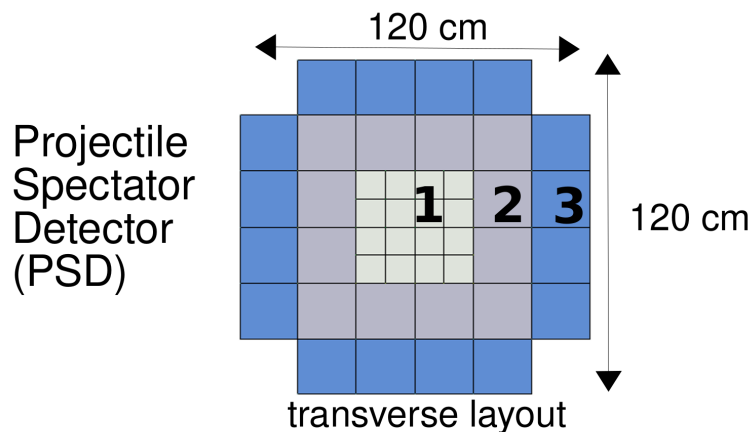


Figure 3.11: Transverse layout of the Projectile Spectator Detector. With different colors regions with sensitivity to spectator fragments are highlighted.

is shown in figure 3.11. It consists of 44 long modules and one additional short module. The central part of the detector has a better granularity with transverse module size 10 x 10 cm (16 modules). All other modules have size 20 x 20 cm. One more short module with a size 20 x 20 cm is located in front all other in the center to decrease shower leakage from the high energy heavy-ion beam particles. This short module has only two sections in longitudinal direction, while the long modules have ten sections. The design is similar to the CBM PSD, it is described in section 3.1.1. The Projectile Spectator Detector is sensitive mostly to spectator fragments (outer modules are also sensitive to produced particles), and is used for event (centrality) classification and reaction plane determination.

### **Trigger and Beam Position Detectors**

The trigger system consists of scintillator counters (S1, S2, S3) which also can be used for beam particle identification (in case of secondary beams) and veto scintillator counters (V1, V2) with a hole in the middle to reject off-target interactions, a charge detector (Z) and an interaction trigger detector (S4). For beam position and direction determination three Beam Position Detectors (BPDs) are used. Each of them is a wire chamber detector, and fist the BPD is located at a distance of about 30 m upstream of the target.

### **Time-of-Flight detector**

Two Time-of-Flight walls are placed downstream from the MTPCs. They are designed to cover kaons at midrapidity at SPS collision energies. Each of the TOF array consists of about 1000 scintillators which are read out by two photomultiplier tubes. The time resolution of the measurement is approximately 60 ps. Additionally, the total deposited charge is measured to distinguish double hits. Measured TOF hits are assigned to the closest extrapolated track.

# Chapter 4

## Calibration tools and analysis frameworks

This chapter describes the preparatory work, namely the tuning of event and track cuts, data quality assurance (QA), calibration and development of analysis frameworks (centrality, particle identification). It is organized in the following way:

- Dataset description of NA61/SHINE data and CBM simulation with track and event cuts
- Calibration of NA61/SHINE data
- Centrality Framework description and obtained results
- Particle Identification Framework description and obtained results

The flow results presented in chapter 5 are based on this preparatory work.

## 4.1 CBM simulation setup

### 4.1.1 Event generators

In this work simulations have been performed using the Ultra relativistic Quantum Molecular Dynamics (UrQMD) event generator [63, 64], and the Dubna Cascade Model with the Quark Gluon String Model (DCM-QGSM) and the Statistical Multifragmentation Model (SMM) [65] as afterburner.

UrQMD is a Monte Carlo event generator for proton-proton, proton-nucleus, and nucleus-nucleus collisions developed at the Goethe University. In the standard mode it is based on the propagation of hadrons, and provides a solution for the relativistic Boltzman equation. There are no spectator fragments in this model. All spectators are protons and neutrons.

In the DCM-QGSM code spectator fragments are formed by the coalescence process. After that, further decay of the excited and unstable nucleus is done with the SMM afterburner. In the end, the most realistic description of spectator fragment formation available on the market is used for this simulation.

### 4.1.2 Datasets

To study the CBM physics performance, a set of simulations was performed. The first set is dedicated to flow performance studies, and consists of 3M Au+Au collisions at a beam momentum of 10A GeV/c simulated with the UrQMD event generator. The CBM detector response for those collisions is simulated with the GEANT3 [66] transport code, and a realistic digitization and reconstruction is done in CBMROOT version Jul17. The PSD geometry consists of 44 modules and has a rectangular hole of size 20 x 20 cm in the center (diamond shape).

The second set of simulations is dedicated to the study of the PSD hole size effect on the performance of flow and centrality estimation. It consists of 300k



Au+Au collisions at 10A GeV/ $c$  simulated with DCM-QGSM event generator with spectators coalescence and statistical multifragmentation (SMM). The CBM detector response is simulated with GEANT4 [67] and CBMROOT version Jul17. Three different simulations with PSD hole sizes of 0, 7 and 20 cm were performed.

The details are summarized in the table 4.1.

Table 4.1: Simulated datasets used in this thesis.

Model	UrQMD	DCM-QGSM-SMM
System	Au+Au	Au+Au
Beam momentum	10A GeV/ $c$	10A GeV/ $c$
PSD geometry	44 modules hole size 20 cm	44 modules hole size 0, 7, 20 cm
Transport code	GEANT3	GEANT4
Detector response	CBMROOT Jul17	CBMROOT Jul17

### 4.1.3 Event selection

The list of event cuts used for CBM performance studies is presented below:

- Existence of the primary vertex and a good fit quality  $\chi^2_{vertex\ fit}$  of the reconstructed vertex:

$$\checkmark \quad 0.5 < \chi^2_{vertex\ fit} < 1.5$$

- Position of the reconstructed primary vertex to select events with vertex position close to the target region:

$$\checkmark \quad -0.1 < Z_{vertex}(cm) < 0.1$$

$$\checkmark \quad -0.1 < X_{vertex}(cm) < 0.1$$

$$\checkmark \quad -0.1 < Y_{vertex}(cm) < 0.1$$

#### 4.1.4 Track selection

Track cuts used to select primary particles with a good track fit quality are listed below:

- Total number of hits in the STS+MVD is larger than 3 to assure sufficient momentum resolution:

$$\checkmark N_{hits}(STS + MVD) > 3$$

- Number of hits associated to the track is required to be more than 70% of the maximum number of points along the particle trajectory to avoid track splitting (hardcoded cut in track reconstruction procedure):

$$\checkmark N_{hits}^{total} / N_{hits}^{potential} > 0.7$$

- Distance of closest approach of the track to the primary vertex normalized on its errors less than 3 to select primary particles:

$$\checkmark \chi_{vertex}^2 < 3$$

The azimuthal angle  $\varphi$  vs. transverse momentum  $p_T$  distribution is shown in the figure 4.1 for MC-true protons (left) and MC-true positively charged pions (right). Non-uniformity in  $\varphi$  is observed for both protons and pions. Positively charged particles are deflected by the magnetic field which causes this non-uniformity.

The pseudorapidity  $\eta$  vs. transverse momentum  $p_T$  distribution for all selected tracks is shown in the figure 4.2. In the plane pseudorapidity versus transverse momentum, the phase space acceptance is more uniform. The CBM detector has transverse momentum coverage to very low  $p_T$ .

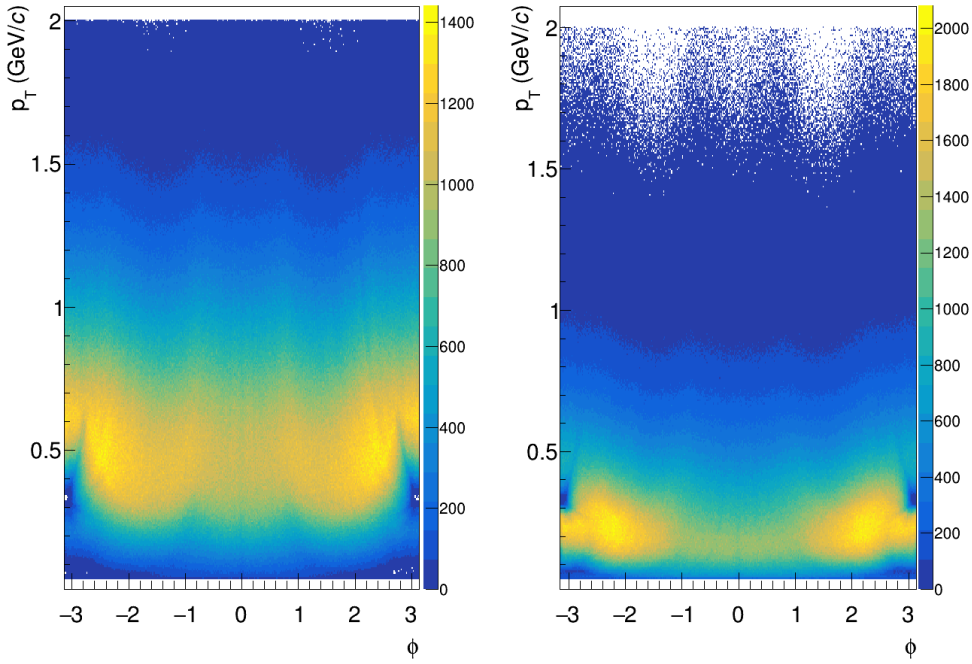


Figure 4.1: Azimuthal angle  $\varphi$  distribution vs. transverse momentum  $p_T$  for MC-true protons (left) and MC-true positively charged pions (right) after track selection.

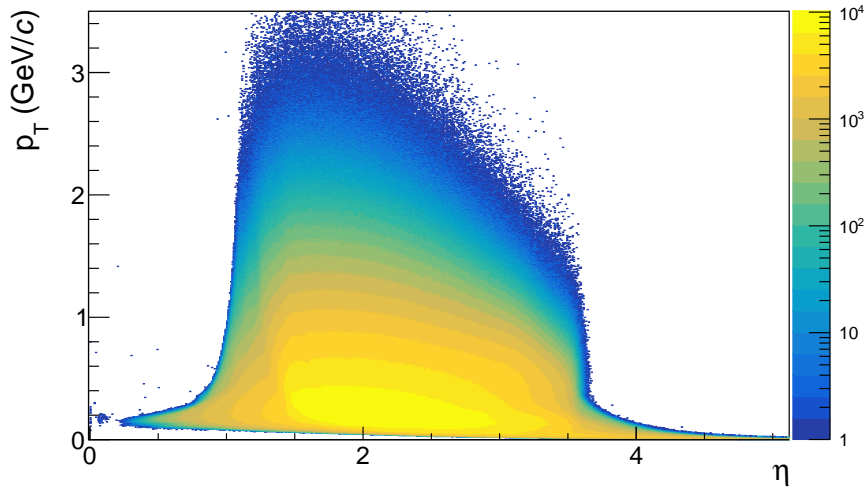


Figure 4.2: Pseudorapidity  $\eta$  distribution vs. transverse momentum  $p_T$  for all charged particles reconstructed with STS+MVD after track selection.

## 4.2 NA61/SHINE data

A sample of Pb+Pb collisions at 30A GeV/c collected in 2016 was used for the analysis. The approximate number of events for each trigger as well as trigger definitions can be found in the table 4.2. About 10% of the data were collected with target removed configuration.

Table 4.2: Trigger definitions and approximate number of collected events for Pb+Pb @ 30A GeV/c .

Trigger	Definition	Number of events
T1 (beam)	$S1 * S2 * V1bar$	
T2 (central)	$S1 * S2 * S3bar * V1bar * PSD$	
T3 (beam)	$S1 * S2$	
T4 (minbias)	$S1 * S2 * S3bar * V1bar$	

### 4.2.1 Event selection

The event cuts can be divided into two categories: biasing and non-biasing. Non-biasing event cuts use only information from the detectors upstream from the target. They have no impact on collision selection and cannot contribute to systematic biases. The main purpose of those cuts is to select beam particles with a desired position and direction (in case of secondary beams also identify the projectile particle type).

Biasing event cuts are cutting on variables which characterize beam interaction with the target. They bias the selected events, especially for low multiplicity collisions. The list of non-biasing cuts is presented below:

- Beam position cut (BPD) to remove beam outlayers

$$\checkmark \quad -0.5 < BPD1_x (cm) < 0.3$$

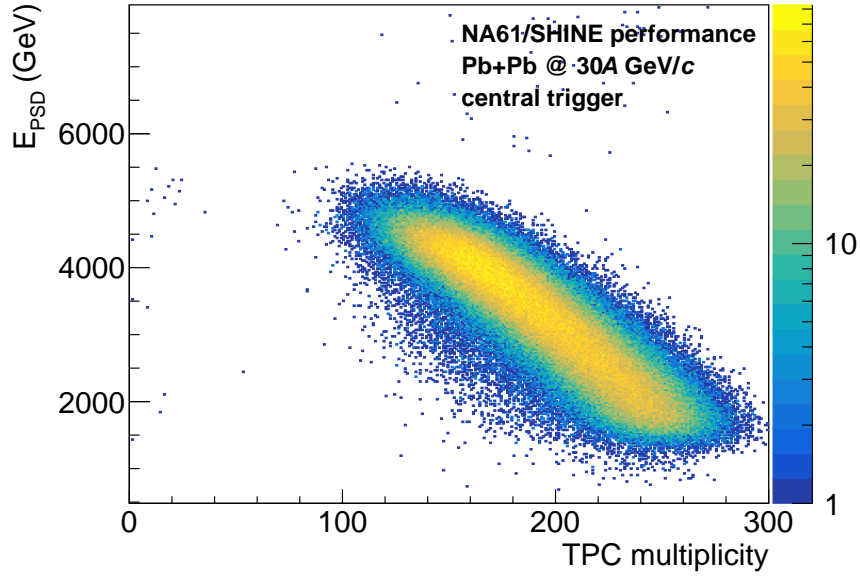


Figure 4.3: PSD energy vs. multiplicity correlation for central T2 trigger.

- ✓  $-0.7 < BPD1_y (cm) < 1.1$
- ✓  $-0.7 < BPD2_x (cm) < -0.1$
- ✓  $-0.4 < BPD2_y (cm) < 0.3$
- ✓  $-1.05 < BPD3_x (cm) < 0.35$
- ✓  $-0.55 < BPD3_y (cm) < 0.05$
- Multi-Hit Time Digital Converter cut (sometimes referred as WFA cut) to reject off-time particles, that come too close with the triggered particle
  - ✓  $WFA_{beam} (T1) < 4000 ns$
  - ✓  $WFA_{interaction} (T4) < 25000 ns$
- S1 and S2 cuts to select beam particles with appropriate charge (Pb beam is primary, but the cut still is used to remove tails of the distribution)

The list of biasing cuts is presented below:

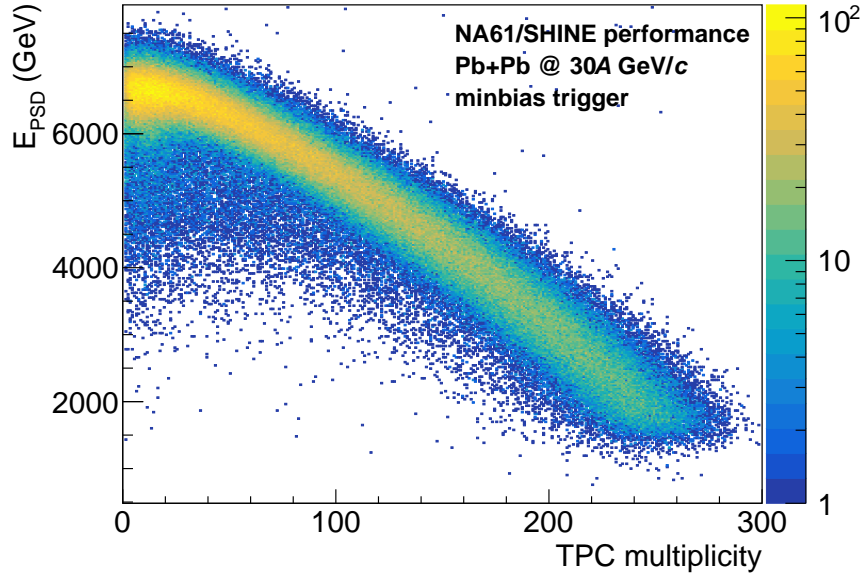


Figure 4.4: PSD energy vs. multiplicity correlation for minimum bias T4 trigger.

- Existence of the primary vertex and a good fit quality of the reconstructed vertex

$$\checkmark \quad 0.5 < \chi_{vertex\ fit}^2 < 1.5$$

- Position of the reconstructed primary vertex to select events with vertex position close to the target region

$$\checkmark \quad -593 < Z_{vertex} (cm) < -591$$

$$\checkmark \quad -0.35 < X_{vertex} (cm) < 0.3$$

$$\checkmark \quad -0.37 < Y_{vertex} (cm) < 0.08$$

After event selection, the available statistics for configuration with magnetic field and target inserted is 1.1 M events for the minimum bias trigger T4 and 0.6 M events for the central trigger T2 which was fully efficient in the 0-15% centrality class.

### 4.2.2 Tracks selection

Track cuts used to select primary particles with a good track fit quality are listed below:

- "Good" track status (track status = 0)
- Total number of clusters in the TPCs larger than 30 (to have large enough number of cluster for  $dE/dx$  calculation) and number of clusters in the vertex TPCs larger than 15 (large enough number of clusters in magnetic field to allow for a good momentum resolution):

$$\checkmark N_{clusters}(VTPC1 + VTPC2) > 15$$

$$\checkmark N_{clusters}(Total) > 30$$

- Number of hits associated to the track was required to be more than 55% of the maximum number of points along the particle trajectory to avoid track splitting:

$$\checkmark N_{clusters}(Total)/N_{clusters}^{potential} > 0.55$$

$$\checkmark N_{clusters}(Total)/N_{clusters}^{potential} < 1.1$$

- Distance of closest approach to the primary vertex in the plane transverse to the beam direction less than 2 cm in  $x$  direction and less than 1 cm in  $y$  direction to select primary particles (different values of the cut in  $x$  and  $y$  direction are due to tracks bending in  $x$  direction in the magnetic field):

$$\checkmark |b_x| < 2 \text{ cm}$$

$$\checkmark |b_y| < 1 \text{ cm}$$

The azimuthal angle  $\varphi$  vs. pseudorapidity  $\eta$  distribution for selected tracks is shown in the figure 4.5. The detector acceptance is non-uniform in azimuthal angle, which is connected to Vertex TPCs geometry - they consist of two sensitive

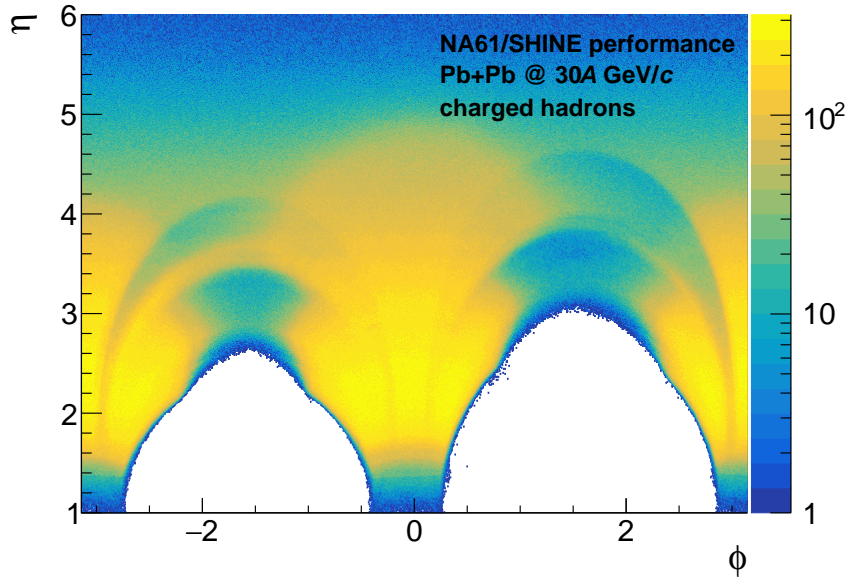


Figure 4.5: Azimuthal angle  $\varphi$  distribution vs. pseudorapidity  $\eta$  for all charged particles after track selection.

volumes located on each side (left and right) from the beam. That results in "holes" in the acceptance at  $+\pi/2$  (above the beam) and  $-\pi/2$  (below the beam). The size of those holes is different because the beam was not centered with respect to the VTPC and was shifted by around 20 cm above the center. The "hole" size is becoming larger for tracks with smaller pseudorapidity.

The transverse momentum  $p_T$  vs. pseudorapidity  $\eta$  distribution for selected tracks is shown in the figure 4.6. In pseudorapidity and transverse momentum the phase space acceptance is more uniform. There are two structures at  $3 < \eta < 4$  and  $3.5 < \eta < 4.5$  which corresponds to tracks starting from VTPC1 and VTPC2. VTPC2 provides coverage to a very forward rapidities which in combination with fixed-target geometry allows for unique measurements of flow in this kinematic region.

The azimuthal angle  $\varphi$  vs. transverse momentum  $p_T$  distribution for selected tracks is shown in the figure 4.7. NA61/SHINE spectrometer provides coverage to



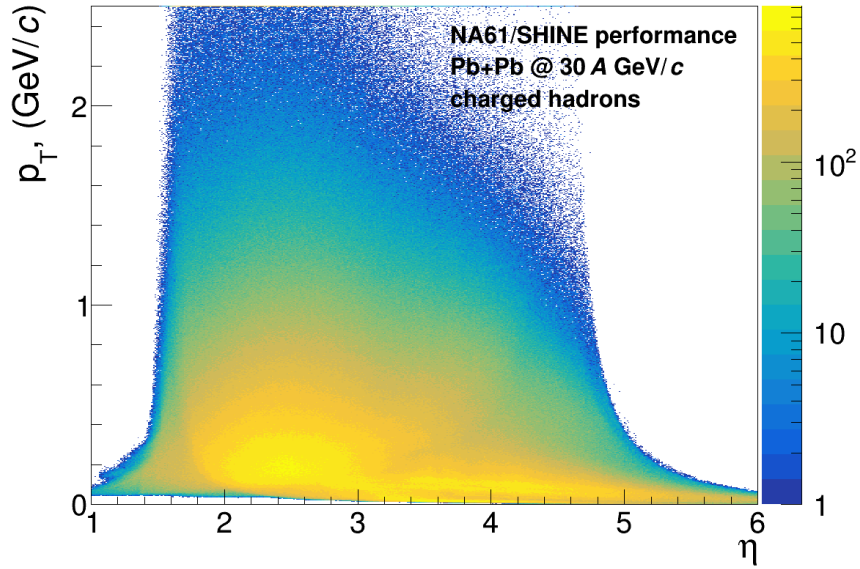


Figure 4.6: Transverse momentum  $p_T$  vs. pseudorapidity  $\eta$  for all charged particles after track selection.

very low transverse momentum down to  $p_T = 0$ . Similarly to figure 4.5 the "hole" in azimuthal angle acceptance is observed. It is less visible at low transverse momenta  $p_T < 0.3$  GeV/c .

Charged pion and proton identification was based on specific energy loss  $dE/dx$  in the TPCs. The details of particle identification will be discussed in the Chapter 4.4.

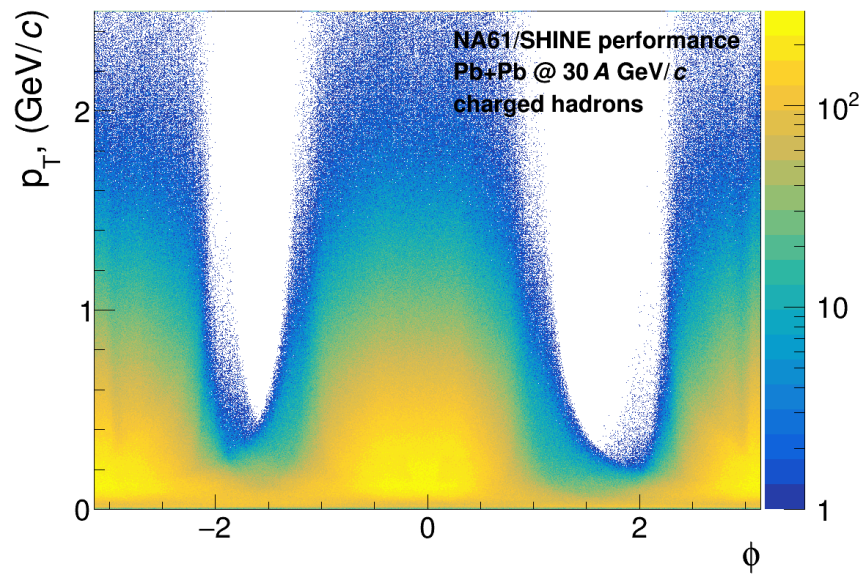


Figure 4.7: Azimuthal angle  $\varphi$  vs. transverse momentum  $p_T$  for all charged particles after track selection.

## 4.3 NA61/SHINE TPC calibration

Before obtaining any physics results, the detector which was used for any kind of measurement has to be calibrated. In case of the NA61/SHINE experiment, the main detectors are TPCs. There are several parameters of TPCs which require calibration. The main ones are drift velocity  $v_D$ , detector position in space and so-called  $T_0$  value which is connected with electronics reaction time. Within this work NA61/SHINE TPCs were calibrated. The procedure was performed in 4 major Stages, which will be discussed in details later:

- Stage 1: global  $T_0$  and Multihit time-to-digital converter calibration
- Stage 2: drift velocity  $v_D$
- Stage 3: chamber  $T_0$
- Stage 4: chamber positions in  $y$ -direction (alignment)

For Stages 1 and 3 only the functionality of the SHINE Framework was used. The calibration procedure was developed by Peter Kövesarki and Andras Laszlo [68, 69]. It was tested and approved during this work. For Stages 2 and 4 a program was developed in addition to the basic SHINE functionality.

### 4.3.1 Global $T_0$ calibration (Stage 1)

This Stage takes as an input raw data and does not need unpacking of TPC data. The first component (so-called global  $T_0$  calibration) calibrates the time-to-digital converter (TDC) which measures the time phase between  $S_{1_1}$  and the start of the TPC time sampling. The calibration procedure is based on the information that the phase shift between  $S_{1_1}$  and TPC time sampling spans the interval  $[0, 40]$  ns due to electronics properties. The TDC distribution window can be identified with the spanned TDC window using a linear calibration. The

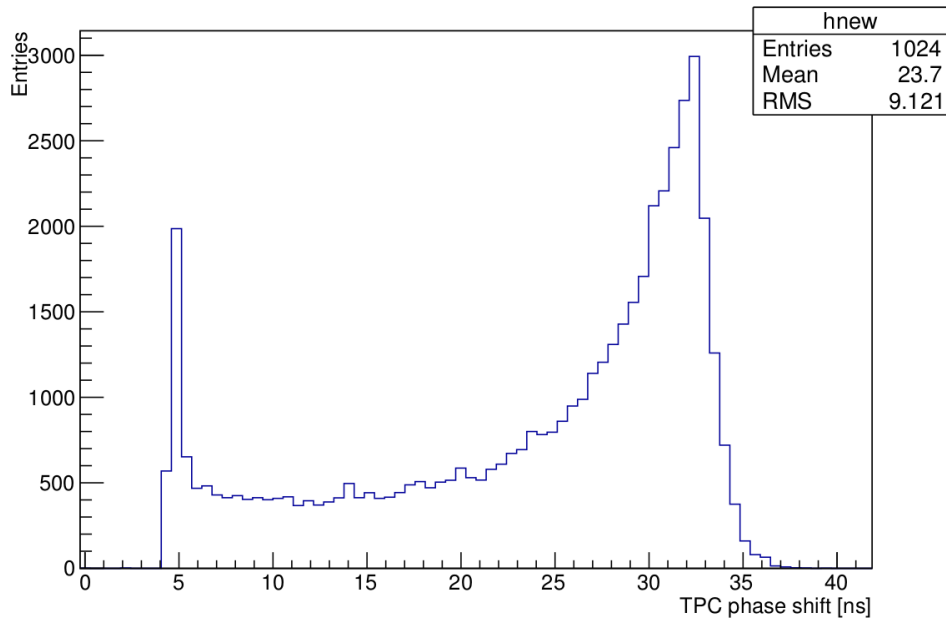


Figure 4.8: TPC time sampling (global  $T_0$  calibration).

distribution after calibration is shown in the figure 4.8. The second component calculates calibration factors for CAEN V1290N Multihit-TDC (MHTDC). The pertinent unit is triggered by the MainTrigger signal, which occurs uniquely for each event. The occurrence times of the signal of the other beam detectors (such as the  $S_{1_1}$ ) relative to the MainTrigger is recorded with a 200 ps time resolution. The timing of MainTrigger is not very accurate and the timing reference signal of NA61 is the  $S_{1_1}$ . Therefore, the reconstruction software needs to find the matching  $S_{1_1}$  signal to the MainTrigger and needs to recalculate the occurrence times relative to that.

The calibration module correlates the occurrence times of  $S_{1_1}$  relative to MainTrigger and determines the unknown most probable time shift between the two along with a narrow acceptance window, in order to avoid matching the of MainTrigger to off-time  $S_{1_1}$  hits.

### 4.3.2 Drift velocity calibration (Stage 2)

This stage calibrates drift velocity in all chambers. First, track reconstruction using drift velocity measured with detector control system (DCS) is done. The DCS measurement precision is usually about 1%, which is 10 times worse than is needed for a final reconstruction. Then, global tracks are splitted into segments for each TPC and refitted as local tracks. Local tracks in different TPCs are extrapolated to a common plane and a distance in  $y$ -direction is calculated:

$$\Delta y = y_\alpha - y_\beta \quad (4.1)$$

where  $\alpha$  is a TPC we want to calibrate,  $\beta$  is a reference TPC or TOF (in case of TOF, extrapolation is done to a TOF position and  $y_{TOF}$  is a coordinate of TOF hit). The illustration of the drift velocity calibration principle is shown in figure 4.9. Then, drift velocity value can be estimated as:

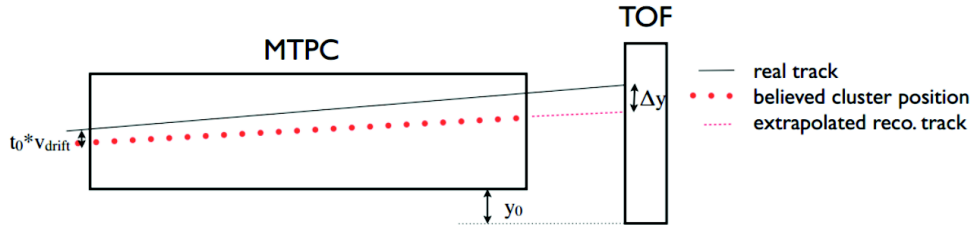


Figure 4.9: Illustration of drift velocity calibration procedure on TOF and one of the MTPCs example.

$$v_D = v_D^{DCS} (1 - \Delta y / y_\beta) \quad (4.2)$$

where  $v_D$  is the estimation of "true" drift velocity value,  $v_D^{DCS}$  is initial estimation measured with Detector Control System DCS.

As a starting point one always needs to use TOF to have a reference detector without drift velocity miscalibration. Calibration sequence which was used pre-

sented in 4.10. In this case everything is calibrated with respect to TOF-L (the

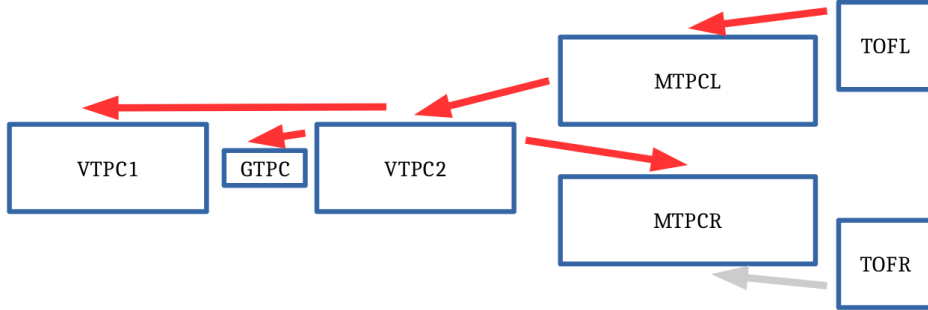


Figure 4.10: Illustration of drift velocity calibration sequence. With red arrows direction of calibration is shown, with grey arrow combination which was used only for cross-check.

magnetic field polarity for calibrated runs was such, that positively charged particles were deflected to the left). To verify results of the calibration procedure, this Stage 2 was performed one more time to assure that there is no slope anymore in  $\Delta y$  vs  $y$ . Plots for all TPCs and TOF combinations used for calibration are shown in the figure 4.11. The drift velocity resolution should be less than 1‰ to not provide any bias in track reconstruction procedure. The achieved resolution is usually even smaller than 1‰.

### 4.3.3 Chamber $T_0$ calibration (Stage 3)

This stage determines the  $T_0$ , i.e. the unknown but constant time offset of the delay of drift time sampling with respect to the timing reference of the event, the  $S_{1_1}$  signal. Traditionally,  $T_0$  is split according to the:

$$T_0 = T_0^{global} + T_0^{chamber} \quad (4.3)$$

where  $T_0^{global}$  is an overall delay, also slightly depending on the time-of-flight of the beam particle along with some of the cable delays common to all chambers.

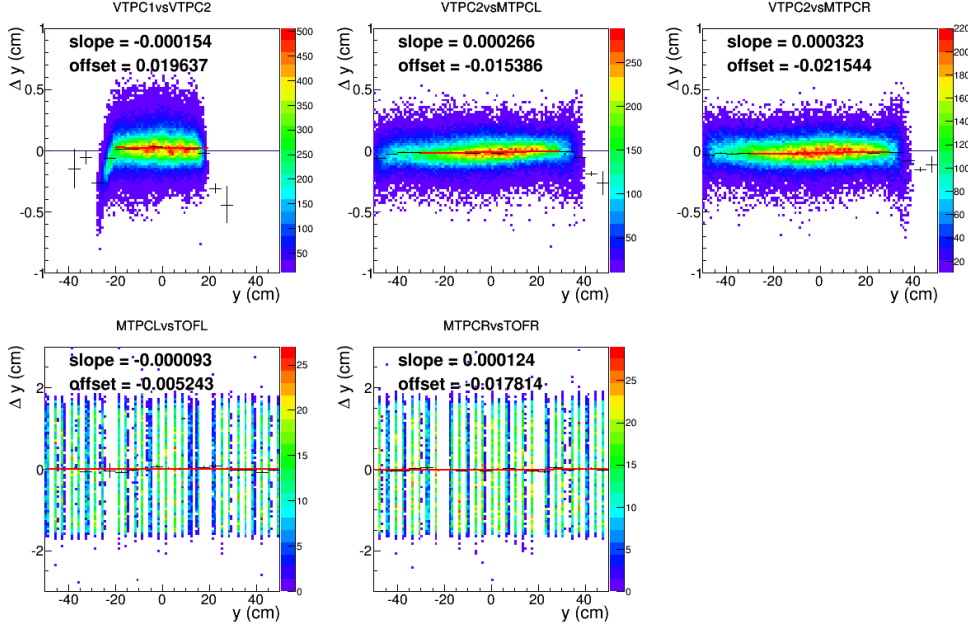


Figure 4.11:  $\Delta y$  vs  $y$  after drift velocity calibration. With the red line linear fit is shown with 2 parameters slope and offset.

By convention in the NA61/SHINE experiment,  $T_0^{VTPC1} = -94.6 \text{ ns}$  which determines  $T_0^{global}$  given from our  $T_0$  calibration procedure for VTPC1. The  $T_0^{chamber}$  for the other chambers are simply defined by their respective:

$$T_0^{chamber} = T_0 - T_0^{global} \quad (4.4)$$

The  $T_0$  is determined in the following way using the bottom point method:

$$(T_0 + t_{bottom})v_{drift} = L_{drift} \quad (4.5)$$

where  $L_{drift}$  is the drift length  $v_{drift}$  is the drift velocity  $t_{bottom}$  is the measured raw drift time to the bottom of the chamber.

Main-vertex tracks are dissected into local tracks which are refitted using their local clusters with the last cluster excluded from the fit. The intersection of the fitted local track and the pad plane of the last cluster determines the last point

of the track and the raw drift time corresponding to it determines  $t_{\text{bottom}}$  and thus  $T_0$  can be calculated. The procedure is illustrated in the figure 4.12. The

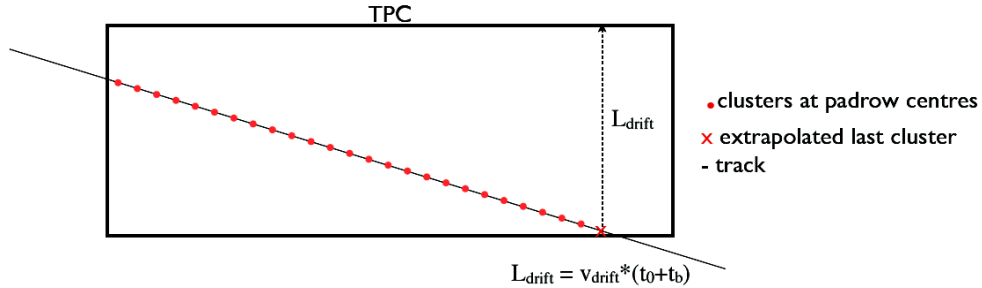


Figure 4.12: Illustration of the principle of the bottom point analysis for determination of the drift time measurement offset ( $T_0^{ch}$ ).

local track refitting with the last cluster excluded helps to reduce the effect of the bias due to the closeness of the cathode plane to the last detected bottom cluster along with the remaining discretization effect of the cluster centroid estimation.

#### 4.3.4 Chamber positions calibration (Stage 4)

It calibrates the geometrical vertical shifts  $y_0$  of TPC chambers. It is similar to Stage 2 but at this point drift velocity and  $T_0$  are known and one can calculate constant in time shift between any two chambers. The sequence of the calibration is the same as for Stage 2 - everything is calibrated relatively to TOF-L.

#### 4.3.5 Summary

Within this work the following parameters of the NA61/SHINE TPCs were calibrated: global and chamber  $T_0$ , Multihit time-to-digital converter calibration, drift velocity  $v_D$ , chamber positions in  $y$ -direction. The NA61/SHINE calibration software was improved (Stages 2 and 4) and successfully tested and applied on Pb+Pb collisions. The typical resolution for drift velocity calibration is less than 1‰ and TPC  $y$ -position resolution is at the order of 100  $\mu\text{m}$ . The cali-



bration results were submitted to NA61/SHINE DataBase and used for official productions.

## 4.4 Charged hadron identification

Charged hadron identification is a basic tool needed in any heavy-ion experiment. In this section the most common identification techniques will be discussed and a framework developed for CBM will be described. The purpose of this part of the work was to start the development of a PID framework, which could be easily maintained and extended with the new features in the future.

### 4.4.1 Identification with Time-of-Flight and specific energy loss

Charged hadron identification in most experiments is done with specific energy loss ( $dE/dx$ ) or Time-of-Flight (TOF) method (or combination of both). The specific energy loss method is based on the Bethe formula, which describes mean energy loss per distance traveled of charged particles depending on their mass, velocity and charge. The typical illustration of  $dE/dx$  measurement is shown in [4.13](#).

A Time-of-Flight measurement is based on relation between particle momentum, velocity and mass:

$$p = \frac{m\beta}{\sqrt{1 - \beta^2}} \quad (4.6)$$

One can measure particle momentum using the track curvature in the magnetic field and the velocity  $\beta = l/t$  measuring track length and time. An example of input information for particle identification with this method is shown in [4.14](#) based on a CBM simulation.

Both methods provide a clear separation between particle species. There are different methods to select particles samples with different efficiency and purity. One of them will be discussed in the next section.

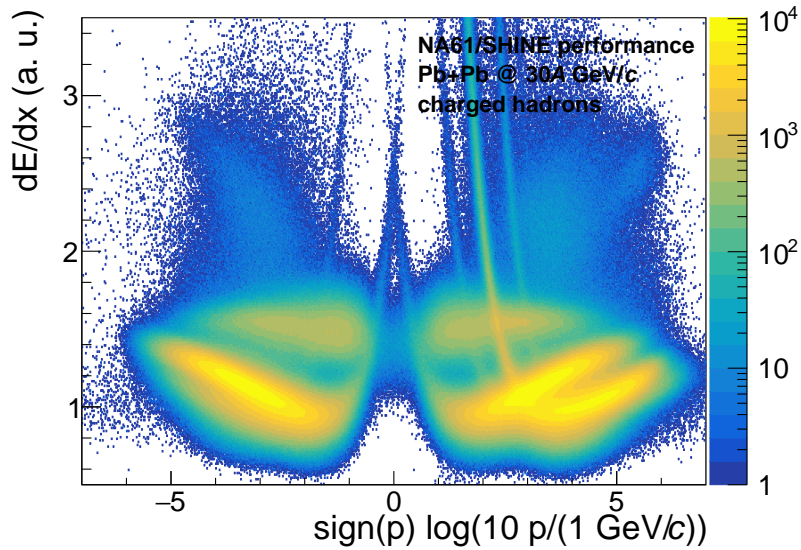


Figure 4.13: Specific energy loss  $dE/dx$  vs. momentum  $p$  for all charged tracks measured by the NA61/SHINE TPCs for Pb+Pb collisions at 30A GeV/c .

#### 4.4.2 Framework description

The framework functionality can be divided into two step:

1. two-dimensional histogram fitting
2. calculationg PID probabilities (hypotheses)

Both of them are described below.

##### Two-dimensional histogram fitting

Fitting of a two-dimensional (2D) histogram can be done as a sequence of fitting one-dimensional (1D) histogram in each bin along  $x$ -axis. Then the fit parameter dependence on the  $x$ -axis variable (usually momentum) can be approximated using the information from fits in all bins. Fitting of a 1D histogram is trivial using CERN ROOT [70] functionality. One has to define the fit function and initial values for the parameters and the build-in minimizator will find the best

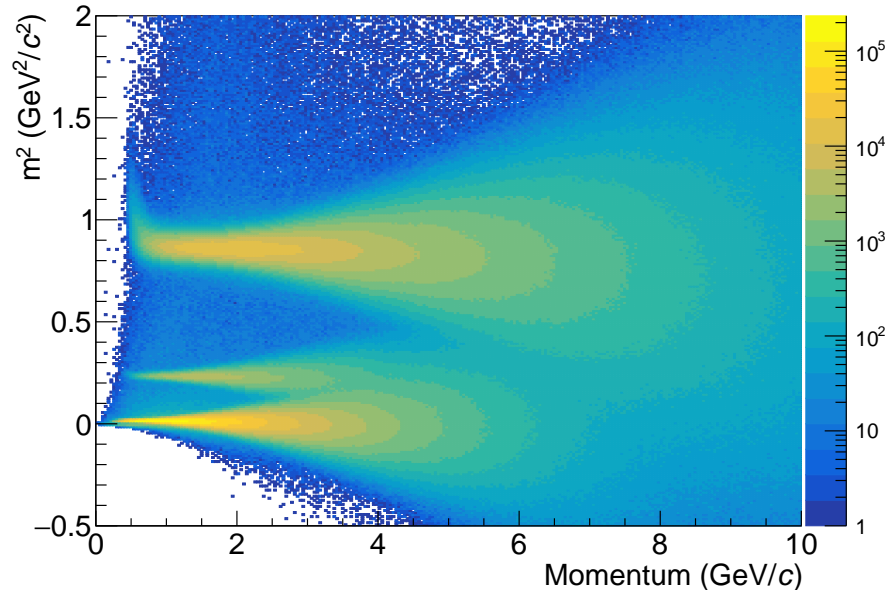


Figure 4.14: Mass square  $m^2$  of particle calculated using TOF information vs. momentum for simulated Au+Au collisions @ 10A GeV/c .

fit. The Framework provides an interface to tune the fitting procedure. For one-dimensional fitting one can modify:

- fitting function (usually, Gaussian)
- particles species to fit (protons, pions, kaons)
- fitting ranges for all particles species
- background function
- $\chi^2$  cut for the fit quality

The illustration of this procedure is shown in figure 4.15. As an input one bin from the mass square vs. momentum distribution obtained with CBM simulated data is used. The fit function is Gaussian for three particle species (protons, pions and kaons) and polynomial function with three parameters  $y = a_0 + a_1x + a_2x^2$  (pol2) for background (track and TOF hit mismatch). Parameter approximation is also

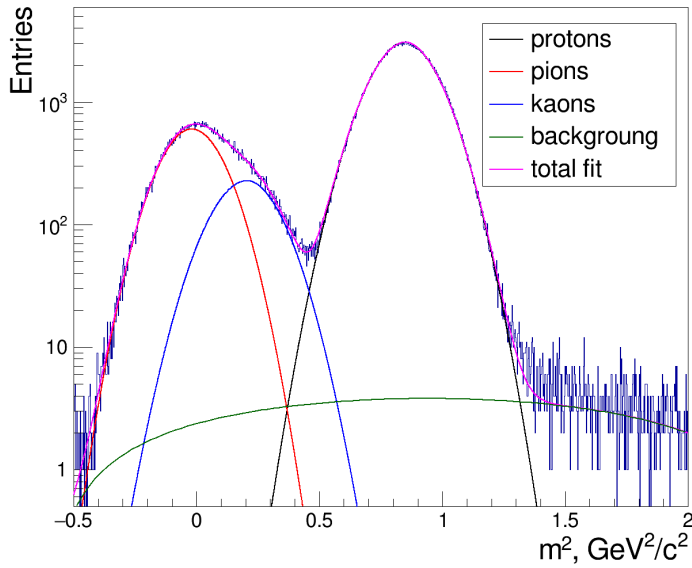


Figure 4.15: One dimensional fitting procedure illustration. The square mass is calculated using TOF and tracking information from CBM simulation. The particle species as well as the background and the total fit function are shown in different colors.

similar to that: one has to propagate the output (including uncertainties) from several one-dimensional fits to the ROOT minimizer. For approximation of parameters  $x$ -axis dependence one can set following options for every parameter independently:

- fitting function
- fitting range

This procedure is illustrated in figure 4.16. The one-dimensional fit was repeated for all momentum bins and approximated with polynomial functions with three parameters (pol2) for mean value  $\mu$  and standard deviation  $\sigma$ , polynomial functions with 5 parameters (pol4) for background parameters  $a_0, a_1, a_2$  and with exponential function for integral  $A$ .

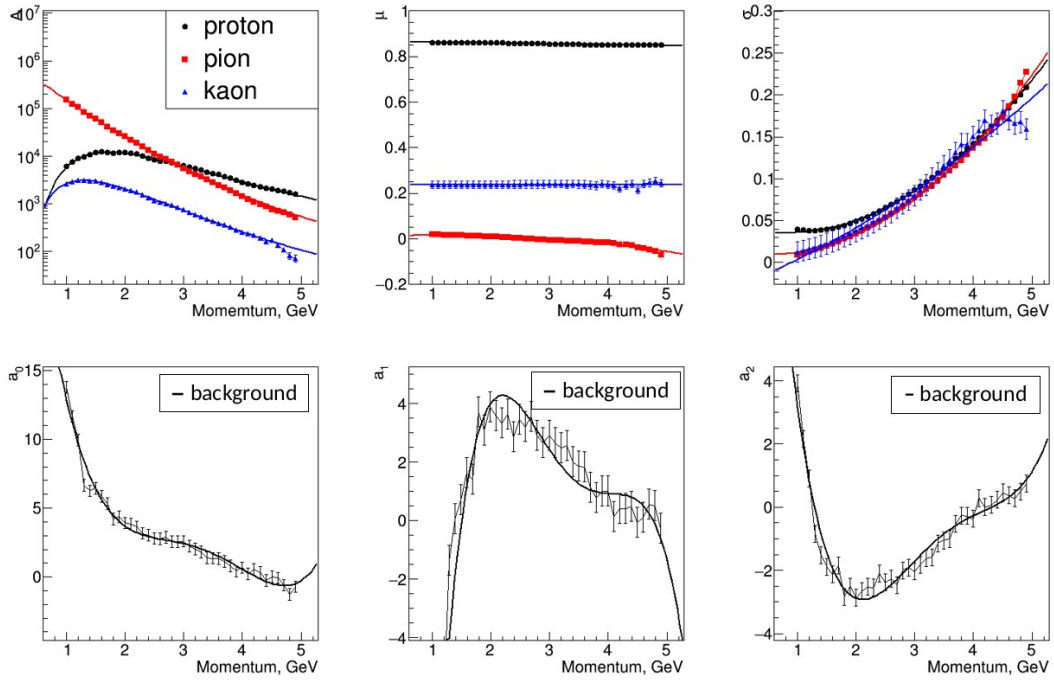


Figure 4.16: Illustration of fit parameters momentum dependence approximation procedure. For the top plots with different colors different particle species are indicated.

### Calculating probabilities

The next step after fitting 2D histogram is to use a parametrization to select particles of a given species. There are several ways to do so, the most popular of them are:

- sigma cut selection
- probability or purity selection

The second method is preferable, because it allows to control purity of the selected sample. In case of sensitive measurements of less abundant particles (kaons, in this example), the sigma cut could give a completely wrong measurement of the observable. In the Framework both of them are available with use of corresponding getters.

The selection criteria for purity selection is defined similar to that used in ALICE [71]. For example, for in selected case of particle identification with TOF, probability  $P_j$  for a given  $m^2$  and  $p$  for a particle to be of type  $j$  can be calculated as follows:

$$P_j(m^2, p) = \frac{G_j(m^2, p)}{\sum_{i=\pi, p, K} G_i(m^2, p) + BG(m^2, p)} \quad (4.7)$$

where  $G_j(m^2, p)$  is a fit function value at a given point for particle specie  $j$ ,  $BG(m^2, p)$  is a background fit function value.

Using this information the probabilities for all particle species can be calculated. The purity calculated for one momentum bin is shown in figure 4.17. Based on this information selection cuts can be defined.

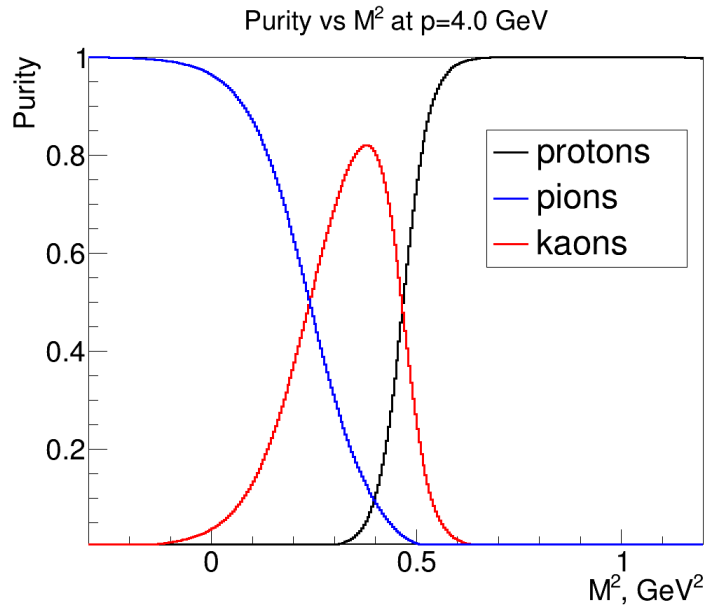


Figure 4.17: Purity of selection given particle specie (shown with different colors) for one momentum bin.

### 4.4.3 Results

An example of PID determination procedure using Gaussian fit function is presented in this section. In this section charged hadron identification for CBM simulation is performed using Time-of-Flight technique and for NA61/SHINE it is performed using specific energy loss. The results presented in this section are used for flow measurements, which are reported in section 5.

#### Time-of-Flight identification in CBM

To study the CBM performance for charged hadron identification, a purity cut of 90% was applied. The square mass vs. momentum distribution for selected particles is shown in figure 4.18. All three particle species (protons, pions and

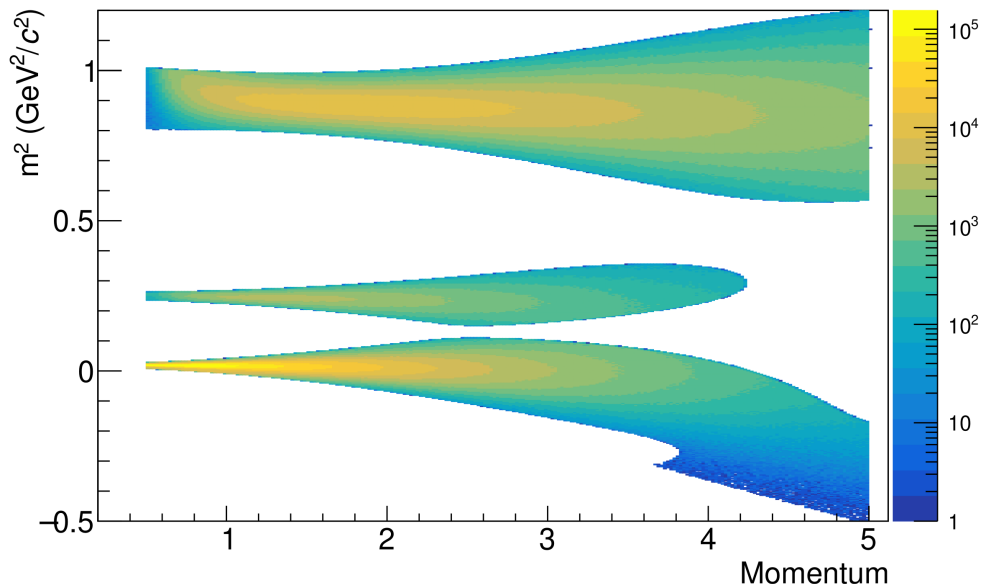


Figure 4.18: Mass square  $m^2$  vs. momentum for Au+Au @ 10A GeV/c after PID selection with purity cut of 90%.

kaons) have large selection area with a given purity.

The identified particle reconstruction efficiency, which takes into account tracking, track to TOF hit matching and identification efficiencies, is calculated as a



ratio of the number of reconstructed and identified tracks to the number of MC-particles of a given specie in a given kinematic bin. The efficiency map for protons is presented in the figure 4.19. A high identification efficiency over wide kinematic

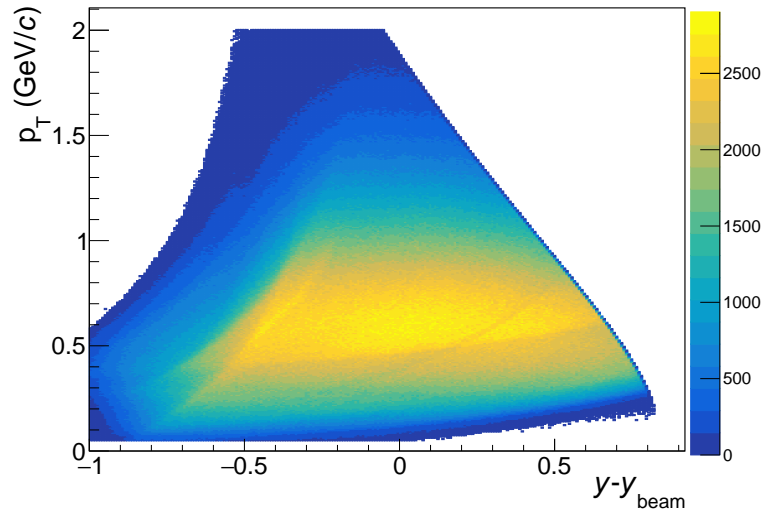


Figure 4.19: Transverse momentum  $p_T$  vs. rapidity  $y$  for protons after tracks and PID selection.

range is observed.

### Energy loss identification in NA61/SHINE

For charged hadrons identification in the NA61/SHINE experiment TShine software [72] was used. The package functionality includes fitting  $dE/dx$  distribution in momentum bins. Unlike to CBM analysis no approximating from bin to bin applied.

An example of the fitting procedure with TShine for one momentum bin is shown in figure 4.20. The fit function consists of a sum of four particle species: protons, pions, kaons and electrons. The description of the data is reasonably good near the centers of the peaks. The peaks shape is non-gaussian, therefore the tails of the distribution is not described by the fit.

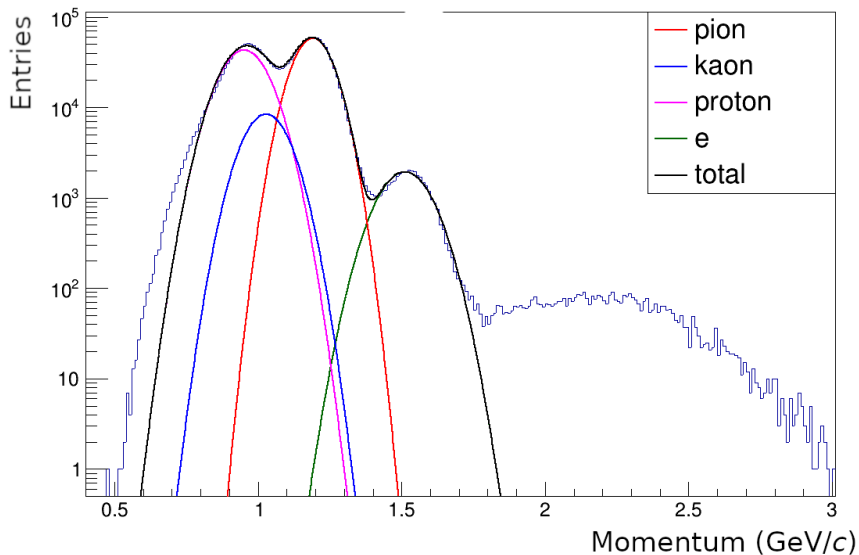


Figure 4.20: Transverse momentum vs. rapidity for protons after tracks and PID selection.

Using the fit results, identified particle samples with purity more than 90% are selected. Probabilities and purity criteria are calculated using the fit parameter in every momentum bin independently. The corresponding regions on  $dE/dx$  vs. momentum plot are illustrated in the figure 4.21. All particle species are clearly separated and the particle identification efficiency is large.

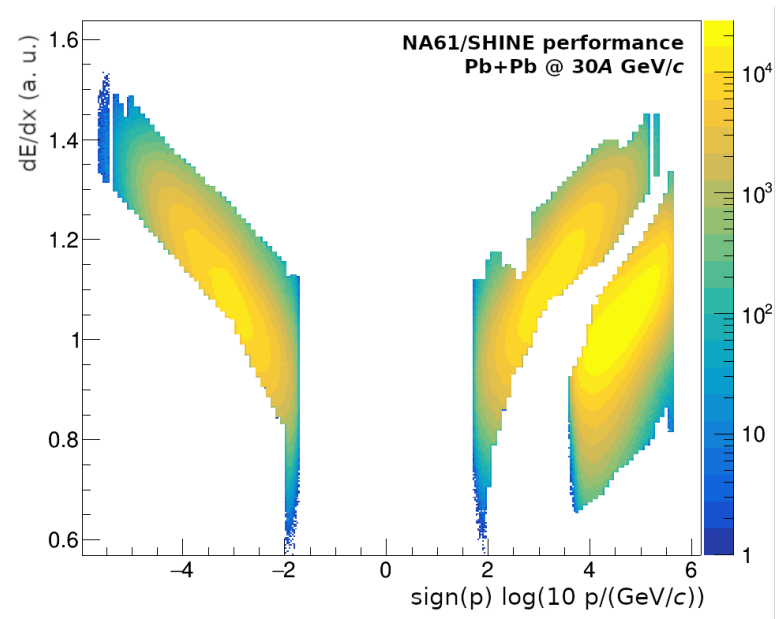


Figure 4.21: Specific energy loss  $dE/dx$  vs. momentum for pions and protons after tracks and PID selection.

The transverse momentum vs. rapidity distribution for selected negatively (left) and positively (right) charged pions with purity more than 90% are shown in figure 4.22. The same distribution for protons is shown in figure 4.23.

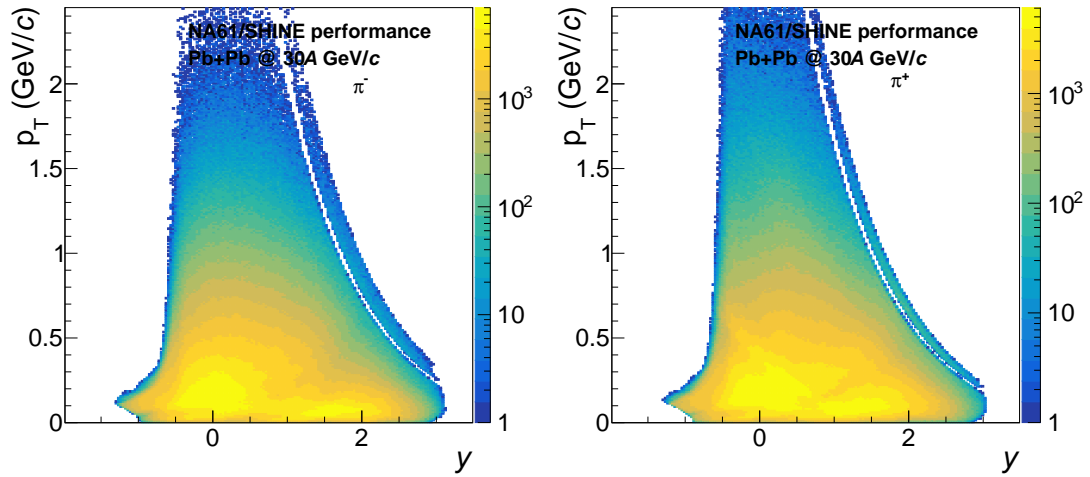


Figure 4.22: Transverse momentum vs. rapidity for negatively (left) and positively (right) charged pions after tracks and PID selection.

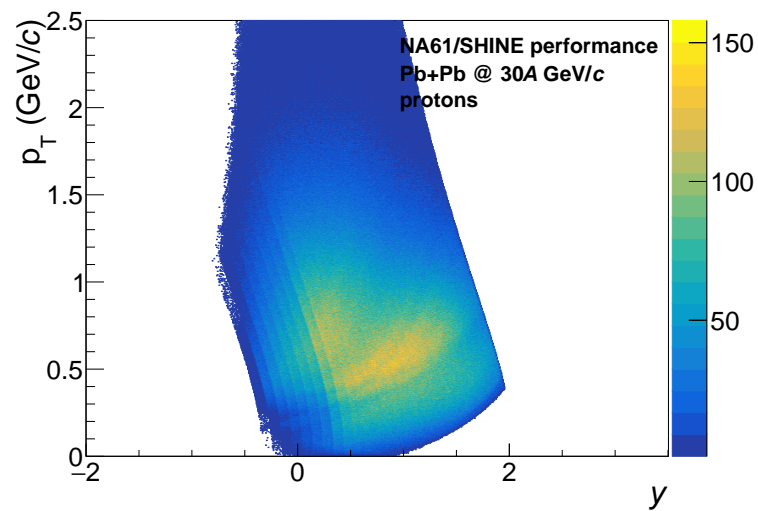


Figure 4.23: Transverse momentum  $p_T$  vs. rapidity  $y$  for protons after tracks and PID selection.

#### 4.4.4 Summary

An object oriented C++ Framework for particle identification analysis was developed [73]. The basic functionality is described above and includes:

1. Fill  $m^2$  vs  $p$  distribution for a pure sample of  $\pi$ , K and p (denoted below as 2D-( $\pi$ ,K,p)) and for all particles (2D-all). Pure sample of pions, kaons and protons can be obtained from decay daughters of  $K_s^0$ ,  $\Lambda$  and  $\phi$  using KF Particle Finder [74].
2. Parameterize  $m^2$  distribution in slices of momentum:
  - (a) Fit each slice of 2D-( $\pi$ ,K,p) using generalized Gaussian function  $G(m^2) = Ae^{-\left(\frac{|m^2-\mu|}{\sigma}\right)^k} \left(1 + \text{Erf}\left(s\frac{m^2-\mu}{\sqrt{2}\sigma}\right)\right)$  with 5 parameters abundance ( $A$ ), mean ( $\mu$ ), sigma ( $\sigma$ ),  $s$  and  $k$  are connected with skewness and kurtosis.
  - (b) Fit each slice of 2D-all with a sum of generalized Gaussian  $G(m^2, p)$  and polynomial function for background  $BG(m^2, p)$ .
3. Parametrize momentum dependence of the fit parameters. Repeat until parameters are stabilized.
4. Save fit parameters to the ROOT file for further use in the analysis.
5. Calculate a bayesian probability

This procedure can be applied in different centrality classes. In this case the 2D histogram for each centrality class should be fitted separately. More detailed information about C++ implementation with examples and HowTo can be found in the project documentation [75].

## 4.5 Centrality

The size and evolution of the medium created in a heavy-ion collision depends on collision geometry which is defined by the impact parameter vector, number of participants and binary collisions etc. Those geometric quantities cannot be measured directly. Experimentally, collisions are characterized by the measured particle multiplicities around midrapidity, or by the energy measured in the forward rapidity region, which is sensitive to the spectator fragments. For this, collisions are grouped into centrality classes with the most central class defined by events with the highest multiplicity (smallest forward energy) which corresponds to small values of the impact parameter. The most common definition of the centrality is connected to the impact parameter. According to it, collisions with the impact parameter  $b$  defined to have the following centrality  $c_b$ :

$$c_b = \frac{1}{\sigma_{inel}} \int_0^b P_{inel}(b) db \quad (4.8)$$

where  $P_{inel}(b) = d\sigma/db$  is the probability that an inelastic collision occurs at impact parameter  $b$ ,  $\sigma_{inel}$  - is the inelastic cross-section of a nucleus-nucleus collision. It is important to keep in mind, that the experimentally defined centrality is a different quantity and in general case does not correspond to  $c_b$ . In this section some methods to define centrality classes experimentally and their connection to model parameters will be discussed.

### 4.5.1 Mapping collision geometry to experimental observables

The main observables used for the centrality estimation in heavy-ion experiments are the charged particle multiplicity in a given kinematic window, and the forward (backward) rapidity energy, which is an approximation for number of projectile

(target) spectators. Then, the centrality definition reads as follows:

$$c_{N_{ch}} = \frac{1}{\sigma_{inel}} \int_{N_{ch}}^{\infty} \frac{d\sigma}{dN_{ch}} dN_{ch} \quad (4.9)$$

$$c_{E_{sp}} = \frac{1}{\sigma_{inel}} \int_0^{E_{sp}} \frac{d\sigma}{dE_{sp}} dE_{sp} \quad (4.10)$$

Usually the total inelastic cross-section is substituted with a total number of collisions corrected for a trigger inefficiency and bias. One way to do this correction will be described in the section 4.5.3.

The observables from equations 4.9 and 4.10 are not equivalent to equation 4.8. In case of a narrow correlation between impact parameter and measured observable they can be quite close. The illustration of this principle is shown in figure 4.24. In this case, the event classes selected by multiplicity can be mapped

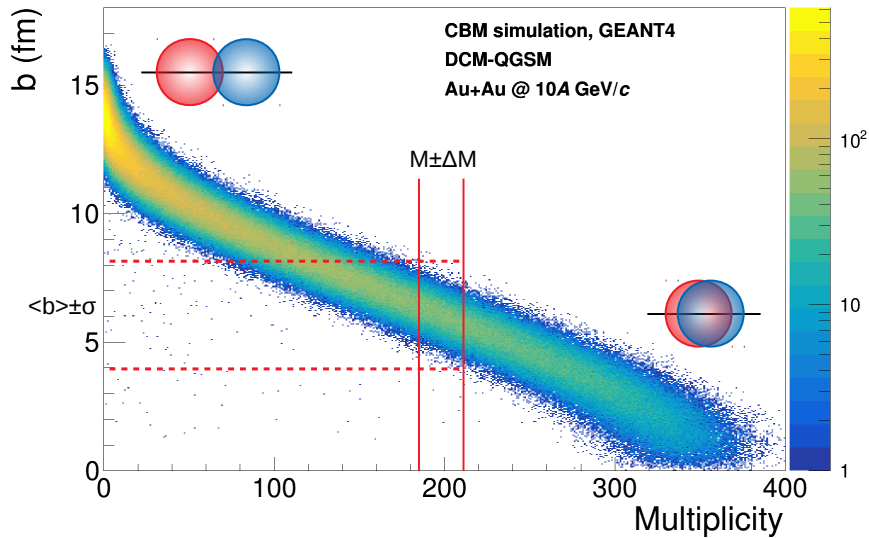


Figure 4.24: Correlation between track multiplicity measured by STS and impact parameter  $b$ .

to a certain range of impact parameter. It is done within some models which can reproduce measured quantities and has impact parameter. The most popular

model which is used for example by ALICE [76] and STAR [77] is the Glauber model.

### 4.5.2 Glauber model

The Glauber model is widely used to describe the initial state distribution of nucleons in heavy-ion collisions. In this model, a collision is described as individual interactions of the constituent nucleons. It assumes, that with sufficiently high energy, nucleons pass each other undeflected and move independently inside the nucleus. Interactions are defined by the size of the nucleons, which is large compared to the range of the nucleon-nucleon force. An input of the Glauber model is the nucleon density inside the nucleus. It is usually parametrized by Fermi distribution.

$$\rho(r) = \rho_0 \frac{1 + w(r/R)}{1 + \exp(\frac{r-R}{a})} \quad (4.11)$$

where  $R$  is radius of the nucleus,  $\rho_0$  is density in the center of the nucleus,  $a$  is parameter which defines size width of the crust.

Due to its simplicity and good description of experimental data, the Glauber model is widely used for centrality definition. Often it is the only way to make comparison of experimental data measured with different detectors and with different centrality definitions. The way to do this is described below.

### 4.5.3 MC-Glauber fit

To estimate the total cross-section and the trigger bias it is common to use the so-called MC-Glauber fit. The procedure includes fitting experimentally measured particle multiplicity (or similar observable, for example number of hits in some detector, etc) with a Glauber model based function.

$$F_{fit}(f, \mu, \sigma) = P_{\mu, \sigma} N_A(f) \quad (4.12)$$



where  $P_{\mu,\sigma}$  is the negative binomial distribution,  $N_A$  is a number of ancestors, which can be parametrized in a following way (some selected parametrization, but not a full list):

$$\begin{aligned} N_A(f) &= fN_{part} + (1 - f)N_{coll} \\ N_A(f) &= N_{part}^f \\ N_A(f) &= N_{coll}^f \end{aligned} \tag{4.13}$$

where  $N_{part}$  and  $N_{coll}$  is the number of participants and number of binary collisions. The first term corresponds to the contributions from soft processes and the second corresponds to hard processes. For FAIR energies, the second term is expected to be small. The most challenging part in this procedure is to find the best fit. One possible implementation is described in the next section.

At some point, the contributions from the trigger and from the electromagnetic interactions bias the measured distribution. At this point, the data and the fit start to diverge. Below this point, which is called the "anchor" point, the centrality determination is not reliable. With the MC-Glauber fit one has the connection between measured collisions and simulated collisions with the Glauber model. With the assumption, that the Glauber model is describing the data, one can calculate average values of the model parameters such as impact parameter,  $N_{part}$  and  $N_{coll}$  for a given centrality class.

#### 4.5.4 Framework description

The first step towards centrality estimation is to determine the total cross-section. As discussed above, it can be done with the MC-Glauber fitting procedure. It involves finding the best fit in a phase space of three parameters of the function from equation 4.12  $f, \mu, \sigma$ . The first parameter defines the fit function shape and can be connected with the type of nucleon-nucleon interaction. The last two ( $\mu$  and  $\sigma$ ) are parameters of the NBD distribution. The parameter  $\mu$  is the

mean number of tracks (hits) in the detector produced from the one source (ancestor). It convolutes particle production from physics processes and detector acceptance/efficiency. The fit function is very sensitive to changes of this parameter due to the fact that it effectively changes the scale on the  $x$ -axis. The second parameter of the NBD distribution  $\sigma$  defines the spread in multiplicities (number of hits) for a given  $N_A$  and can be connected to fluctuations of some kind. To find the best fit one should first to define a criteria for comparing. One of the most popular fitting criteria is  $\chi^2$ , which is defined as follows:

$$\chi^2 = \sum_{i=i_{low}}^{i_{high}} \frac{(F_{fit}^i - F_{data}^i)^2}{(\Delta F_{fit}^i)^2 + (\Delta F_{data}^i)^2} \quad (4.14)$$

where  $F_{fit}^i$  and  $F_{data}^i$  are values of the fit function and the fitted histogram at bin  $i$ ,  $\Delta F_{fit}^i$  and  $\Delta F_{data}^i$  are corresponding uncertainties,  $i_{low}$  and  $i_{high}$  are higher and lower fitting ranges. To make the value of  $\chi^2$  more illustrative it is divided over number of fitted bins:

$$\chi_{norm}^2 = \frac{\chi^2}{i_{high} - i_{low}} \quad (4.15)$$

In this case the  $\chi_{norm}^2$  value is close to one, which means that on average distance between fit function and data histogram is consistent within the uncertainties, which can be interpreted as a very good fit quality. The fitting procedure takes as an input:

1. a root file with the MC-Glauber model parameters generated using TGlauberMC [78];
2. input histogram to fit;
3.  $N_A$  parametrization, for example one of the presented in Eq. 4.13;
4. parameters range ( $f$  and  $\sigma$ , fitting of  $\mu$  parameter will be described later) and number of steps to search for the minimum;

## 5. fitting range;

For each step of  $f$  and  $\sigma$  parameters the optimal value of the  $\mu$  parameter is calculated. As was mentioned before the  $\chi^2$  is very sensitive to the change of this parameter and the fit converges very fast. It is implemented with the golden-section search method. Then iterating over all  $f$  and  $\sigma$ , the optimal fit parameters are found. After finding the optimal fit parameters one can easily estimate the total cross-section. With a known cross-section all events can be divided into groups with a given range of total cross-section (0-5%, 10-20% etc). For that one defines an observable sensitive to the collision geometry (number of track for example in figure 4.24) and use it for event selection. For an one-dimensional histogram it is done simply by calculating the number of events in bins (with linear approximation between the bins) and putting an event class border if this number exceeds some value. The similar approach can be also used in case of a more complicated selection, for example in case of using correlation between two different observables, for example track multiplicity and energy measured by a forward rapidity calorimeter, as shown in figure 4.25. The event-by-event centrality is determined by the following procedure:

1. STS multiplicity ( $M_{\text{STS}}$ ) and energy deposition in PSD subgroup ( $E_{\text{PSD}}$ ) scaled by their maximal value ( $M_{\text{STS}}^{\text{max}}$  and  $E_{\text{PSD}}^{\text{max}}$ ).
2. Parameterise 2D correlation between multiplicity and/or PSD subgroup energies:
  - initial fit of profile (red circles) of the correlation using a polynomial function (red line);
  - recalculate profile (black triangles) according to the fit slope and refit (red line).
3. Slice 2D correlation perpendicular to the fit (Fig. 4.25) or 1D distribution (not shown) in percentiles of total number of events.

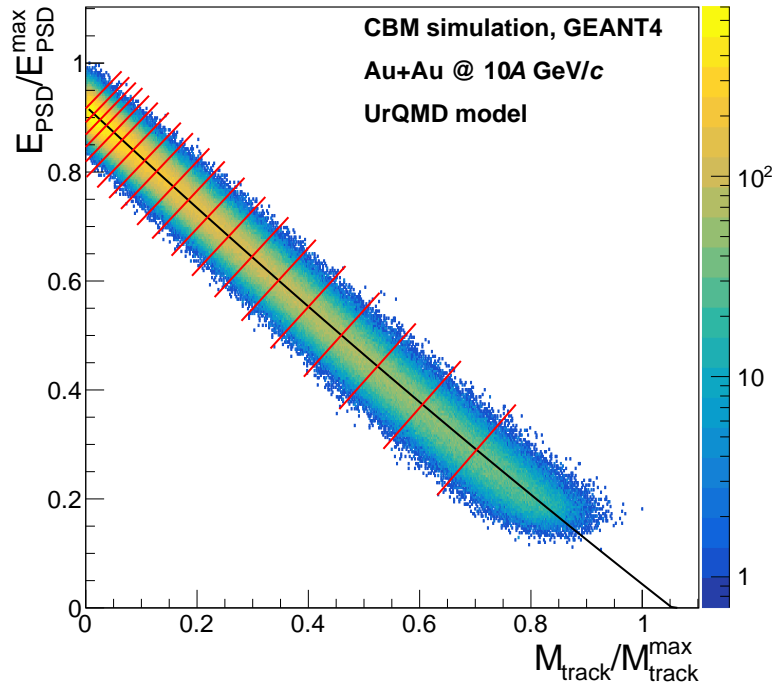


Figure 4.25: Illustration of the 2D centrality determination procedure. The centrality is defined by the correlation between track multiplicity measured by STS+MVD and forward rapidity energy measured by PSD. The correlation is overlaid with a fit function and centrality classes borders.

For each centrality class the mean value of the impact parameter and its corresponding standard deviation was found using simulated information.

### 4.5.5 Results

In the following section the results obtained with the framework will be discussed. There are two experiments where it was used: CBM and NA61/SHINE. The results are subdivided into corresponding subsections and used for flow measurements which will be discussed later.

## CBM

**PSD hole size effects** To reduce the radiation damage by the high-intensity beam, the PSD geometry includes a diamond shaped hole of size 20 x 20 cm in the middle for the beam pipe. In this section, the effect on the centrality determination performance is discussed, and compared to a previous study as described in the PSD TDR [62]. To study the impact on the centrality determination, three PSD geometries with hole sizes 0, 7 and 20 cm were implemented. The full CBM detector response was simulated with GEANT4. As event generator the DCM-QGSM-SMM model was used.

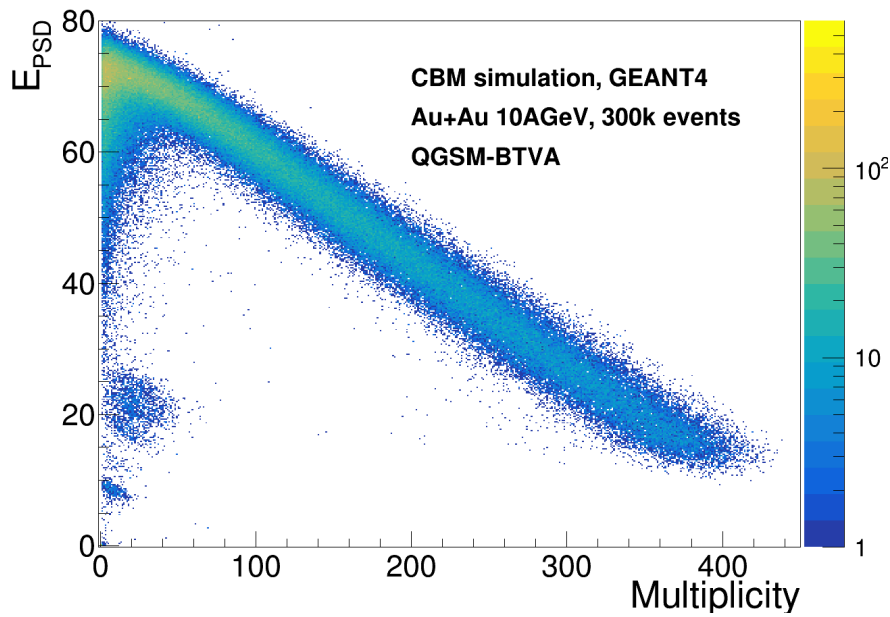


Figure 4.26: PSD energy distribution vs. STS multiplicity for realistic GEANT4 simulation with PSD geometry without a hole.

The forward energy with the track multiplicity correlation for the simulation without a hole is shown in figure 4.26. As expected, a strong anti-correlation is observed – the PSD energy is an approximation for the number of projectile spectators, and the number of charged particles is roughly proportional to number of

participating nucleons. In this case, both observables can be used as independent centrality estimators. They have different sensitivities to the impact parameter and the first study of the PSD performance done for the TDR shows that the PSD resolution is slightly worse comparing to the STS.

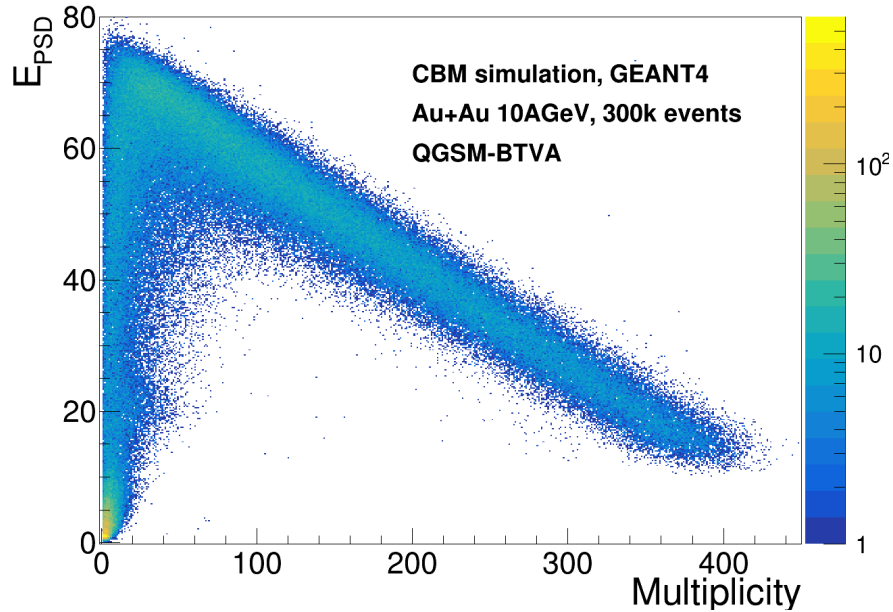


Figure 4.27: PSD energy distribution vs. STS multiplicity for realistic GEANT4 simulation with PSD geometry with 7 cm hole (diamond shape).

The forward energy with the track multiplicity correlation for the simulation with a 7 cm hole is shown in figure 4.27. This setup is close to one which was studied for the PSD TDR [62]. A large energy loss due to fragments passing through the hole is observed mostly for very peripheral events. In central and mid-central collisions the PSD still can be used as independent centrality estimator. Unbiased by the hole are about 30% of the collisions.

The forward energy with the track multiplicity correlation for the simulation with a 20 cm hole is shown in figure 4.28. This hole size is necessary due to the radiation damage of the PSD by the beam halo and by heavy fragments hitting the PSD producing hadronic showers.

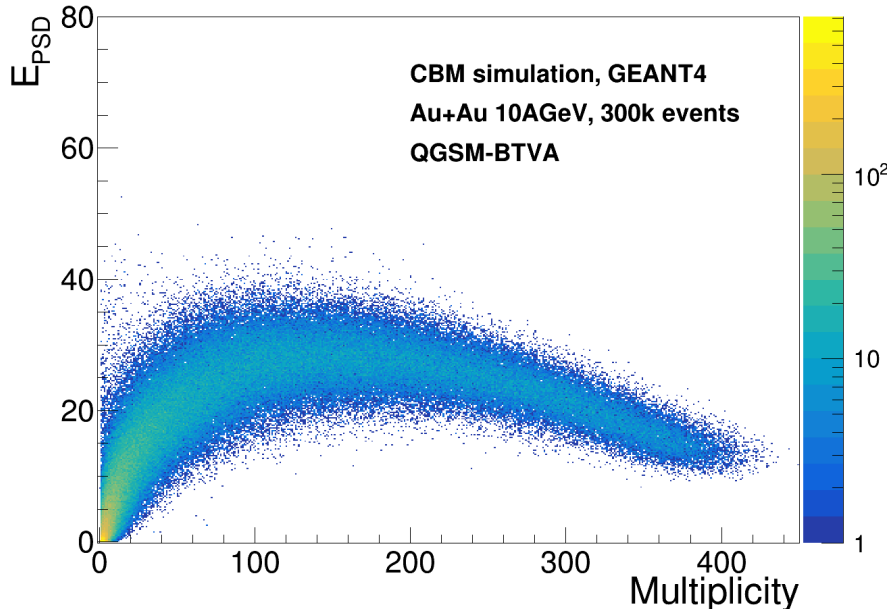


Figure 4.28: PSD energy distribution vs. STS multiplicity for realistic GEANT4 simulation with PSD geometry with 20 cm hole (diamond shape).

The correlation is completely degraded in this case due to the large hole. In this setup, an additional detector is needed to estimate the centrality together with the PSD. There is an ongoing discussion to add a quartz counter in the hole to register number and charge of particles passing through. Additional studies with a combination of other detectors are needed to study the centrality estimation performance.

**Centrality estimation resolution** In this section the simulation dataset with the UrQMD model and a 20 x 20 cm hole is used. An illustration of the MC-Glauber fitting procedure using the CBM simulation is presented in figure 4.29. The fit is describing the multiplicity distribution over the whole range. No event selection or other biases are observed.

The fit results were used to calculate the impact parameter distribution in each centrality class. The result is shown in figure 4.30 (left). Also the mean value

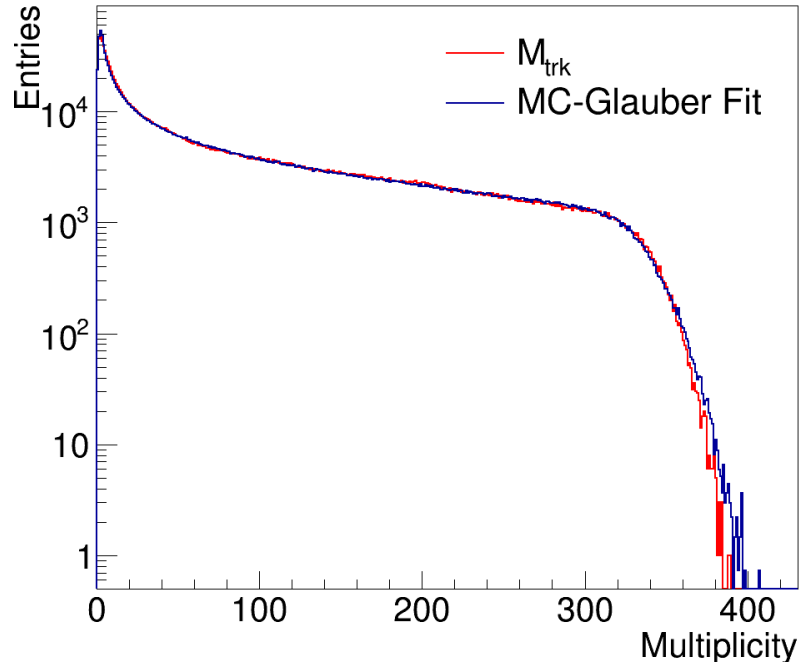


Figure 4.29: Track multiplicity distribution (red) and MC-Glauber fit (blue).

and the width of the impact parameter were calculated for a given centrality, the result is presented in figure 4.30 (right). For more peripheral events the centrality classes start to overlap. For a further analysis one can make the bin size in centrality larger.

As a final result, the centrality classes are defined using the energy deposited in the PSD. Borders of the centrality classes as well as the PSD energy distribution are presented in figure 4.31. The size of the bin size is 5% and only first 60% of centrality is shown.



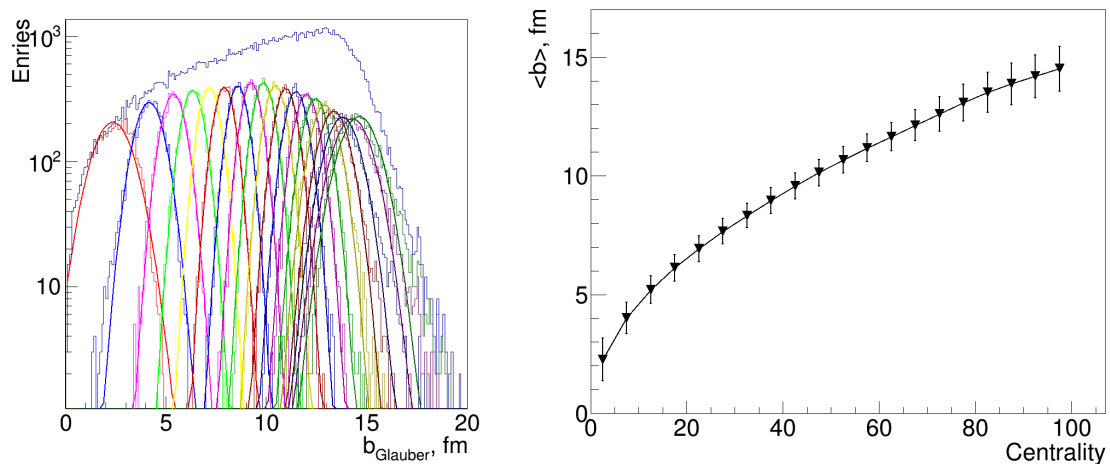


Figure 4.30: Impact parameter distribution for each centrality classes indicated with different colors (left). Mean impact parameter in each centrality class vs. centrality (right).

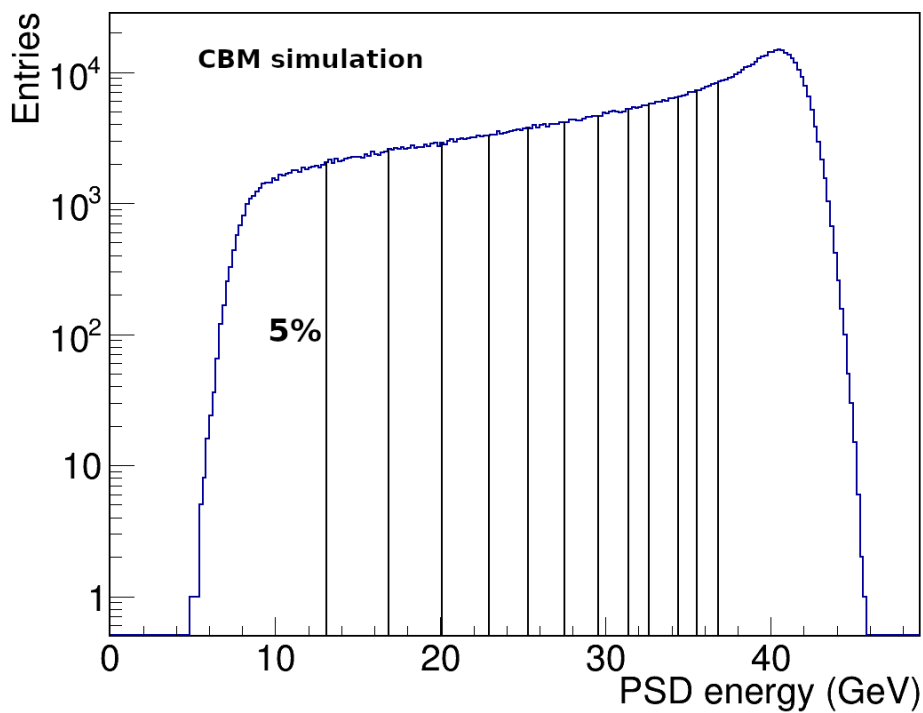


Figure 4.31: PSD energy distribution for the CBM simulation. Dashed vertical lines mark the borders of event (centrality) classes.

## NA61/SHINE

The Centrality framework was also tested with NA61/SHINE Pb+Pb data @ 30A GeV/c collected in 2016. The result of the MC-Glauber fitting procedure shown in figure 4.32. The trigger bias for this dataset is expected to be less than

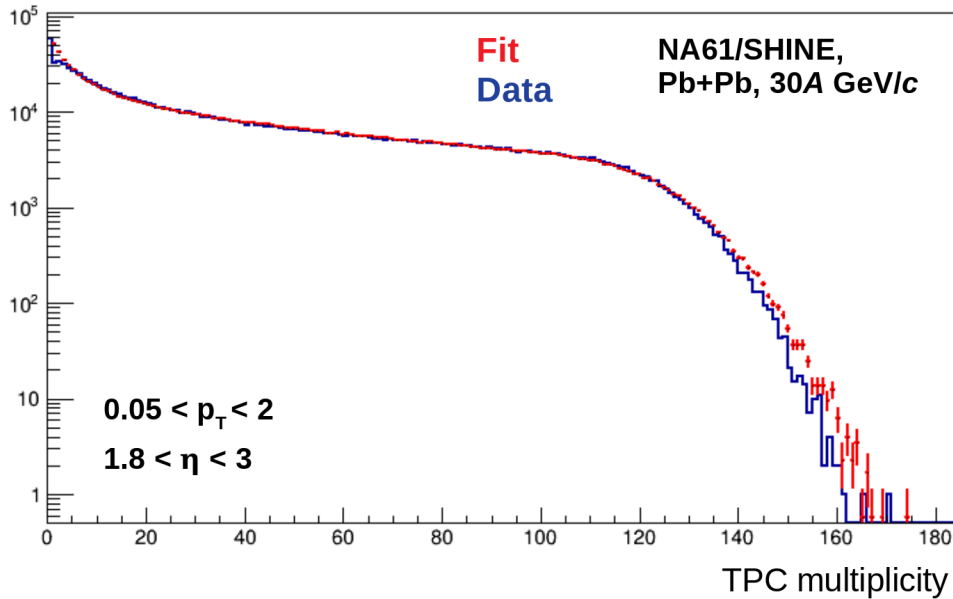


Figure 4.32: Track multiplicity distribution (red) and MC-Glauber fit (blue).

5%.

As well as for the CBM experiment, the PSD energy deposition is used for centrality determination. The centrality classes are presented in figure 4.33. Both central and minimum bias triggers are used for analysis. The central trigger found to be unbiased for 0-15% of centrality.

### 4.5.6 Summary

An objected oriented C++ framework for centrality analysis was developed. The basic functionality is described above and includes:

- Estimate trigger / event reconstruction / etc biases using MC-Glauber fit

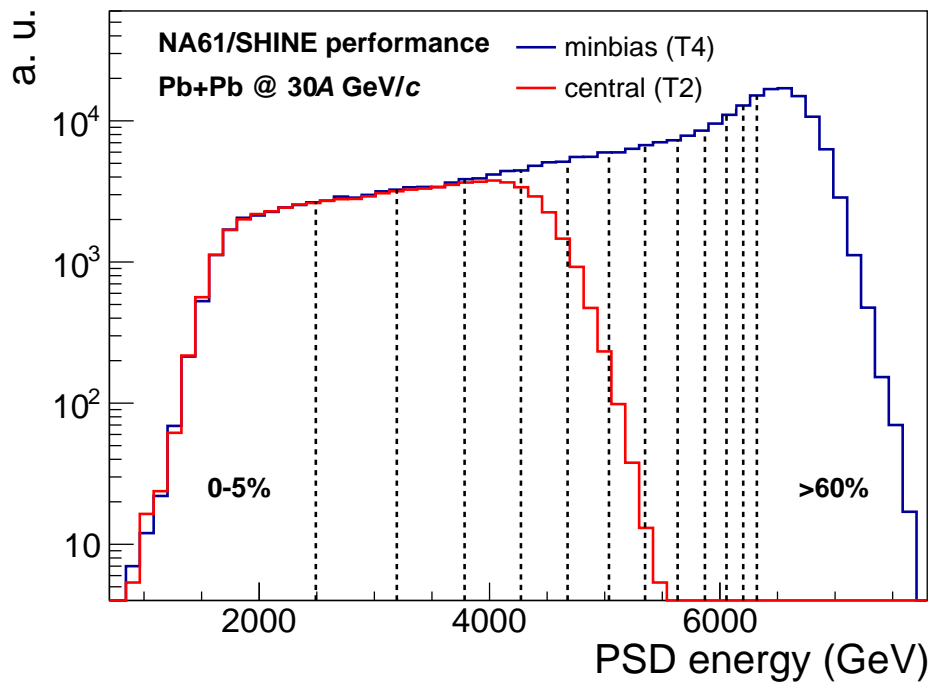


Figure 4.33: PSD energy distribution for central (T2) and minimum bias (T4) triggers. Dashed vertical lines mark the borders of event (centrality) classes.

- Divide events into classes based on any observable or correlation of two observables
- Map event classes to geometrical model parameters
- Store information into output object
- Getting centrality class for a given value of observable

It was tested using CBM simulation results and NA61/SHINE data. The framework is (well) documented and a modular code structure allows for a future extensions. It is included in CBMROOT as external package and can be used independently as a standalone framework [79]. More detailed information about the C++ implementation with examples and HowTo can be found in project documentation [80].



# Chapter 5

## Results

In this section the flow results for the CBM performance and the NA61/SHINE data are presented. The measurement technique was discussed in the section [2.3](#).

### 5.1 NA61/SHINE measurement

The results are presented for correlations between charged pions and protons produced by strong interaction processes and their weak and electromagnetic decays (in the TPC acceptance [\[81\]](#)) and all hadrons at forward rapidity (in the PSD acceptance [\[82\]](#)). The results are corrected for detector non-uniformity. No corrections for secondary interactions were applied.

#### 5.1.1 Correction for detector effects

The results are corrected for tracking efficiency using GEANT4 [\[67, 66\]](#) Monte-Carlo simulation. Event generator DCM-QGSM with coalescence afterburner was used. It is briefly described in Section [4.1.1](#). The correction was implemented as a weight for every particle equal to inverted tracking efficiency for a given particle specie in a given kinematic bin. The tracking efficiency map for positively charged pions depending on transverse momentum and rapidity is shown

in figure 5.1. It is defined as a ratio of the number of reconstructed tracks with a matched MC-particle to the number of MC-particle in a given kinematic bin. For a wide acceptance range acceptance is flat and in the order of 60% due to

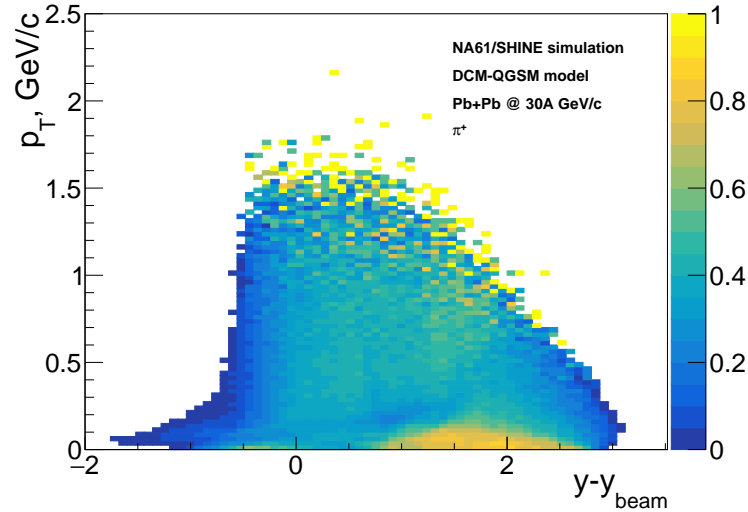


Figure 5.1: Tracking efficiency map for positively charged pions.

limited acceptance of NA61/SHINE detector in  $\varphi$  (Vertex TPCs consist of two parts separated in x-direction, which leads to a "hole" in the acceptance). For low transverse momentum and forward rapidity tracks the efficiency is close to one, which can be explained by magnetic field bending tracks away from the "hole".

The efficiency for protons is defined in the same way and is presented in figure 5.2. The same pattern for efficiency dependence on rapidity and transverse momentum as for pions is observed. Also the results are corrected for particle identification efficiency. Each particle is weighted with inverted efficiency of a given particle specie selection in the specific momentum bin.

### 5.1.2 Systematics

For each particle track  $i$  reconstructed with the TPC a  $n$ -th harmonic unit vector  $\mathbf{u}_{n,i}$  is defined. The  $\mathbf{q}_n$ -vectors were calculated for charged pions and protons in

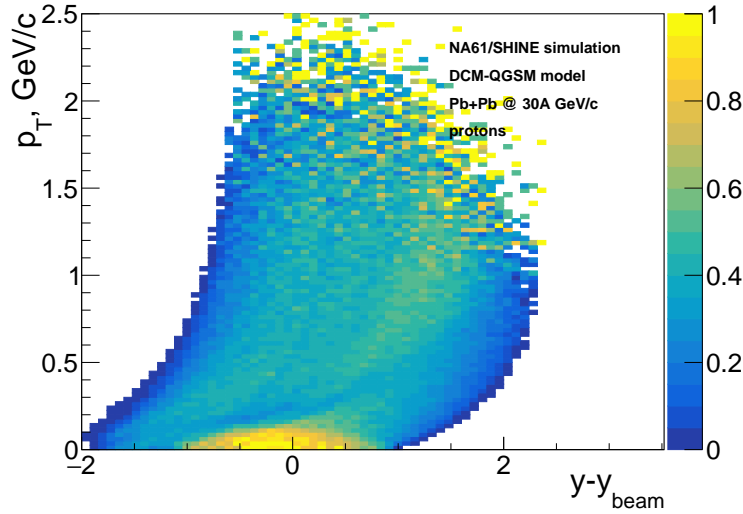


Figure 5.2: Tracking efficiency map for protons.

transverse momentum ( $p_T$ ) intervals using equation 2.4 where  $M$  is the number of particles in a given  $p_T$  interval.

For the analysis PSD modules were subdivided into 3 groups (PSD1, PSD2, PSD3) with approximate coverage in pseudorapidity  $\eta \in \{(5.1, \infty), (4.4, 5.1), (4.0, 4.4)\}$ . Flow coefficients can be calculated using any of those 3 subevents for event plane estimation. Ideally they should provide independent measurement with different event plane estimations. For the case of PSD subevents difference in acceptance is not expected to have a significant impact on flow measurement. Flow coefficients were calculated using all 3 subevents, and the comparison for negatively charged pions vs transverse momentum is shown in figure 5.4. All 3 subevents show consistent results. The uncertainty of PSD3 the measurement is higher, which is explained by a smaller number of particles hitting the outer part of the detector. For the following results the combined flow for all subevents will be presented. The combination was done by arithmetic mean calculation and corresponding error propagation.

As was described in section 2, another way to check the consistency of the

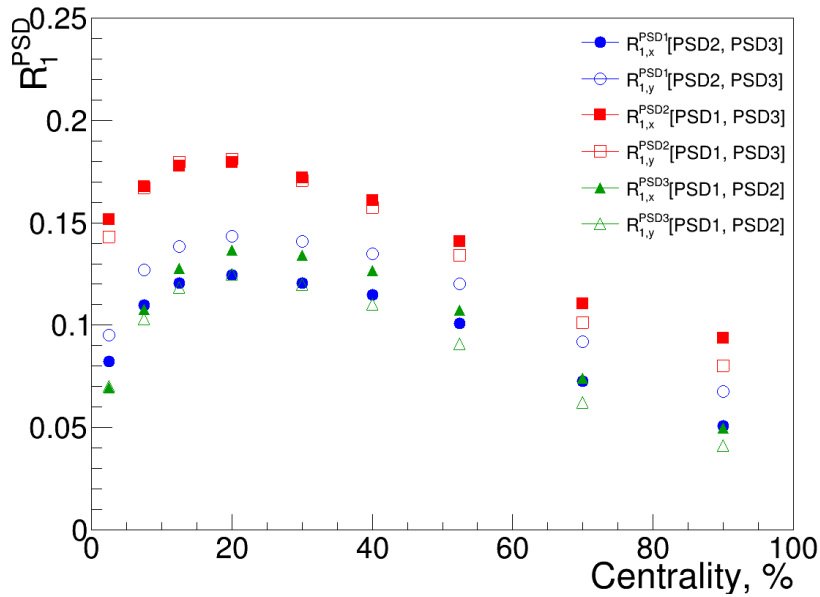


Figure 5.3: The first harmonic resolution correction factor calculated with the 3-subevent method.

results and eliminate possible systematic biases is comparing  $x$  and  $y$  components of the flow coefficients. Both components of the directed flow for negatively charged pions vs. transverse momentum are shown in figure 5.5.

The results of the  $x$  and  $y$  components are very similar, but with very different uncertainties, which are significantly larger for the  $y$ -component. That is connected to the non-uniform TPC acceptance in  $\phi$  – there are almost no tracks in the vertical ”hole” between two parts of Vertex TPCs. For the following results on the directed flow only the  $x$ -component is presented. Results for  $v_1$  and  $v_2$  with different PSD subevents and different  $x$  and  $y$  components are found to be consistent within statistical uncertainties.

### 5.1.3 Results for directed flow

The presented preliminary data are for all PSD subevents combined. For  $v_1$  only the  $x$ -component correlation is used. Figure 5.6 (*left*) shows the directed flow



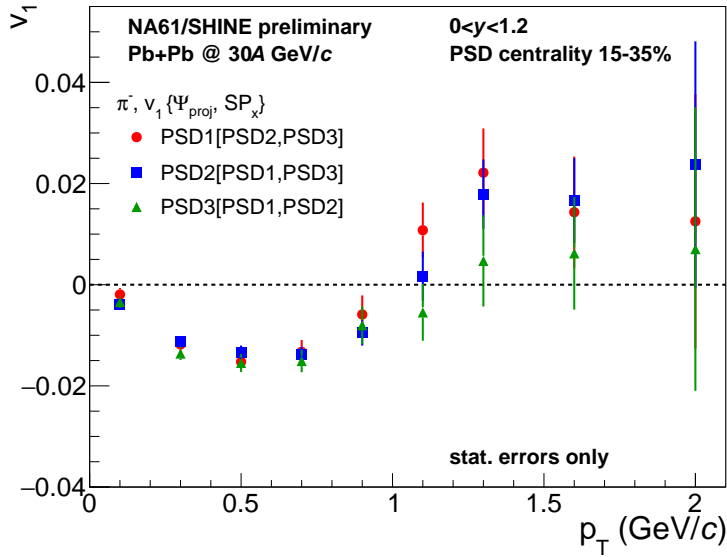


Figure 5.4: Negatively charged pion directed flow for different event plane estimators in PSD centrality class 15-35%. Only statistical uncertainties are shown.

of negatively charged pions as a function of transverse momentum in different centrality classes (0-15%, 15-35%, 35-60%). A strong centrality dependence of  $v_1$  is observed. At  $p_T \approx 0$  directed flow approaches 0 and changes sign depending on centrality in the region  $p_T \approx 0.9-1.3$  GeV/c .

Figure 5.7 (right) shows the  $\pi^-$  directed flow as a function of  $p_T$ . It is compared to the new analysis [83] of NA49 data for Pb+Pb collisions at 40A GeV using forward calorimeters (VCal and RCal) for projectile spectator plane estimation. Agreement between NA61/SHINE and NA49 measurements within statistical errors is observed.

Positively and negatively charged pions and proton directed flow as a function of transverse momentum for 15-35% centrality class is shown in figure 5.8.

A significant mass dependence of the directed flow is observed. The charge dependence of pion  $v_1$  can be sensitive to effects of the magnetic field in heavy-ion collisions [84].

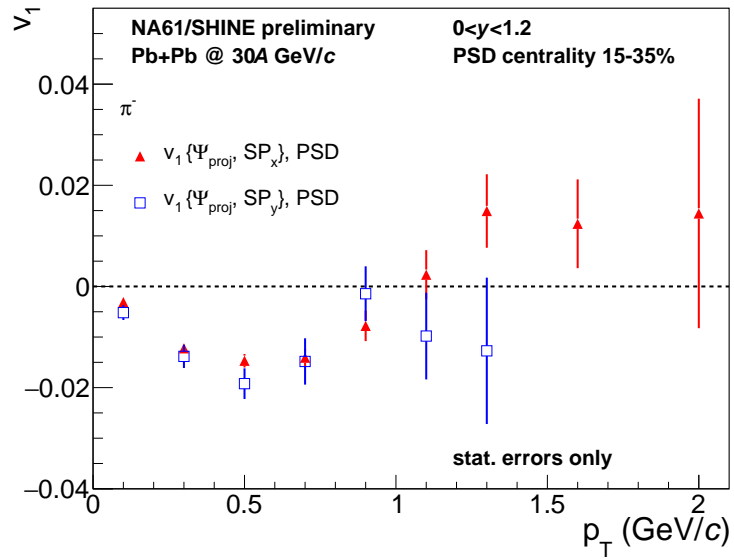


Figure 5.5: Negatively charged pion directed flow for  $x$  and  $y$  components in PSD centrality class 15-35%. Only statistical uncertainties are shown.

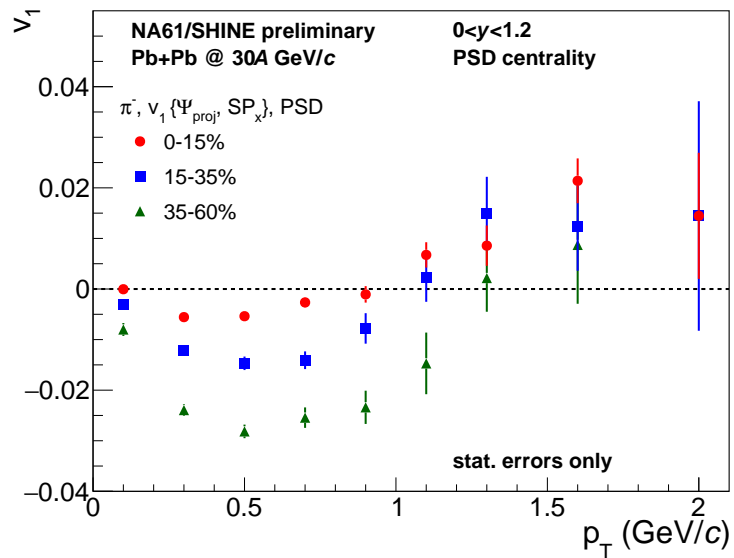


Figure 5.6: Negatively charged pion directed flow vs. transverse momentum  $p_T$  for different centrality classes. Only statistical uncertainties are shown.

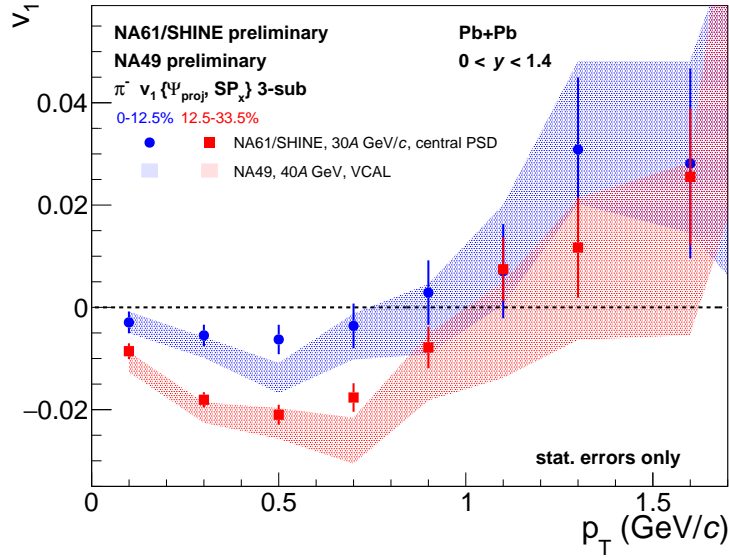


Figure 5.7: Negatively charged pion directed flow compared to a new analysis [83] of the NA49 Pb+Pb data at 40A GeV . The NA61/SHINE results are obtained using central PSD modules for centrality and projectile spectator plane ( $\Psi_{proj}$ ) estimation. Only statistical uncertainties are shown.

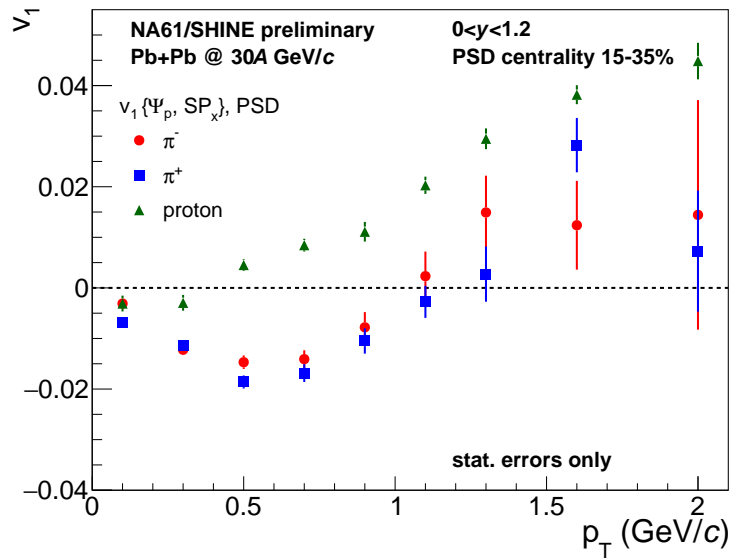


Figure 5.8: Charged pion and proton directed flow as a function of transverse momentum for 15-35% PSD centrality class. Only statistical uncertainties are shown.

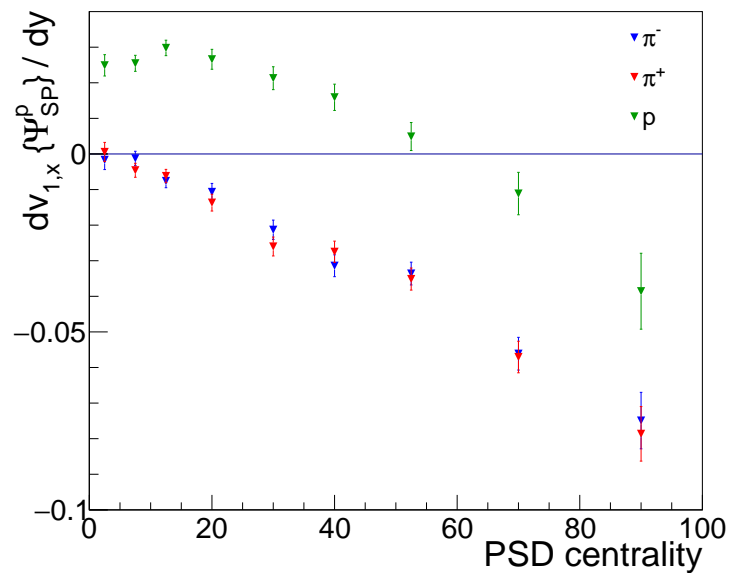


Figure 5.9: Slope of directed flow at midrapidity vs. PSD centrality. Only statistical uncertainties are shown.

### 5.1.4 Results for elliptic flow

For the elliptic flow  $v_2$  results an average of the  $(y, x, y)$  and  $(y, y, x)$  correlations is used. These combinations have the smallest statistical uncertainties due to the geometry of the TPCs.

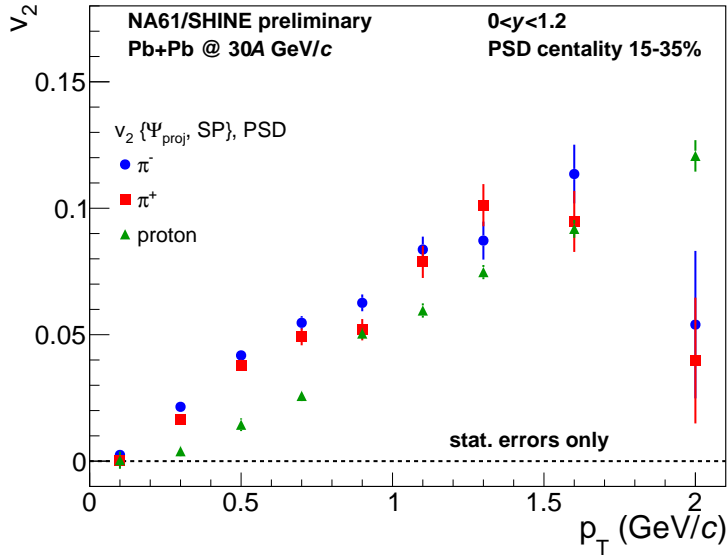


Figure 5.10: Charged pion and proton elliptic flow as a function of transverse momentum  $p_T$  for 15-35% PSD centrality class. Only statistical uncertainties are shown.

Results for  $\pi^-$ ,  $\pi^+$  and proton elliptic ( $v_2$ ) flow for the 15-35% centrality class are presented in 5.10. A strong mass dependence is observed. The difference between  $\pi^-$ ,  $\pi^+$   $v_2$  is small.

The centrality dependence of elliptic flow for positively charged pions and negatively charged pions are presented in figures 5.11 and 5.12, respectively. A strong centrality dependence is observed.

The centrality dependence of elliptic flow for protons is shown in figure 5.13. As well as for pions, a strong centrality dependence is observed.

The comparison with STAR results [85] is shown in figure 5.14. Track selection cuts were adjusted to be the same as in STAR analysis.

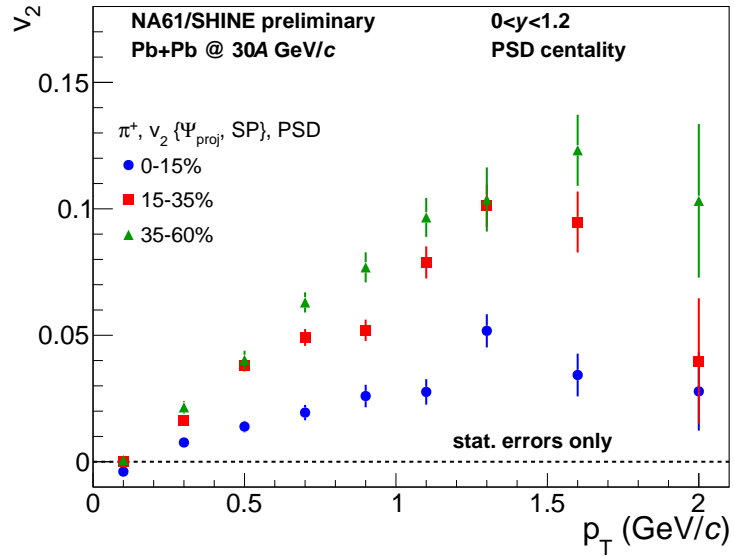


Figure 5.11: Positively charged pion elliptic flow as a function of transverse momentum  $p_T$  for different centrality classes. Only statistical uncertainties are shown.

Similar results for central and peripheral collisions are observed. Tension for mid-central collisions could be due to the different centrality estimators: particle multiplicity at midrapidity (STAR) and Projectile spectators (NA61/SHINE).

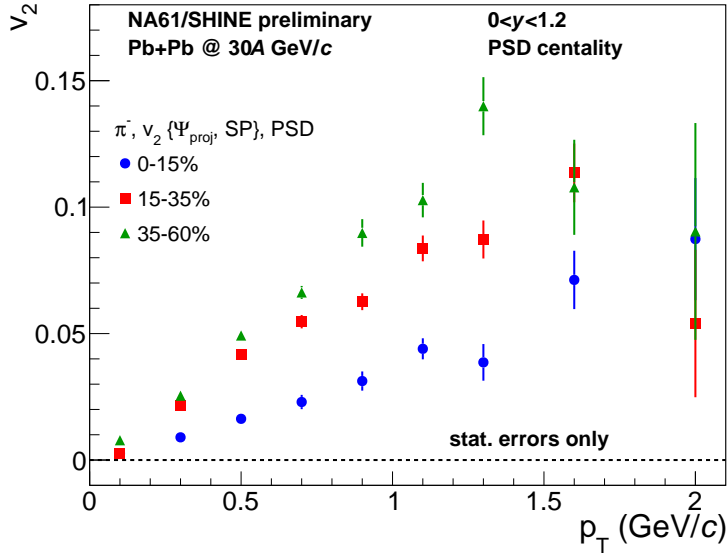


Figure 5.12: Negatively charged pion elliptic flow as a function of transverse momentum  $p_T$  for different centrality classes. Only statistical uncertainties are shown.

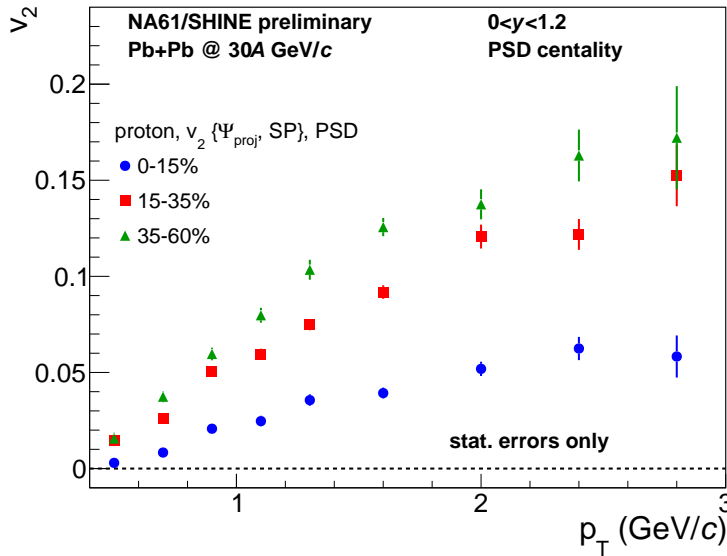


Figure 5.13: Proton elliptic flow as a function of transverse momentum  $p_T$  for different centrality classes. Only statistical uncertainties are shown.

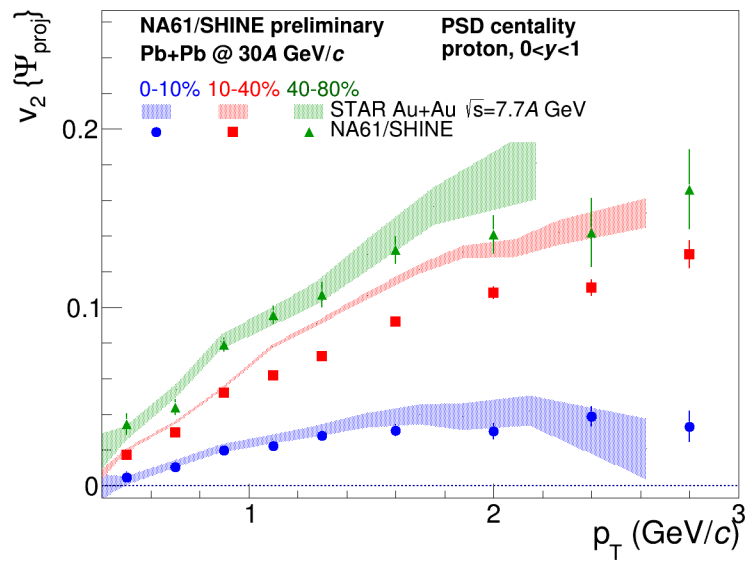


Figure 5.14: Proton elliptic flow as a function of transverse momentum  $p_T$  for different centrality classes. Only statistical uncertainties are shown.



## 5.2 CBM performance

Results are presented for correlations between charged hadrons (in the STS and MVD acceptance) and all hadrons at forward rapidity (in the PSD acceptance). Charged hadrons (pions, kaons and protons) are not corrected for weak decays contribution.

### 5.2.1 Correction for detector effects

#### PSD hole size effects

In this section the effect of the PSD hole size is discussed. A hole of 20 x 20 cm is needed to avoid radiation damage of the detector by the high-intensity beam. The results are compared to a hole size of 7 x 7 cm and to a setup without any hole in the PSD. To study the effect of the hole, 300 k minimum bias Au+Au collisions @ 10A GeV/ $c$  were simulated with DCM-QGSM model with coalescence and fragment decay afterburner. The CBM detector response is simulated using CBMROOT version Jul17.

Three versions of PSD detector geometry were simulated: without a hole, with 7 x 7 cm and 20 x 20 cm hole (diamond shape). To quantify the effect of introducing a hole, the resolution factors for all geometries are calculated using correlation with MC-true reaction plane:

$$R_1 = \langle Q \cos \Psi_{RP} \rangle \quad (5.1)$$

The resolution correction factor for the center part of the detector PSD1 (four central modules) is shown in figure 5.15. For a hole size of 20 x 20 cm, a better sensitivity for the reaction plane direction is observed. This can be explained by the improved PSD performance without any heavy fragments, which have smaller sensitivity to reaction plane angle. The effect is largest for peripheral collisions

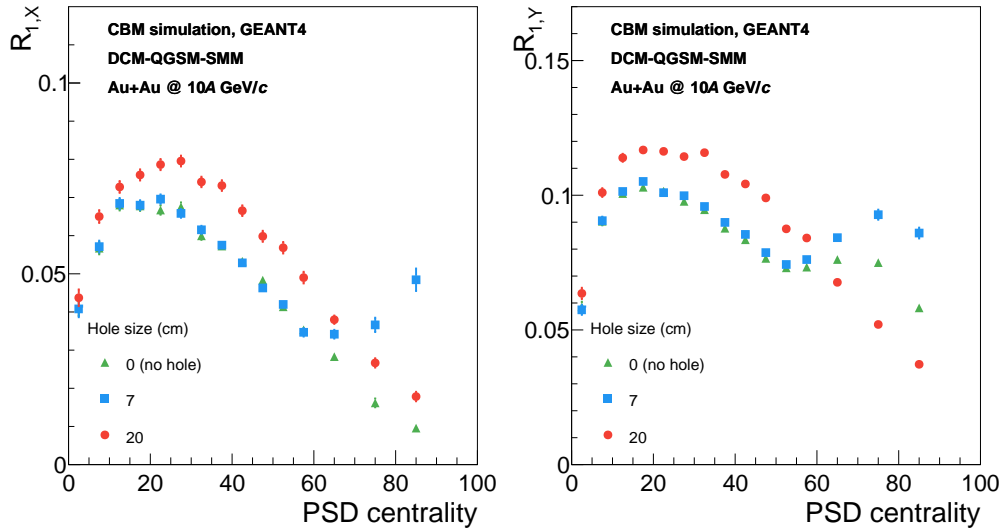


Figure 5.15: Scalar product resolution correction factor  $R$  for central part of the Projectile Spectator Detector (PSD1) for  $x$  (left) and  $y$  (right) component.

and almost not visible for central collisions.

The resolution correction factor is presented in figures 5.16 and 5.17 for middle and outer parts of PSD (PSD2 and PSD3) respectively. The observed difference between PSD geometries is smaller if we move to the outer part of the detector, but still is visible even for outer modules. That is consistent with previous observations that the transverse width of the hadronic shower is larger than module size.

For positively charged pions (identified using MC-true information), the directed flow vs. rapidity is shown in figure 5.18. For the reaction plane estimation the central part of PSD (PSD1) is used. All three tested geometries allow to reconstruct the initial MC-true flow.

In summary, increasing the PSD hole to 20 x 20 cm improves the sensitivity for the reaction plane reconstruction, and has a small positive effect for the flow measurement performance. However, the main limiting factor comes from the centrality estimation, where the PSD performance is significantly worse compared

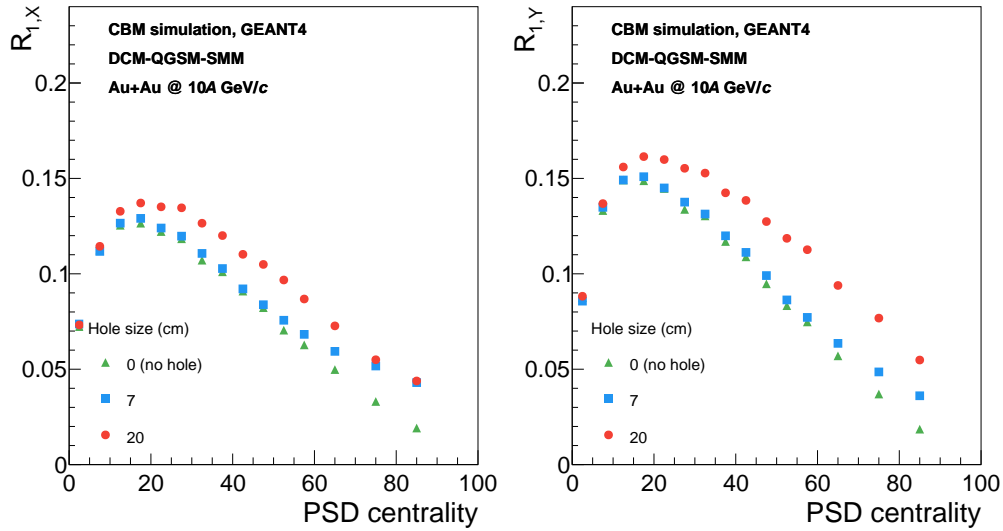


Figure 5.16: Scalar product resolution correction factor  $R$  for middle part of the Projectile Spectator Detector (PSD2) for  $x$  (left) and  $y$  (right) component.

to the configuration without a hole (details discussed in the section 4.5.5).

### Correction for tracking efficiency

The correction procedure for the tracking efficiency is equivalent to the one used for NA61/SHINE data. The tracking efficiency map for pions (left) and protons (right) is shown in the 5.20

$$\varepsilon = \frac{N_{rec}^{matched}}{N_{MC}} \quad (5.2)$$

One can estimate the reaction plane angle with spectators detected in the PSD and determine the flow of produced particles detected in the STS with respect to this plane. For event plane determination the PSD modules were subdivided into 3 groups (PSD1, PSD2, PSD3) with approximate coverage in pseudorapidity  $\eta \in \{(4.4, \infty), (3.7, 4.4), (3.1, 3.7)\}$ .

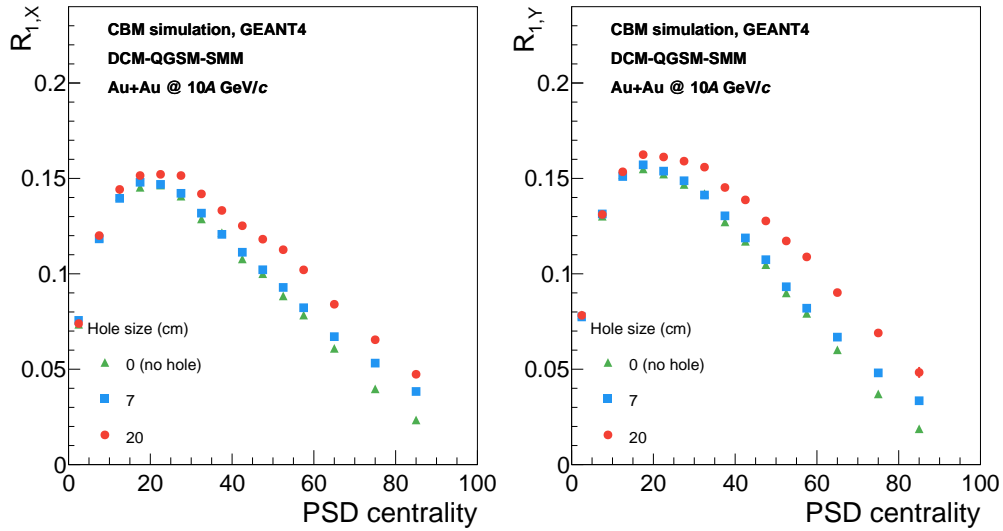


Figure 5.17: Scalar product resolution correction factor  $R$  for outer part of the Projectile Spectator Detector (PSD3) for  $x$  (left) and  $y$  (right) component.

## 5.2.2 Results for directed flow

In figure 5.21 the directed flow for positively charged pions vs. transverse momentum is shown. The centrality is defined using the PSD energy deposition as described in section 4.5. Events with 5-10% centrality are selected. The event plane is estimated with inner (PSD1) and outer (PSD3) parts of the Projectile Spectator Detector. Both measurements show consistent results with each other, and MC-true calculation results. The directed flow has a minimum at around 0.2 GeV/c.

The rapidity dependence of the same observable shown in figure 5.22. Reconstructed values of directed flow are consistent with MC-true in all centrality classes. The directed flow crosses 0 at midrapidity.

The directed flow for positively charged kaon vs. rapidity  $y$  is shown in figure 5.23. Both PSD estimations show consistent results with MC-true. Similarly to pions, the directed flow crosses 0 at midrapidity. The statistical uncertainties

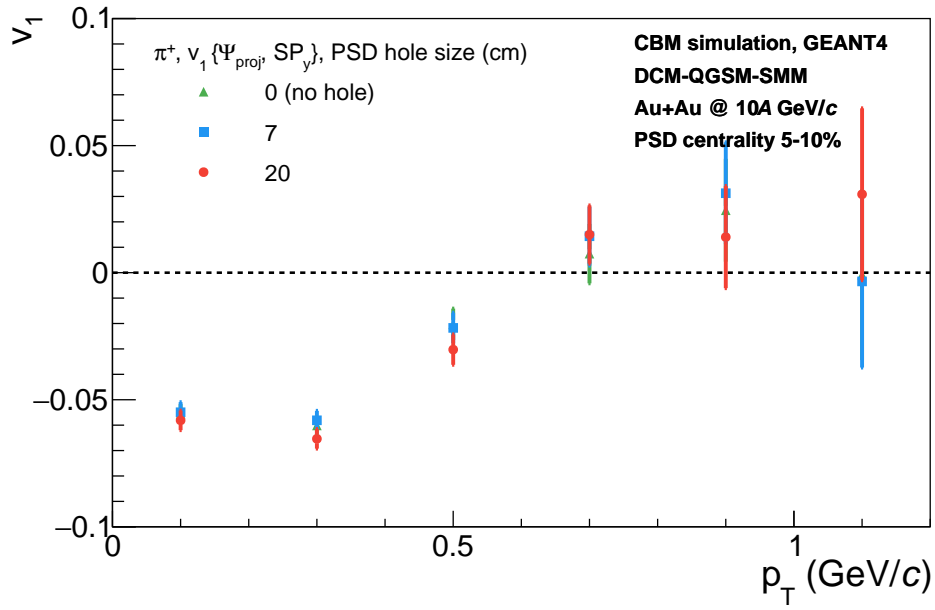


Figure 5.18: Positively charged pions (MC-true) directed flow vs. transverse momentum  $p_T$  for PSD centrality class 5-10%. With different colors PSD geometries with hole size from 0 (no hole) to 20 cm are indicated.

are rather large, so for future extensive studies of the CBM performance for the flow of strange particles larger statistics is required.

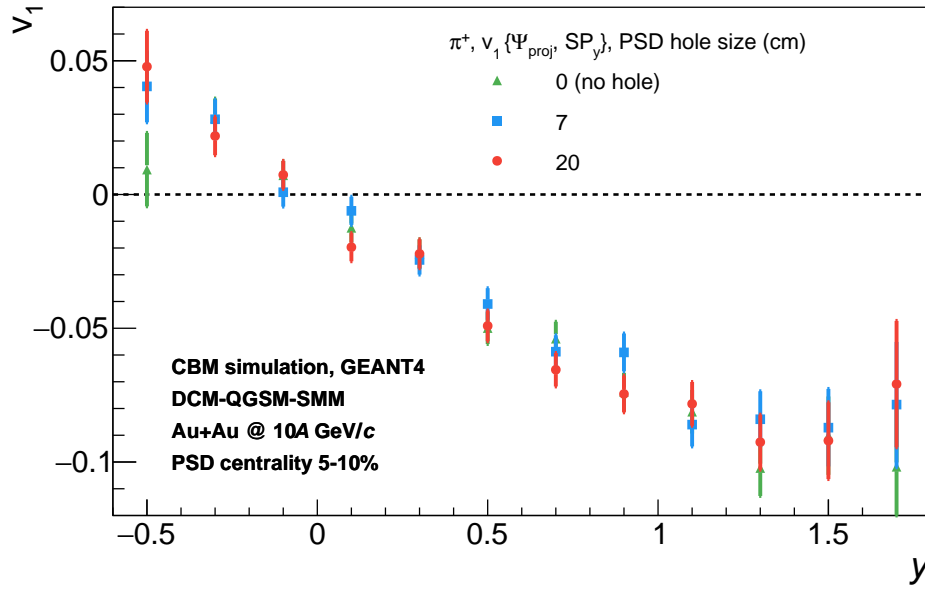


Figure 5.19: Positively charged pions (MC-true) directed flow vs. rapidity  $y$  for PSD centrality class 5-10%. With different colors PSD geometries with hole size from 0 (no hole) to 20 x 20 cm are indicated.

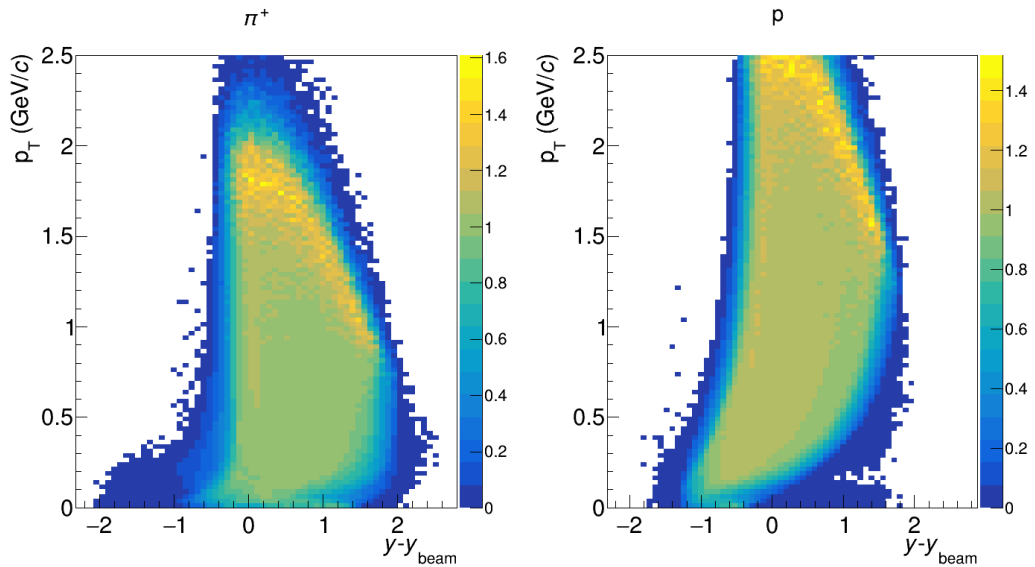


Figure 5.20: Tracking efficiencies for positively charged pion (left) and proton (right) as a function of transverse momentum and rapidity.

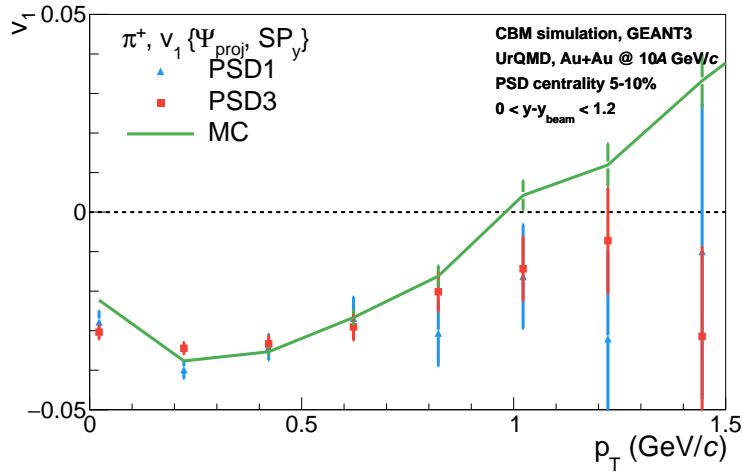


Figure 5.21: Directed flow of positively charged pions vs. transverse momentum  $p_T$  compared to the Monte-Carlo true calculation for centrality class 5-10%. Only statistical uncertainties are shown.

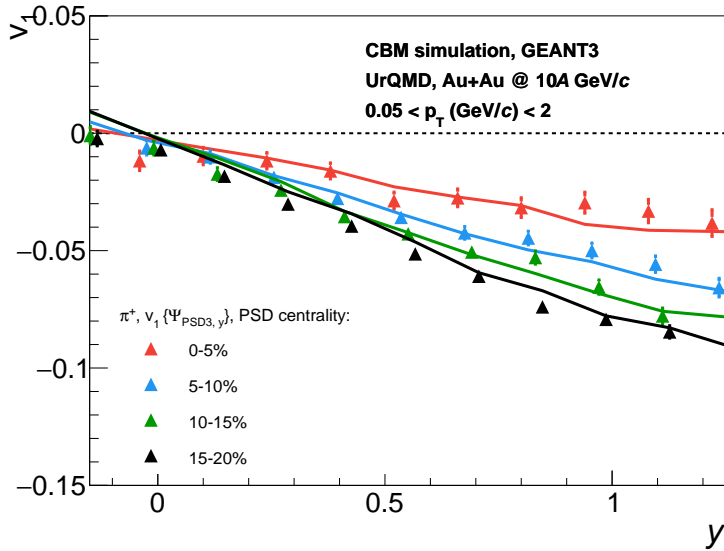


Figure 5.22: Directed flow of positively charged pions vs. rapidity  $y$  compared to the Monte-Carlo true calculation (indicated with lines) for centrality classes from 0 to 20%. Only statistical uncertainties are shown.

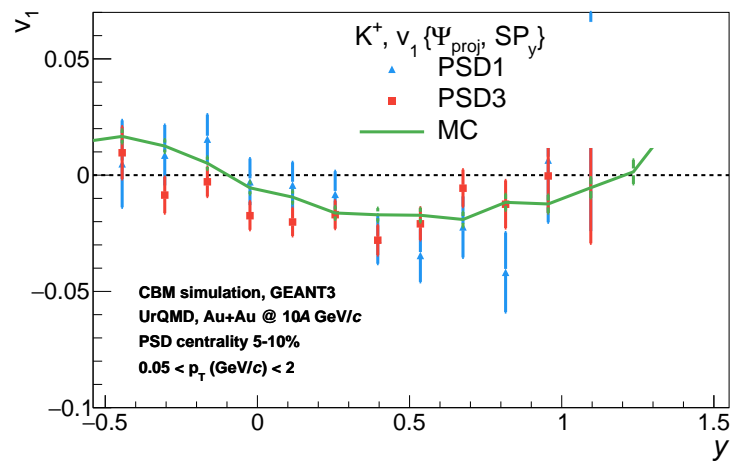


Figure 5.23: Directed flow of positively charged kaons vs. rapidity  $y$  compared to the Monte-Carlo true calculation for centrality class 5-10%. Only statistical uncertainties are shown.



# Chapter 6

## Conclusions and outlook

### Motivation

One of the ways to explore the QCD phase diagram is heavy-ion collisions. In heavy-ion collisions, the initial geometry and relative position of the nuclei play an important role. During the evolution of the created medium, the spatial anisotropy of the energy density converts to momentum anisotropy of the produced particles due to interaction between them. In an asymmetrical medium, the pressure gradient will be also asymmetrical. The anisotropy of the produced particles in the final stage can be measured experimentally.

The flow harmonics correspond to the asymmetry for a given harmonics in the Fourier expansion of the distribution. The magnitude of  $v_n$  depends on the system size, energy, centrality and other event and particle properties. The main feature of anisotropic flow is its sensitivity to early stages of collision. It originates from the particles spatial anisotropy in initial stage, which vanishes already in first few  $fm/c$  of the collision.

In this thesis, anisotropic flow measurements for SPS and FAIR energies are presented. Also within this work several tools for analysis, such as particle identification and centrality frameworks were developed, as well as a TPC calibration

procedure for NA61/SHINE detector.

## Calibration tools and analysis frameworks

### Calibration

Within this work the following parameters of the NA61/SHINE TPCs were calibrated: global and chamber  $T_0$ , Multihit time-to-digital converter calibration, drift velocity  $v_D$ , chamber positions in  $y$ -direction. The NA61/SHINE calibration software was improved (Stages 2 and 4) and successfully tested and applied for Pb+Pb collisions. The typical resolution for drift velocity calibration is less than 1‰, and the TPC  $y$ -position resolution is of the order of 100  $\mu\text{m}$ . The calibration results were submitted to the NA61/SHINE DataBase, and are used for official productions.

### Centrality

An objected oriented C++ framework for centrality analysis was developed. The basic functionality includes:

- Estimate trigger / event reconstruction / etc biases using MC-Glauber fit
- Divide events into classes based on any observable or correlation of two observables
- Map event classes to geometrical model parameters
- Store information into output object
- Getting centrality class for a given value of observable

It was tested using CBM simulation results and NA61/SHINE data. The framework is (well) documented and a modular code structure allows for a future

extensions. It will be included in the CBMROOT as external package, and can be used independently as a standalone framework.

## Particle identification

A C++ framework for particle identification analysis was developed. The basic functionality includes:

1. Parametrize  $m^2$  distribution in slices of momentum:
2. Parametrize momentum dependence of the fit parameters. Repeat until parameters are stabilized.
3. Save fit parameters to the ROOT file for further use in the analysis.
4. Calculate a bayesian probability

This procedure can be applied to different centrality classes. In this case the 2D histogram for each centrality class should be fitted separately. It was tested using CBM Time-Of-Flight simulation for the charged hadron identification. The framework can be used as standalone package and will be included to CBMROOT.

## Results of the anisotropic flow measurements

In this work the CBM performance for anisotropic flow measurements is studied with Monte-Carlo simulations using gold ions at SIS-100 energies employing different heavy-ion event generators. The resulting performance of CBM for flow measurements is demonstrated for positively charged pions and kaons directed flow as a function of rapidity and transverse momentum in different centrality classes. The CBM detector and the developed analysis techniques allow for precise anisotropic flow measurements using the forward calorimeter PSD.

In this thesis an analysis of the anisotropic flow harmonics in Pb+Pb collisions at beam momenta  $30A$  GeV/ $c$  collected by the NA61/SHINE experiment in the

year 2016 is presented. Flow coefficients are measured relative to the spectator plane estimated with the Projectile Spectators Detector (PSD). Transverse momentum and rapidity dependence of the directed and elliptic flow is presented for different centrality classes. The results are compared to the corresponding NA49 data, and to the measurements from the RHIC BES program.

## **PSD beam hole size effect on physics performance**

To reduce the radiation damage by the high-intensity beam, the PSD geometry includes a diamond shaped hole of size 20 x 20 cm in the middle for the beam pipe. In this work the PSD performance for the centrality and event plane determination is discussed, and compared to a previous study as described in the PSD TDR, which was done with a 6 cm diameter hole. For the centrality estimation, in a case of 20 x 20 cm hole correlation between registered energy and geometrical model parameters, such as impact parameter, is completely degraded. In this setup, an additional detector is needed to estimate the centrality together with the PSD. Additional studies with a combination of other detectors are needed to study the centrality estimation performance. For the flow measurement, increasing the PSD hole to 20 x 20 cm, improves the sensitivity for the reaction plane reconstruction and has a small positive effect for the performance.

## **Outlook**

The developed frameworks are well structured and documented, which allows for a further extension and improvement. The work presented in this thesis is rather a first step for a future CBM physics performance studies.

For the NA61/SHINE data, measurements could be extended to other colli-

sions systems, such as Xe+La, Ar+Sc, and Be+Be collisions, which are available from the system size scan of the NA61/SHINE experiment.



# List of Figures

1.1	The Standard Model of elementary particles [1] . . . . .	7
1.2	Schematic phase diagram of dense nuclear matter, in the baryon chemical potential $\mu_B$ - temperature $T$ plane [2]. . . . .	9
1.3	A schematic picture of the the transition from nuclear to deconfined quark matter with increasing density [2]. . . . .	10
1.4	The neutron star mass-radius relation as predicted by different Equations of State [4]. . . . .	11
1.5	Possible structure of the neutron star [9]. . . . .	12
1.6	Distributions of the rest-mass density $\rho$ in units of $\rho_0$ (left panel) and the temperature (right panel) on the equatorial plane at a post-merger time of $t=6.34$ ms for the LS220-M132 binary [12]. . . . .	13
1.7	Stages of a heavy-ion collision [15]. . . . .	14
2.1	Left: the two nuclei approach each other along the direction of the $z$ -axis with impact parameter $b$ . The plane spanned by $b$ and $e_z$ is the reaction plane. Right: the spatial asymmetry develops through multiple scattering into a momentum asymmetry. Taken from [41]. . . . .	18

2.2	The illustration of the definitions of the reaction plane and participant plane ( $PP$ ) coordinate systems [42]. The distribution of the produced particles does not coincide with the reaction plane due to the fluctuations. . . . .	19
2.3	Directed flow slope for protons and pions at midrapidity vs. Au+Au collision energy (left). Statistical (bars) and systematic (shaded area) uncertainties are shown separately. Elliptic flow slope at midrapidity vs. collision energy [45] (right). . . . .	21
2.4	Directed flow $v_1$ for pions (left) and protons (right) vs. rapidity (top) and transverse momentum (bottom) for Pb+Pb collision @ 40A GeV beam energy. Three different centralities are shown in different colors. . . . .	22
2.5	Mid-rapidity directed flow slope versus beam energy for for baryons (left). Elliptic flow $v_2$ for pions and protons (right) [47]. . . . .	23
2.6	Schematic illustration of the recentering correction step. . . . .	27
2.7	Schematic illustration of the twist correction step. . . . .	28
2.8	Schematic illustration of the rescale correction step. . . . .	29
2.9	Elliptic flow $v_2$ of charged particles estimated with event planes from different ALICE detectors. . . . .	30
3.1	Schematic view of the Future Facility for Antiproton and Ion Research. . . . .	32
3.2	Interaction rates as function of collision energy for existing and planned heavy-ion experiments. . . . .	33
3.3	The CBM experimental setup. For muon measurements, the RICH detector will be replaced by the MuCH, which is shown to the right of the beam axis. . . . .	36
3.4	CBM Dipole magnet geometry implementation in CBMROOT (geometry version 18a). . . . .	37



---

3.5	Schematic view of the Micro Vertex Detector. . . . .	38
3.6	Schematic view of the Silicon Tracking System. . . . .	39
3.7	Schematic view of the Time-of-Flight wall. . . . .	40
3.8	Transverse layout of the Projectile Spectator Detector. With different colors regions with sensitivity to spectator fragments are highlighted. . . . .	41
3.9	The Super Proton Synchrotron as part of current particle accelerator complex at CERN. . . . .	43
3.10	Layout of the NA61/SHINE experiment. . . . .	44
3.11	Transverse layout of the Projectile Spectator Detector. With different colors regions with sensitivity to spectator fragments are highlighted. . . . .	45
4.1	Azimuthal angle $\varphi$ distribution vs. transverse momentum $p_T$ for MC-true protons (left) and MC-true positively charged pions (right) after track selection. . . . .	51
4.2	Pseudorapidity $\eta$ distribution vs. transverse momentum $p_T$ for all charged particles reconstructed with STS+MVD after track selection. . . . .	51
4.3	PSD energy vs. multiplicity correlation for central T2 trigger. . .	53
4.4	PSD energy vs. multiplicity correlation for minimum bias T4 trigger. . . . .	54
4.5	Azimuthal angle $\varphi$ distribution vs. pseudorapidity $\eta$ for all charged particles after track selection. . . . .	56
4.6	Transverse momentum $p_T$ vs. pseudorapidity $\eta$ for all charged particles after track selection. . . . .	57
4.7	Azimuthal angle $\varphi$ vs. transverse momentum $p_T$ for all charged particles after track selection. . . . .	58
4.8	TPC time sampling (global $T_0$ calibration). . . . .	60

4.9	Illustration of drift velocity calibration procedure on TOF and one of the MTPCs example. . . . .	61
4.10	Illustration of drift velocity calibration sequence. With red arrows direction of calibration is shown, with grey arrow combination which was used only for cross-check. . . . .	62
4.11	$\Delta y$ vs $y$ after drift velocity calibration. With the red line linear fit is shown with 2 parameters slope and offset. . . . .	63
4.12	Illustration of the principle of the bottom point analysis for determination of the drift time measurement offset ( $T_0^{ch}$ ). . . . .	64
4.13	Specific energy loss $dE/dx$ vs. momentum $p$ for all charged tracks measured by the NA61/SHINE TPCs for Pb+Pb collisions at 30A GeV/c . . . . .	67
4.14	Mass square $m^2$ of particle calculated using TOF information vs. momentum for simulated Au+Au collisions @ 10A GeV/c . . . . .	68
4.15	One dimensional fitting procedure illustration. The square mass is calculated using TOF and tracking information from CBM simulation. The particle species as well as the background and the total fit function are shown in different colors. . . . .	69
4.16	Illustration of fit parameters momentum dependence approximation procedure. For the top plots with different colors different particle species are indicated. . . . .	70
4.17	Purity of selection given particle specie (shown with different colors) for one momentum bin. . . . .	71
4.18	Mass square $m^2$ vs. momentum for Au+Au @ 10A GeV/c after PID selection with purity cut of 90%. . . . .	72
4.19	Transverse momentum $p_T$ vs. rapidity $y$ for protons after tracks and PID selection. . . . .	73
4.20	Transverse momentum vs. rapidity for protons after tracks and PID selection. . . . .	74

---

4.21	Specific energy loss $dE/dx$ vs. momentum for pions and protons after tracks and PID selection. . . . .	75
4.22	Transverse momentum vs. rapidity for negatively (left) and positively (right) charged pions after tracks and PID selection. . . . .	76
4.23	Transverse momentum $p_T$ vs. rapidity $y$ for protons after tracks and PID selection. . . . .	76
4.24	Correlation between track multiplicity measured by STS and impact parameter $b$ . . . . .	79
4.25	Illustration of the 2D centrality determination procedure. The centrality is defined by the correlation between track multiplicity measured by STS+MVD and forward rapidity energy measured by PSD. The correlation is overlaid with a fit function and centrality classes borders. . . . .	84
4.26	PSD energy distribution vs. STS multiplicity for realistic GEANT4 simulation with PSD geometry without a hole. . . . .	85
4.27	PSD energy distribution vs. STS multiplicity for realistic GEANT4 simulation with PSD geometry with 7 cm hole (diamond shape). . . . .	86
4.28	PSD energy distribution vs. STS multiplicity for realistic GEANT4 simulation with PSD geometry with 20 cm hole (diamond shape). . . . .	87
4.29	Track multiplicity distribution (red) and MC-Glauber fit (blue). . . . .	88
4.30	Impact parameter distribution for each centrality classes indicated with different colors (left). Mean impact parameter in each centrality class vs. centrality (right). . . . .	89
4.31	PSD energy distribution for the CBM simulation. Dashed vertical lines mark the borders of event (centrality) classes. . . . .	89
4.32	Track multiplicity distribution (red) and MC-Glauber fit (blue). . . . .	90

4.33	PSD energy distribution for central (T2) and minimum bias (T4) triggers. Dashed vertical lines mark the borders of event (centrality) classes. . . . .	91
5.1	Tracking efficiency map for positively charged pions. . . . .	94
5.2	Tracking efficiency map for protons. . . . .	95
5.3	The first harmonic resolution correction factor calculated with the 3-subevent method. . . . .	96
5.4	Negatively charged pion directed flow for different event plane estimators in PSD centrality class 15-35%. Only statistical uncertainties are shown. . . . .	97
5.5	Negatively charged pion directed flow for $x$ and $y$ components in PSD centrality class 15-35%. Only statistical uncertainties are shown. . . . .	98
5.6	Negatively charged pion directed flow vs. transverse momentum $p_T$ for different centrality classes. Only statistical uncertainties are shown. . . . .	98
5.7	Negatively charged pion directed flow compared to a new analysis [83] of the NA49 Pb+Pb data at 40A GeV . The NA61/SHINE results are obtained using central PSD modules for centrality and projectile spectator plane ( $\Psi_{\text{proj}}$ ) estimation. Only statistical uncertainties are shown. . . . .	99
5.8	Charged pion and proton directed flow as a function of transverse momentum for 15-35% PSD centrality class. Only statistical uncertainties are shown. . . . .	99
5.9	Slope of directed flow at midrapidity vs. PSD centrality. Only statistical uncertainties are shown. . . . .	100

---

5.10 Charged pion and proton elliptic flow as a function of transverse momentum $p_T$ for 15-35% PSD centrality class. Only statistical uncertainties are shown. . . . .	101
5.11 Positively charged pion elliptic flow as a function of transverse momentum $p_T$ for different centrality classes. Only statistical uncertainties are shown. . . . .	102
5.12 Negatively charged pion elliptic flow as a function of transverse momentum $p_T$ for different centrality classes. Only statistical uncertainties are shown. . . . .	103
5.13 Proton elliptic flow as a function of transverse momentum $p_T$ for different centrality classes. Only statistical uncertainties are shown. . . . .	103
5.14 Proton elliptic flow as a function of transverse momentum $p_T$ for different centrality classes. Only statistical uncertainties are shown. . . . .	104
5.15 Scalar product resolution correction factor $R$ for central part of the Projectile Spectator Detector (PSD1) for $x$ (left) and $y$ (right) component. . . . .	106
5.16 Scalar product resolution correction factor $R$ for middle part of the Projectile Spectator Detector (PSD2) for $x$ (left) and $y$ (right) component. . . . .	107
5.17 Scalar product resolution correction factor $R$ for outer part of the Projectile Spectator Detector (PSD3) for $x$ (left) and $y$ (right) component. . . . .	108
5.18 Positively charged pions (MC-true) directed flow vs. transverse momentum $p_T$ for PSD centrality class 10-35%. With different colors PSD geometries with hole size from 0 (no hole) to 20 cm are indicated. . . . .	109

- 
- 5.19 Positively charged pions (MC-true) directed flow vs. rapidity  $y$  for PSD centrality class 10-35%. With different colors PSD geometries with hole size from 0 (no hole) to 20 x 20 cm are indicated. . . . 110
- 5.20 Tracking efficiencies for positively charged pion (left) and proton (right) as a function of transverse momentum and rapidity. . . . 110
- 5.21 Directed flow of positively charged pions vs. transverse momentum  $p_T$  compared to the Monte-Carlo true calculation for centrality class 10-35%. Only statistical uncertainties are shown. . . . . 111
- 5.22 Directed flow of positively charged pions vs. rapidity  $y$  compared to the Monte-Carlo true calculation for centrality class 10-35%. Only statistical uncertainties are shown. . . . . 111
- 5.23 Directed flow of positively charged kaons vs. rapidity  $y$  compared to the Monte-Carlo true calculation for centrality class 10-35%. Only statistical uncertainties are shown. . . . . 112

# List of Tables

1.1	Fundamental forces. . . . .	6
1.2	Dense baryonic matter properties at different conditions. . . . .	10
4.1	Simulated datasets used in this thesis. . . . .	49
4.2	Trigger definitions and approximate number of collected events for Pb+Pb @ 30A GeV/c . . . . .	52

# Bibliography

- [1] Standard model diagram. <http://www-f9.ijs.si/~lubej/SM.pdf>.
- [2] Gordon Baym, Tetsuo Hatsuda, Toru Kojo, Philip D. Powell, Yifan Song, and Tatsuyuki Takatsuka. From hadrons to quarks in neutron stars: a review. *Rept. Prog. Phys.*, 81(5):056902, 2018.
- [3] M. A. Stephanov. QCD phase diagram: An Overview. *PoS*, LAT2006:024, 2006.
- [4] Paul Demorest, Tim Pennucci, Scott Ransom, Mallory Roberts, and Jason Hessels. Shapiro Delay Measurement of A Two Solar Mass Neutron Star. *Nature*, 467:1081–1083, 2010.
- [5] J. R. Oppenheimer and G. M. Volkoff. On Massive neutron cores. *Phys. Rev.*, 55:374–381, 1939.
- [6] A. Einstein. Die Grundlage der allgemeinen Relativitätstheorie. *Annalen der Physik*, 354:769–822, 1916.
- [7] J. M. Lattimer and M. Prakash. Neutron star structure and the equation of state. *Astrophys. J.*, 550:426, 2001.
- [8] Yeunhwan Lim, Chang Ho Hyun, and Chang-Hwan Lee. Nuclear Equation of State and Neutron Star Cooling. *Int. J. Mod. Phys.*, E26(4):1750015, 2017.



- 
- [9] X. Roca-Maza, J. Piekarewicz, T. Garcia-Galvez, and M. Centelles. Influence of the nuclear symmetry energy on the structure and composition of the outer crust. 2011.
- [10] Feryal Ozel, Dimitrios Psaltis, Zaven Arzoumanian, Sharon Morsink, and Michi Baubock. Measuring Neutron Star Radii via Pulse Profile Modeling with NICER. *Astrophys. J.*, 832(1):92, 2016.
- [11] B. P. Abbott et al. Observation of Gravitational Waves from a Binary Black Hole Merger. *Phys. Rev. Lett.*, 116(6):061102, 2016.
- [12] Matthias Hanauske, Jan Steinheimer, Luke Bovard, Ayon Mukherjee, Stefan Schramm, Kentaro Takami, Jens Papenfort, Natascha Wechselberger, Luciano Rezzolla, and Horst Stöcker. Concluding Remarks: Connecting Relativistic Heavy Ion Collisions and Neutron Star Mergers by the Equation of State of Dense Hadron- and Quark Matter as signalled by Gravitational Waves. *J. Phys. Conf. Ser.*, 878(1):012031, 2017.
- [13] B. P. Abbott et al. GW170817: Observation of Gravitational Waves from a Binary Neutron Star Inspiral. *Phys. Rev. Lett.*, 119(16):161101, 2017.
- [14] B. P. Abbott et al. Multi-messenger Observations of a Binary Neutron Star Merger. *Astrophys. J.*, 848(2):L12, 2017.
- [15] Tapan K. Nayak. Heavy Ions: Results from the Large Hadron Collider. *Pramana*, 79:719–735, 2012.
- [16] AGS Experiments. <https://www.phy.bnl.gov/newphysics/experiments.html>.
- [17] Brookhaven National Laboratory. <https://www.bnl.gov/about/>.
- [18] Joint Institute for Nuclear Research. <http://www.jinr.ru/main-en/>.
- [19] A. Andronic et al. Excitation function of elliptic flow in Au+Au collisions and the nuclear matter equation of state. *Phys. Lett.*, B612:173–180, 2005.

- 
- [20] Y. J. Kim. Flow of strange particles from FOPI at SIS. *Int. J. Mod. Phys.*, A22:608–611, 2007.
- [21] A. Forster et al. Review of the results of the KaoS collaboration. *J. Phys.*, G31(6):S693–S700, 2005.
- [22] L. Adamczyk et al. Global  $\Lambda$  hyperon polarization in nuclear collisions: evidence for the most vortical fluid. *Nature*, 548:62–65, 2017.
- [23] HADES Collaboration. <https://www-hades.gsi.de/>.
- [24] Mikhail Kapishin. Studies of baryonic matter at the BM@N experiment (JINR). *Nucl. Phys.*, A982:967–970, 2019.
- [25] M. N. Kapishin. The Fixed Target Experiment for Studies of Baryonic Matter at the Nuclotron (BM@N). *Phys. Atom. Nucl.*, 80(10):1613–1619, 2017. [Yad. Fiz.7,no.6,543(2016)].
- [26] N. Abgrall et al. NA61/SHINE facility at the CERN SPS: beams and detector system. *JINST*, 9:P06005, 2014.
- [27] NA61/SHINE Collaboration. <http://shine.web.cern.ch/>.
- [28] STAR Collaboration. <https://www.star.bnl.gov/>.
- [29] K. Aamodt et al. The ALICE experiment at the CERN LHC. *JINST*, 3:S08002, 2008.
- [30] ALICE Collaboration. <http://aliceinfo.cern.ch/Public/Welcome.html>.
- [31] The Large Hadron Collider. <https://home.cern/science/accelerators/large-hadron-collider>.
- [32] Kathryn C. Meehan. The fixed-target experiment at STAR. *J. Phys. Conf. Ser.*, 742(1):012022, 2016.

- 
- [33] N. S. Geraksiev and Geraksiev. The Nuclotron-based Ion Collider Facility Project. The Physics Programme for the Multi-Purpose Detector. *J. Phys. Conf. Ser.*, 1023(1):012030, 2018.
- [34] V. D. Kekelidze, A. D. Kovalenko, I. N. Meshkov, A. S. Sorin, and G. V. Trubnikov. NICA at JINR: New prospects for exploration of quark-gluon matter. *Phys. Atom. Nucl.*, 75:542–545, 2012.
- [35] H. Sako et al. Towards the heavy-ion program at J-PARC. *Nucl. Phys.*, A931:1158–1162, 2014.
- [36] H. Stocker et al. Nuclear Fluid Dynamics versus Intranuclear Cascade—Possible Evidence for Collective Flow in Central High-Energy Nuclear Collisions. *Phys. Rev. Lett.*, 47:1807–1810, 1981.
- [37] H. A. Gustafsson et al. Collective Flow Observed in Relativistic Nuclear Collisions. *Phys. Rev. Lett.*, 52:1590–1593, 1984.
- [38] Jean-Yves Ollitrault. Anisotropy as a signature of transverse collective flow. *Phys. Rev.*, D46:229–245, 1992.
- [39] S. S. Adler et al. Elliptic flow of identified hadrons in Au+Au collisions at  $\sqrt{s_{NN}} = 200$ -GeV. *Phys. Rev. Lett.*, 91:182301, 2003.
- [40] K Aamodt et al. Elliptic flow of charged particles in Pb-Pb collisions at 2.76 TeV. *Phys. Rev. Lett.*, 105:252302, 2010.
- [41] Jacobus Onderwaater. *Charge correlations and collective dynamics in Pb-Pb collisions at  $\sqrt{s_{NN}} = 2.76$  TeV*. PhD thesis, Technische Universität, November 2017.
- [42] Sergei A. Voloshin, Arthur M. Poskanzer, and Raimond Snellings. Collective phenomena in non-central nuclear collisions. *Landolt-Bornstein*, 23:293–333, 2010.

- 
- [43] N. Borghini, P. M. Dinh, Jean-Yves Ollitrault, Arthur M. Poskanzer, and S. A. Voloshin. Effects of momentum conservation on the analysis of anisotropic flow. *Phys. Rev.*, C66:014901, 2002.
- [44] Peter F. Kolb and Ulrich W. Heinz. Hydrodynamic description of ultrarelativistic heavy ion collisions. pages 634–714, 2003.
- [45] Anton Andronic. Experimental results and phenomenology of quarkonium production in relativistic nuclear collisions. *Nucl. Phys.*, A931:135–144, 2014.
- [46] C. Alt et al. Directed and elliptic flow of charged pions and protons in Pb + Pb collisions at 40-A-GeV and 158-A-GeV. *Phys. Rev.*, C68:034903, 2003.
- [47] Yang Wu. Recent results for STAR  $\sqrt{s_{NN}} = 4.9$  GeV Al+Au and  $\sqrt{s_{NN}} = 4.5$  GeV Au+Au Fixed-Target Collisions. *Nucl. Phys.*, A982:899–902, 2019.
- [48] Behruz Kardan. Collective flow and correlations measurements with HADES in Au+Au collisions at 1.23 AGeV. *Nucl. Phys.*, A982:431–434, 2019.
- [49] Behruz Kardan. Collective flow measurements with HADES in Au+Au collisions at 1.23A GeV. *PoS*, CPOD2017:049, 2018.
- [50] B. Alver et al. System size, energy, pseudorapidity, and centrality dependence of elliptic flow. *Phys. Rev. Lett.*, 98:242302, 2007.
- [51] Matthew Luzum and Jean-Yves Ollitrault. Eliminating experimental bias in anisotropic-flow measurements of high-energy nuclear collisions. *Phys. Rev.*, C87(4):044907, 2013.
- [52] Ante Bilandzic, Raimond Snellings, and Sergei Voloshin. Flow analysis with cumulants: Direct calculations. *Phys. Rev.*, C83:044913, 2011.
- [53] Nicolas Borghini, Phuong Mai Dinh, and Jean-Yves Ollitrault. Flow analysis from multiparticle azimuthal correlations. *Phys. Rev.*, C64:054901, 2001.

- 
- [54] Ilya Selyuzhenkov and Sergei Voloshin. Effects of non-uniform acceptance in anisotropic flow measurement. *Phys. Rev.*, C77:034904, 2008.
- [55] Flow vector correction framework, available under GNU General Public License v.3. <https://github.com/FlowCorrections/FlowVectorCorrections>.
- [56] Alexander Malakhov and Alexey Shabunov, editors. *Technical Design Report for the CBM Superconducting Dipole Magnet*. GSI, Darmstadt, 2013.
- [57] Johann Heuser, Walter Müller, V. Pugatch, Peter Senger, Christian Joachim Schmidt, Christian Sturm, and Ulrich Frankenfeld, editors. [*GSI Report 2013-4*] *Technical Design Report for the CBM Silicon Tracking System (STS)*. GSI, Darmstadt, 2013.
- [58] Technical Design Report for the CBM Ring Imaging Cherenkov Detector. Technical report, 2013.
- [59] Technical Design Report for the CBM : Transition Radiation Detector (TRD). Technical report, 2018.
- [60] Subhasis Chattopadhyay, Yogendra Pathak Viyogi, Peter Senger, Walter F. J. Müller, and Christian J. Schmidt, editors. *Technical Design Report for the CBM : Muon Chambers (MuCh)*. GSI, Darmstadt, 2015.
- [61] Norbert Herrmann, editor. *Technical Design Report for the CBM Time-of-Flight System (TOF)*. GSI, Darmstadt, 2014.
- [62] Fedor Guber and Ilya Selyuzhenkov, editors. *Technical Design Report for the CBM Projectile Spectator Detector (PSD)*. GSI, Darmstadt, 2015.
- [63] S. A. Bass et al. Microscopic models for ultrarelativistic heavy ion collisions. *Prog. Part. Nucl. Phys.*, 41:255–369, 1998. [Prog. Part. Nucl. Phys.41,225(1998)].

- [64] M. Bleicher et al. Relativistic hadron hadron collisions in the ultrarelativistic quantum molecular dynamics model. *J. Phys.*, G25:1859–1896, 1999.
- [65] A. S. Botvina, K. K. Gudima, J. Steinheimer, M. Bleicher, and I. N. Mishustin. Production of spectator hypermatter in relativistic heavy-ion collisions. *Phys. Rev.*, C84:064904, 2011.
- [66] R. Brun, R. Hagelberg, M. Hansroul, and J. C. Lassalle. *Simulation program for particle physics experiments, GEANT: user guide and reference manual*. CERN, Geneva, 1978.
- [67] S. Agostinelli et al. GEANT4: A Simulation toolkit. *Nucl. Instrum. Meth.*, A506:250–303, 2003.
- [68] Peter Kövesarki and Andras Laszlo. Calibration chain with shine offline framework. 2014.
- [69] Peter Kövesarki. New calibration software (vd, t0, tpc shifts). <https://indico.cern.ch/event/267227/>, 2014.
- [70] Fons Rademakers Rene Brun. ROOT - An Object Oriented Data Analysis Framework. *Nucl. Inst. and Meth. in Phys. Res. A*, pages 81–86, 1997.
- [71] Jaroslav Adam et al. Particle identification in ALICE: a Bayesian approach. *Eur. Phys. J. Plus*, 131(5):168, 2016.
- [72] Silvestro di Luise. Tools for integrated na61/shine analysis. ”NA61/SHINE Analysis/Calibration/Software Meeting, Katowice, Jan. 2015”.
- [73] Particle identification framework. <https://git.cbm.gsi.de/pwg-c2f/analysis/pid>.
- [74] M. Zyzak. Online selection of short-lived particles on many-core computer architectures in the CBM experiment at FAIR. <http://d-nb.info/1112601619/34>, 2015.

- [75] Particle identification framework documentation. <http://web-docs.gsi.de/~klochkov/pid/>.
- [76] Betty Abelev et al. Centrality determination of Pb-Pb collisions at  $\sqrt{s_{NN}} = 2.76$  TeV with ALICE. *Phys. Rev.*, C88(4):044909, 2013.
- [77] B. I. Abelev et al. Centrality dependence of charged hadron and strange hadron elliptic flow from  $s(NN)^{1/2} = 200$ -GeV Au + Au collisions. *Phys. Rev.*, C77:054901, 2008.
- [78] C.Loizides. <https://tglaubermc.hepforge.org/>.
- [79] Centrality framework. <https://git.cbm.gsi.de/pwg-c2f/analysis/centrality>.
- [80] Centrality framework documentation. <http://web-docs.gsi.de/~klochkov/centrality/>.
- [81] NA61/SHINE Collaboration. Time Projection Chamber acceptance. <https://edms.cern.ch/document/1549298/1>.
- [82] NA61/SHINE Collaboration. Projectile Spectator Detector acceptance. <https://edms.cern.ch/document/1867336/1>.
- [83] O. Golosov, V. Klochkov, I. Selyuzhenkov and E. Kashirin [NA49 Collaboration]. QM2018 poster #367.
- [84] Andrzej Rybicki and Antoni Szczurek. Spectator induced electromagnetic effect on directed flow in heavy ion collisions. *Phys. Rev.*, C87(5):054909, 2013.
- [85] L. Adamczyk et al. Beam-Energy Dependence of the Directed Flow of Protons, Antiprotons, and Pions in Au+Au Collisions. *Phys. Rev. Lett.*, 112(16):162301, 2014.

- 
- [86] V. Klochkov and I. Selyuzhenkov. NA61/SHINE measurements of anisotropic flow relative to the spectator plane in Pb+Pb collisions at 30A GeV/c. *Nucl. Phys.*, A982:439–442, 2019.
- [87] V. Klochkov and I. Selyuzhenkov. CBM Performance for Anisotropic Flow Measurements. *KnE Energ. Phys.*, 3:416–421, 2018.
- [88] V. Klochkov and I. Selyuzhenkov. Centrality Determination in Heavy-ion Collisions with CBM. *Acta Phys. Polon. Supp.*, 10:919, 2017.
- [89] Klochkov and I. Selyuzhenkov. Centrality determination in heavy-ion collisions with the CBM experiment. *J. Phys. Conf. Ser.*, 798(1):012059, 2017.
- [90] E. Zherebtsova, V. Klochkov, I. Selyuzhenkov, A. Taranenko, and E. Kashirin. Procedure for event characterization in Pb-Pb collisions at 40A GeV in the NA49 experiment at the CERN SPS. *EPJ Web Conf.*, 182:02132, 2018.



# Zusammenfassung

Diese Arbeit basiert auf folgenden Publikationen:

- "NA61/SHINE measurements of anisotropic flow relative to the spectator plane in Pb+Pb collisions at 30A GeV/c"  
V. Klochkov and I. Selyuzhenkov  
Proceedings, 27th International Conference on Ultrarelativistic Nucleus-Nucleus Collisions (Quark Matter 2018): Venice, Italy, May 14-19, 2018 [86]
- "CBM Performance for Anisotropic Flow Measurements"  
V. Klochkov and I. Selyuzhenkov  
Proceedings, 3rd International Conference on Particle Physics and Astrophysics (ICPPA 2017): Moscow, Russia, October 2-5, 2017 [87]
- "Centrality Determination in Heavy-ion Collisions with CBM"  
V. Klochkov and I. Selyuzhenkov  
Proceedings, 10th International Workshop on Critical Point and Onset of Deconfinement (CPOD 2016): Wroclaw, Poland, May 30-Juni 4, 2016 [88]
- "Centrality determination in heavy-ion collisions with the CBM experiment"  
V. Klochkov and I. Selyuzhenkov  
Proceedings, 2nd International Conference on Particle Physics and Astrophysics (ICPPA 2016): Moscow, Russia, October 10-14, 2016 [89]

- "Procedure for event characterization in Pb-Pb collisions at 40A GeV in the NA49 experiment at the CERN SPS"  
E. Zherebtsova, V. Klochkov, I. Selyuzhenkov, A. Taranenko and E. Kashirin  
Proceedings, 6th International Conference on New Frontiers in Physics (IC-NFP 2017): Crete, Greece, August 17-29, 2017 [90]

## Motivation

Eine der Möglichkeiten, das QCD-Phasendiagramm zu untersuchen, sind Schwerionenkollisionen. Bei Schwerionenkollisionen spielen die Ausgangsgeometrie und die relative Position der Kerne eine wichtige Rolle. Während der Evolution des erzeugten Mediums wandelt sich die räumliche Anisotropie der Energiedichte in die Impulsanisotropie der produzierten Partikel durch Interaktion zwischen ihnen. In einem asymmetrischen Medium ist der Druckgradient ebenfalls asymmetrisch. Die Anisotropie der erzeugten Teilchen im Endstadium kann experimentell gemessen werden. Die Flusskoeffizienten entsprechen der Asymmetrie für eine bestimmte Harmonische in der Fourierreihe der Verteilung. Die Größe von  $v_n$  hängt von der Systemgröße, der Energie, der Zentralität und anderen Ereignis- und Teilcheneigenschaften ab. Das Hauptmerkmal des anisotropen Flusses ist seine Empfindlichkeit gegenüber frühen Phasen der Kollision. Es stammt von der räumlichen Anisotropie der Teilchen im Anfangsstadium, die bereits in den ersten paar  $fm/c$  der Kollision verschwindet.

In dieser Arbeit werden Messungen und Simulationen des anisotropen Flusses für SPS- und FAIR-Energien vorgestellt. Im Rahmen dieser Arbeit wurden auch verschiedene Programmpakete zur Teilchenidentifikation- und Zentralitätsbestimmung, sowie TPC-Kalibrierverfahren für den NA61/SHINE -Detektor entwickelt.

# Kalibrierungs- und Analyseverfahren

## Kalibrierung

Im Rahmen dieser Arbeit wurden folgende Parameter der NA61/SHINE TPCs kalibriert: Global und Kammer  $T_0$ , Multihit Time-to-Digital-Wandler-Kalibrierung, Driftgeschwindigkeit  $v_D$ , Kammerpositionen in  $y$ -Richtung. Die NA61/SHINE -Kalibrierungssoftware wurde verbessert (Stufen 2 und 4) und erfolgreich getestet und auf Blei-Blei-Kollisionen angewendet. Die typische Auflösung für die Driftgeschwindigkeitskalibrierung beträgt weniger als 1‰ und TPC  $y$ -Positionsauflösung liegt in der Größenordnung von  $100 \mu m$ . Die Kalibrierergebnisse wurden an die NA61/SHINE -Datenbank übermittelt und für offizielle Produktionen verwendet.

## Zentralität

Ein objektorientiertes C++ Programmpaket zur Zentralitätsbestimmung wurde entwickelt. Die Grundfunktionalität umfasst:

- Analyse des Einflusses von Trigger und Ereignisrekonstruktion auf die Zentralitätsselektion
- Unterteil und der Ereignisse in Klassen, die auf einer beobachtbaren Kombination von zwei beobachtbaren Ereignissen basieren.
- Zuordnung von Ereignisklassen zu geometrischen Modellparametern
- Speichern von Informationen im Ausgabeobjekt

Es wurde mit CBM-Simulation und NA61/SHINE -Daten getestet. Das Programmpaket ist (gut) dokumentiert und eine modulare Codestruktur ermöglicht zukünftige Erweiterungen. Es ist in CBMROOT als externes Paket enthalten und

kann unabhängig voneinander als stanolones Gerüst verwendet werden. Detailliertere Informationen über die C++-Implementierung mit Beispielen und HowTo finden Sie in der Projektdokumentation [80].

## Teilchenidentifikation

Ein C++ Programmpaket für die Teilchenidentifikationsanalyse wurde entwickelt. Die Grundfunktionalität umfasst:

1. Parametrisieren die  $m^2$ -Verteilung in Scheiben des Impulses:
2. Parametrisieren der Impulsabhängigkeit der Anpassungsparameter. Wiederholen Sie dies, bis die Parameter stabilisiert sind.
3. Speichern die Fit-Parameter in der ROOT-Datei zur weiteren Verwendung in der Analyse.
4. Berechnen der bedingten Wahrscheinlichkeit nach Bayes.

Dieses Verfahren kann in verschiedenen Zentralitätsklassen angewendet werden. In diesem Fall sollte das 2D-Histogramm für jede Zentralitätsklasse separat angepasst werden. Es wurde mit Hilfe der CBM Time-Of-Flight-Simulation für die Identifizierung der geladenen Hadronen getestet. Das Programmpaket kann separat oder als Teil von CBMROOT verwendet werden. Detaillierte Informationen zur C++-Implementierung mit Beispielen und HowTo enthält die in der Projektdokumentation [75].

## Bestimmung des anisotropen Teilchenflusses

In diese Arbeit wird die Bestimmung des anisotropen Teilchenflusses mit dem CBM-Detectorsystem untersucht. Dazu werden Monte-Carlo-Simulationen von Gold-Gold Stößen bei SIS-100 Energien mithilfe verschiedener Ereignisgenerationen durchgeführt. Anhand von Ergebnissen zum kollektiven Fluss von Pionen

and Kaonen als Funktion von Rapidity und Transversalimpuls für verschiedene Zentralitätsklassen wird die Qualität der neu entwickelten Analysetechniken für verschiedenen Konfigurationen des PSD Vorwandskalorimeter demonstriert. Im Rahmen dieser Arbeit wird weiterhin eine Analyse des anisotropen Teilchenflusses in Blei-Blei-Kollisionen bei Strahlimpulsen von 30A GeV/c vorgestellt. Analysiert wurden Daten, die mithilfe des NA61/SHINE Experiments im Jahre 2016 gemessen wurden, unter Verwendung eines PSD, der zur Bestimmung der Reaktionsebene dient. Der gerichtete und elliptische Teilchenfluss wird als Funktion des Transversalimpulses und der Rapidity für verschiedene Zentralitätsklassen analysiert. Die Ergebnisse werden mit entsprechenden Daten von NA49 und dem RHIC-BES-Programm verglichen.

## **Anpassung der PSD Geometrie für SIS-100-Strahlen**

Der PSD des CBM-Experiments an SIS-100 wird bei Strahlintensitäten betrieben, die etwa vier Größenordnungen höher sind als bei NA61/SHINE. Daher muss in der Mitte des CBM-PSD eine Öffnung für das Strahlrohr vorgesehen werden, um Strahlenschäden zu reduzieren. Geplant ist ein diamantförmiges Loch der Größe 20 cm x 20 cm. Die Auswirkungen dieser Geometrie auf die Bestimmung der Zentralität des Stoßes und die Ereignisebene werden untersucht, und mit einer früheren Studie verglichen, die mit einem Loch von 6 cm durchgeführt wurde. Es wird gezeigt, dass bei einem Loch von 20 cm x 20 cm die Korrelation zwischen im PSD registrierter Energie und Zentralität bei peripheren Stoßen verloren geht, da die schweren Fragmente und kleinen Vorwärtswinkeln nicht mehr nachgewiesen werden. Es ist daher ein weiterer, hochdruckfester Detektor erforderlich, um die Zentralität in Verbindung mit dem PSD zu bestimmen. Die Genauigkeit der Bestimmung der Orientierung der Reaktionsebene wird hingegen

durch das größere Loch verbessert, da viele der schweren Fragmenten die unter kleinen Vorwärtewinkeln emittiert und nicht nachgewiesen werden, nur schwach mit der Reaktionsebene korreliert sind

## **Ausblick**

In dieser Arbeit vorgestellten Simulationen und Analysen bilden die Grundlage für detaillierte Studien zur Physik-Performanz des CBM-Experiments bezüglich der Messungen des Kollektiven Fluss von identifizierten Teichen. Darüber hinaus können die entwickelten Analysemethoden und Programme auf weiterer Kollisionssysteme wie Xa+La, Ar+Sc, Be+Be, die bereits von NA61/SHINE gemessen wurden angewendet werden.

# Acknowledgements

I would like to thank all people who supported me during past almost four years.

First of all, I would like to express my deep sense of gratitude to my mentor Dr. Ilya Selyuzhenkov for his constant support and fruitful discussions often outside of working hours and sometimes with a glass of beer. During this time I've learned a lot from him and I could not wish for a better supervisor.

I would like to thank Prof. Dr. Peter Senger for opportunity to join the CBM Collaboration and motivating young people including myself to do research in this field. Also, thanks to the whole CBM Collaboration for keeping me busy with challenging and interesting tasks.

I am very thankful to my Gutachters Prof. Dr. Herbert Ströbele and Prof. Dr. Christoph Blume for reading my thesis and providing valuable comments.

I am grateful to Prof. Dr. Marek Gazdzicki for always very didactic lectures and endless discussions about proper way to define and present experimental data. Also, I am thankful to the NA61/SHINE Collaboration for the invaluable experience in data analysis.

Many thanks to my colleagues, especially to my collaborators from MEPhI Eugeny Kashirin and Oleg Golosov for a friendly atmosphere in our group and a productive work. I am also very thankful to Prof. Dr. Arkadij Taranenko for his hospitality during my visits to Russia and many interesting discussions, not only physics related.

I am grateful to my former supervisor from Kyiv Dr. Oleg Bezshyyko and Prof.

Dr. Ivan Kisel for bringing me to this field and to GSI with the GSI Summer Student Program. And I would like to express special thanks to Dr. Maksym Zyzak for helping me during the whole my time in CBM starting from bachelor thesis and to this moment.

I thank the management of HGS-HIRe for organizing all the events, especially two Power Weeks about Efficient Programming, which changed my approach to frameworks development. Also I am grateful to Lukas Kreis for providing a good example in a code development.

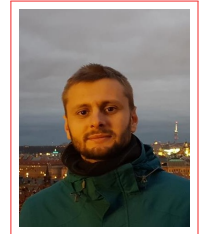
I also very thankful to my friends Valentina Akishina and Hamda Cherif for creating a fun atmosphere in our office.

In the end, I would like to thank all my friends and family for being always there for me.



# Viktor Klochkov

Am Alten Grenzgraben 4  
Darmstadt  
Germany  
☎ +4915257471841  
✉ klochkov44@gmail.com



## Education

- 2016–now **PhD student**, *Johann Wolfgang Goethe University*, Frankfurt am Main, Germany.
- 2013–2015 **Master**, *Taras Shevchenko National University*, Kyiv, Ukraine, *Grade: Excellent*.  
High Energy Physics
- 2009–2013 **Bachelor**, *Taras Shevchenko National University*, Kyiv, Ukraine, *Grade: Excellent*.  
Physics
- 2006–2009 **Pupil**, *Physics and Mathematics Lyceum*, Kherson, Ukraine.
- 1998–2006 **Pupil**, *Secondary school 15*, Kherson, Ukraine.

## Experience

- 2015 – now **Scientist**, *GSI Helmholtzzentrum für Schwerionenforschung*, Darmstadt, Germany, Performance for anisotropic flow measurements, developing Frameworks for data analysis.
- 2015 **Intern**, *L.A.L., Paris-Sud University*, Orsay, France, Data analysis and simulations of the first SoLid module.
- 2013 **Summer Student**, *GSI Helmholtzzentrum für Schwerionenforschung*, Darmstadt, Germany, Reconstruction of the decays of strange particles in CBM experiment using OpenCL.
- 2012 **Intern**, *Joint Institute for Nuclear Research*, Dubna, Russia, Measurement and theoretical description of magnetic field in a Lambertson magnet.

## Schools and conferences

- October 2018 ICPPA, Moscow, Overview of the Compressed Baryonic Matter experiment at FAIR (parallel talk)
- May 2018 Quark Matter, Venice, NA61/SHINE measurements of anisotropic flow relative to the spectator plane in Pb-Pb collisions over a wide rapidity range (parallel talk), Performance for anisotropic flow measurements of the future CBM experiment at FAIR (poster)
- March 2018 DPG Spring Meeting, Bochum, Performance for anisotropic flow measurements of the future CBM experiment at FAIR (parallel talk)
- October 2017 ICPPA, Moscow, CBM performance for anisotropic flow measurements (parallel talk)

- May 2017 International School "Relativistic Heavy Ion Collisions, Cosmology and Dark Matter, Cancer Therapy", Oslo
- March 2017 DPG Spring Meeting, Munster, Performance of charged pions, kaons, protons and their antiparticles identification in the CBM experiment (parallel talk)
- October 2016 ICPPA, Moscow, Centrality determination in heavy-ion collisions with the CBM experiment (parallel talk)
- June 2016 CPOD, Wroclaw, Centrality determination in heavy-ion collisions with CBM (poster)
- March 2016 DPG Spring Meeting, Darmstadt, Performance of centrality determination in heavy-ion collisions with CBM experiment (parallel talk)
- October 2014 CERN Special Ukrainian Students Program
- September 2014 CERN Danube School on Instrumentation in Elementary Particle and Nuclear Physics, Novi Sad
- July 2012 Trans-European School of High Energy Physics, Belgrad
- June 2012 International conference SIN Nano, Dubna-Moscow

## — Awards

- 2017 Giersch-Excellence-Grant 2017 for the outstanding work and progress in the PhD thesis project within the past year.

## — Computer skills

Operating systems	Linux, Windows	Programming skills	C/C++, Python, git, GitLab, CUDA, OpenCL
Physics tools	ROOT, GEANT4	Mathematics tools	MatLab, Mathematica

## — Languages

Ukrainian	<b>Native</b>
Russian	<b>Native</b>
English	<b>Fluent</b>
German	<b>Intermediate</b>

## — Teaching experience

- 2014-2015 **Laboratory**, *Taras Shevchenko National University*, Interaction of ionizing radiation with matter.
- 2014-2015 **Seminars**, *Taras Shevchenko National University*, C++ programming and mathematical modeling.
- 2014-2015 **Laboratory**, *Taras Shevchenko National University*, Methods of detection of the ionizing matter.

## Publications

V. Klochkov and I. Selyuzhenkov. NA61/SHINE measurements of anisotropic flow relative to the spectator plane in Pb+Pb collisions at 30A GeV/c. In *27th International Conference on Ultrarelativistic Nucleus-Nucleus Collisions (Quark Matter 2018) Venice, Italy, May 14-19, 2018*, number Nucl.Phys., 2018.

V. Klochkov and I. Selyuzhenkov. Centrality Determination in Heavy-ion Collisions with CBM. *Acta Phys. Polon. Supp.*, 10:919, 2017.

V. Klochkov and I. Selyuzhenkov. CBM Performance for Anisotropic Flow Measurements. *KnE Energ. Phys.*, 3:416–421, 2018.

Klochkov and I. Selyuzhenkov. Centrality determination in heavy-ion collisions with the CBM experiment. *J. Phys. Conf. Ser.*, 798(1):012059, 2017.

E. Zherebtsova, V. Klochkov, I. Selyuzhenkov, A. Taranenko, and E. Kashirin. Procedure for Event Characterization in Pb-Pb Collisions at 40 A GeV in the NA49 Experiment at the CERN SPS. *KnE Energ. Phys.*, 3:275–279, 2018.

D. Blau, I. Selyuzhenkov, and V. Klochkov. Performance Studies for Strange Hadron Flow Measurements in CBM at FAIR. *KnE Energ. Phys.*, 3:195–201, 2018.

E. Zherebtsova, V. Klochkov, I. Selyuzhenkov, A. Taranenko, and E. Kashirin. Procedure for event characterization in Pb-Pb collisions at 40A GeV in the NA49 experiment at the CERN SPS. *EPJ Web Conf.*, 182:02132, 2018.

Oleg Golosov, Evgeny Kashirin, Viktor Klochkov, and Ilya Selyuzhenkov. Effects of the detector non-uniformity in pion directed flow measurement relative to the spectator plane by the NA49 experiment at the CERN SPS. In *24th International Baldin Seminar on High Energy Physics Problems: Relativistic Nuclear Physics and Quantum Chromodynamics (ISHEPP 2018) Dubna, Russia, September 17-22, 2018*, 2018.

Evgeny Kashirin, Oleg Golosov, Viktor Klochkov, and Ilya Selyuzhenkov. New measurement of pion directed flow relative to the spectator plane by the NA49 experiment at CERN. In *13th Workshop on Particle Correlations and Femtoscopy (WPCF 2018) Kraków, Poland, May 22-26, 2018*, 2018.

N. Abgrall et al. Measurements of  $\pi^\pm$ ,  $K^\pm$  and proton yields from the surface of the T2K replica target for incoming 31 GeV/c protons with the NA61/SHINE spectrometer at the CERN SPS. 2018.

A. Aduszkiewicz et al. Measurements of total production cross sections for  $\pi^+ + C$ ,  $\pi^+ + Al$ ,  $K^+ + C$ , and  $K^+ + Al$  at 60 GeV/c and  $\pi^+ + C$  and  $\pi^+ + Al$  at 31 GeV/c. *Phys. Rev.*, D98(5):052001, 2018.

A. Aduszkiewicz et al. Measurement of meson resonance production in  $\pi^- + C$  interactions at SPS energies. *Eur. Phys. J.*, C77(9):626, 2017.

A. Aduszkiewicz et al. Measurements of  $\pi^\pm$ ,  $K^\pm$ , p and  $\bar{p}$  spectra in proton-proton interactions at 20, 31, 40, 80 and 158  $GeV/c$  with the NA61/SHINE spectrometer at the CERN SPS. *Eur. Phys. J.*, C77(10):671, 2017.

T. Ablyazimov et al. Challenges in QCD matter physics –The scientific programme of the Compressed Baryonic Matter experiment at FAIR. *Eur. Phys. J.*, A53(3):60, 2017.